Politecnico di Milano

Aerospace Science and Technology Department

Doctoral programme in Aerospace Engineering

Self-healing ionomer based systems for aerospace applications

Doctoral Dissertation of:

Antonio Mattia Grande

Supervisor:

Prof. Luca Di Landro

Tutor:

Prof. Michelle Lavagna

Coordinator:

Prof. Luigi Vigevano

2011-2013 - Cycle XXVI

...

Abstract

In recent years one of the most attractive topics in material science is the study of self-healing materials. Many researchers are working on this matter and different approaches have been developed to obtain new polymeric materials with self-healing ability. Thermoplastic polymers as ethylene-co-methacrylic acid based ionomers have shown a self-healing behaviour after high-energy impacts, however the exact relationship between the polymer physical properties and the repairing efficiency is still unclear.

In this research the self-healing feature exhibited by this particular class of polymers has been extensively studied and critical parameters for an efficient damage repair were identified. Moreover, series of physical experiments aimed to the understanding of the correlation between polymer structure/properties and self-healing behaviour were carried out.

In view of an extension of the property ranges required in different potential applications, new polymeric systems have been prepared and tested under different impact conditions. In particular multilayer systems incorporating one or more self-healing layers and polymeric blends, both based on an ethylene-co-methacrylic acid ionomer, were designed.

Finally, the obtained results suggest that there is real potential for using these self-healing thermoplastic polymers in complex structures to heal high velocity impact damage.

Contents

Figure index

Table index

Chapter 1 - Introduction to self-healing materials

1.1 Introduction

Intentionally created self-healing behaviour has become an active research topic in materials science in recent years. A very early example of engineered, intentional self-healing behaviour is the work of Dry [1,2] who included hollow glass fibres filled with a liquid adhesive in a concrete matrix prior to setting of the concrete. Upon local fracture of the matrix the glass fibres break, the liquid adhesive flows out and fills the crack, wets the crack surfaces and crosslinks. After crosslinking the load bearing capacity of the concrete is restored to some degree. The concept works and led to some restoration of properties, but the improvement was modest as the efficiency of the healing process was moderate due to various reasons: the mortar was not fully dense (leading to loss of healing agent into non-relevant pores), the fracture surfaces were rough, the crack opening was uncontrolled and sometimes too large, and there is a big difference in chemical nature between the polymeric healing agent and the inorganic concrete matrix.

A more successful and much more widely acclaimed attempt was made by White et al. [3]. In their research they mixed polymeric microcapsules filled with a crosslinkable liquid oligomer into a low viscosity epoxy matrix with dispersed Grubbs catalyst. Upon controlled fracture of the material, the crack intersects the capsules and breaks them leading to the flow of the healing agent into the crack. The healing agent wets both crack surfaces comes into contact with the dispersed catalyst particles and undergoes a crosslinking reaction leading to a significant restoration of the tensile strength of the sample. In their system a much higher healing efficiency was obtained probably due to the epoxy failing with a smooth planar surface, the fact that the crack opening distance

was artificially kept low and the chemical compatibility between the healing agent and the epoxy matrix.

Very early on, it has been realised that the crack filling potential of small spherical microcapsules is intrinsically limited, and a much better 'long distance supply' of healing agent could be obtained by storing the healing agent in long hollow fibres. Bond et al. [4,5] showed for the first time the effective self-healing behaviour in fibre reinforced composites using hollow fibres. The working principle of these self-healing composites is essentially the same as that for the microcapsule filled unreinforced epoxy material.

Since these three landmark contributions showing engineered self-healing behaviour in man-made materials many new healing concepts for virtually all classes of materials have been developed [6-9]. In this development process two conceptually different routes emerge: i) the extrinsic healing route in which the (generally liquid) healing agent is incorporated into the matrix as discrete entities not contributing to the main functionality of the base material; ii) the intrinsic healing route in which the healing capability is intrinsically connected to the (chemically or compositionally tuned) matrix material. Unlike the case of extrinsic systems where the healing at a particular location can only happen once as the healing agent irreversibly loses its fluidity upon reacting, in intrinsic healing systems healing at a particular location can take place several times as no healing agents are consumed in the healing action. As the healing in intrinsic self-healing materials relies on molecular diffusion processes, only cracks more or less in contact can be healed. For intrinsic healing polymers to heal they should either be already above their glass transition temperature or a temporarily stimulus (such as temperature or moisture) to increase the molecular mobility should be applied.

1.2 Extrinsic self-healing systems

1.2.1 Microcapsules based systems

After the original research of White et al. [3] presenting a microcapsule based self-healing polymer, several scientists have been working on this concept in order improve the efficiency of such system [10-16]: given the proper capsules dimensions and capsule volumetric density, cracks with a crack opening distance of typically up to 500 μm can be healed.

The most commonly adopted polymers in capsule based healing systems are stiff thermosets, e.g. epoxy and vinyl ester, however capsule based self-healing elastomers were also developed and tested [17-19]. In addition, early research by Sanada et al. [20] showed how this extrinsic self-

healing concept can be employed to heal the interface between fibre and matrix. In their work, carbon fibres were coated with an epoxy based mixture containing 10 to 40 wt% urea-formaldehyde (UF) nano-capsules filled with dicyclopentadiene (DCPD) and 2.5 wt% Grubbs' catalyst dispersed in the polymeric matrix. Tensile composite specimens containing such surface modified fibres were manufactured and tested, showing a recovery of up to 19% of the original interface strength. The fact that healing took place demonstrated the validity of the approach, yet the modest level of healing also revealed the inherent limitation of small capsule sizes to heal damage of more substantial dimensions. The effects of different parameters such as capsule dimension and distribution around fibre were reported elsewhere [21].

A similar self-healing system was studied by Blaiszik at al. [22] using a micro-debonding test. In this research glass fibres, coated with Grubbs' catalyst and microcapsules containing a liquid healing agent (DCPD), were embedded in a commercial epoxy matrix to produce single fibre pull-out samples. A maximum average healing efficiency of 44% was measured for 1.2 wt% Grubbs' catalyst concentration and a high interfacial capsule concentration level.

Extrinsic self-healing approach based on microcapsule was also explored by Jones et al. [23] using a single capsule solvent-based healing chemistry. Prepared UF microcapsules containing EPON 862 (diglycidyl ether of bisphenol-F) dissolved in ethyl phenylacetate (EPA) solvent were dispersed on glass fibres using a dip-coat technique (Figure 1.1). Probably due to the larger capsule size and the application of an external force to close the crack, nearly full recovery of interfacial strength (86% maximum healing efficiency) was reached.

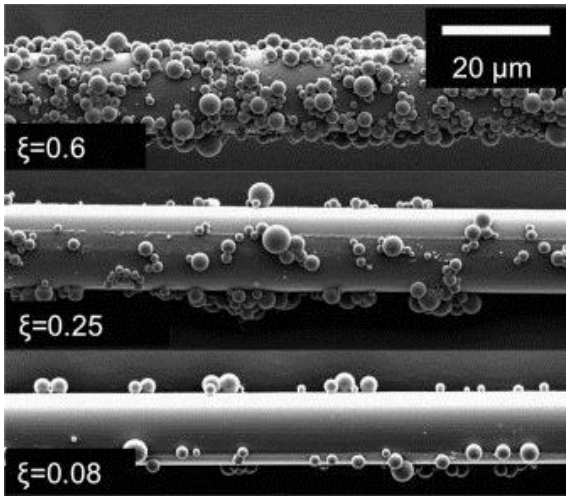

Figure 1.1: SEM micrographs of capsule coated glass fibres [23].

1.2.2 Hollow fibres and microvascular based systems

The development of hollow fibres self-healing systems involves the embedding of such containers for the liquid healing agent in polymeric matrix. Bond et al. [4,5,24,25] have made optimal use of this last concept, but their work also shows that the insertion of filled hollow glass fibres lowers the undamaged properties of the composites substantially as is to be expected given the large difference in specific properties of the fine yet solid carbon fibres and the relatively coarse liquid filled glass capillaries (Figure 1.2).

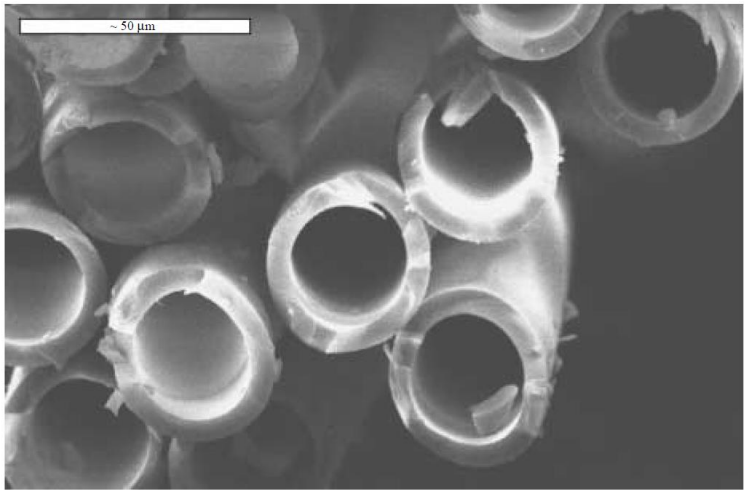

Figure 1.2: SEM micrograph of hollow glass fibre to be used in a Carbon fibre epoxy composite [25].

Furthermore, the controlled positioning of the hollow fibres at the most damage sensitive locations of the composite is by no means trivial and will increase the manufacturing costs considerably. From a manufacturing point of view the 1D systems involving filled hollow fibres seem to be the easiest to be incorporated in currently available manufacturing processes. Recent work by Norris et al. [26-29] showed the importance of alignment of the channels with the local fibre orientation in the ply without disrupting the fibre architecture of adjacent plies too much. To be successful, the distance between neighbouring channels needs to be optimized to prevent significant changes in the mechanical properties of the fibre reinforced composite material before and after introduction of the 1D vasculature. It was shown that the failure strength of $[-45/90/45/0/90]_{2s}$ carbon epoxy composites was hardly affected by the presence of 0.5 mm diameter open channels placed 10 mm apart [26]. Notwithstanding the relatively straightforward 1D healing approach almost full recovery of the mechanical properties of the impacted samples was observed in compression testing after impact.

However, the intrinsically limited healing potential of 1D filled hollow glass fibres has led to more complex 2D and 3D network systems, [30,31] although manufacturing of such networks is hardly compatible with current large-scale production methods of fibre reinforced composite materials. An interesting new approach has recently been presented by Esser-Kahn et al. [32] employing sacrificial polylactic fibres that are woven into 3D glass pre-forms employing a common mechanical weaving technique. After curing of a thermosetting resin, the polylactic fibres are thermally decomposed to obtain a 3D microvasculature allowing infiltration with a suitable healing liquid. As with all extrinsic healing systems the healing capability is restricted to one healing action per location only.

1.2.3 Alternative fibre-based healing systems

A slightly different approach in a new healing system is envisaged in the multi-encapsulate fibres produced by Mookhoek et al. [33]. Instead of making long continuous capillaries they focus on the production of alginate fibres containing multiple healing agent filled discrete vacuoles all along the fibre (Figure 1.3). These fibres can be tuned to have the same mechanical properties as the epoxy. Furthermore they can be spun in diameters comparable to those of the regular reinforcing glass or carbon fibres. Insertion of such new fibres will allow multiple local release and healing events. As with the hollow continuous glass fibres, the alginate fibres will lower the specific mechanical properties of the composite, but they may be blended more easily with the reinforcing carbon fibres and their properties can be tuned to match those of the matrix.

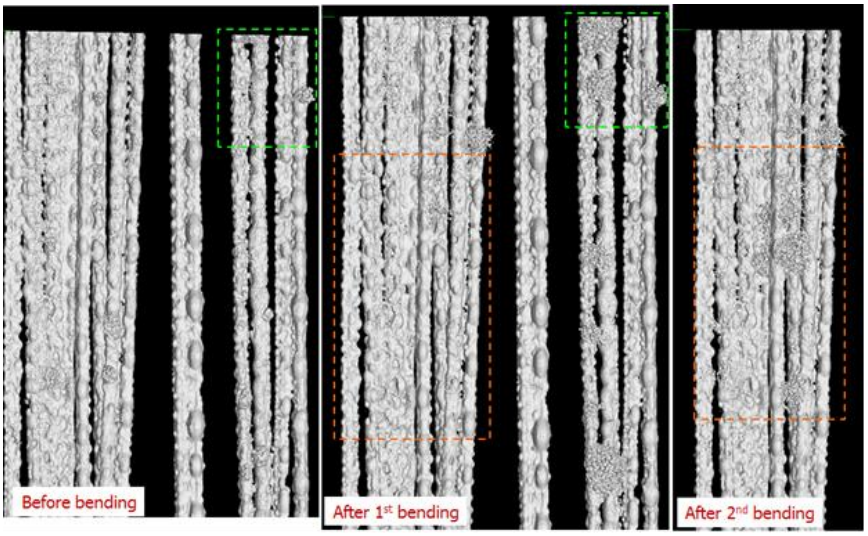

Figure 1.3: Tomographic image of a set of PMMA embedded multi-vacuole fibres in the unloaded as-produced state, after a first sample bending and after a second bending.

An alternative, rather new and promising approach is the use of electrospun or solution-blown core-shell nanofibres [34-37]. Prepared as nanofibrous mats they may be easily integrated during laminate layup as thin interleaves with submicron out-of-plane dimensions hardly affecting the overall weight, strength and stiffness of its host. Yet, their presence at the interface between successive plies promises optimal dispersion of healing fluids at the relatively brittle resin-rich interface layer leading not only to the capability of micron sized damage but also potentially leading to an increase in the interface toughness at a systems level.

1.3 Intrinsic self-healing systems

In intrinsic healing concepts the healing process depends on the ability of the polymer matrix to locally acquire temporary mobility upon the application of an external or internal trigger such as temperature, pH or light induction and generally intrinsic healing systems are not truly autonomous [38-40]. However, they have the advantage that no external healing entities are required and multiple healing events can be obtained, albeit at the expense of their mechanical properties. The general concept of intrinsic healing is depicted in Figure 1.4 where the sudden drop in viscosity upon heating is linked to local temporary network mobility necessary for flow and damage repair. Upon cooling the local properties (e.g. viscosity) are restored to initial values so the material can be further used. Moreover multiple healing events are possible with intrinsic healing approaches.

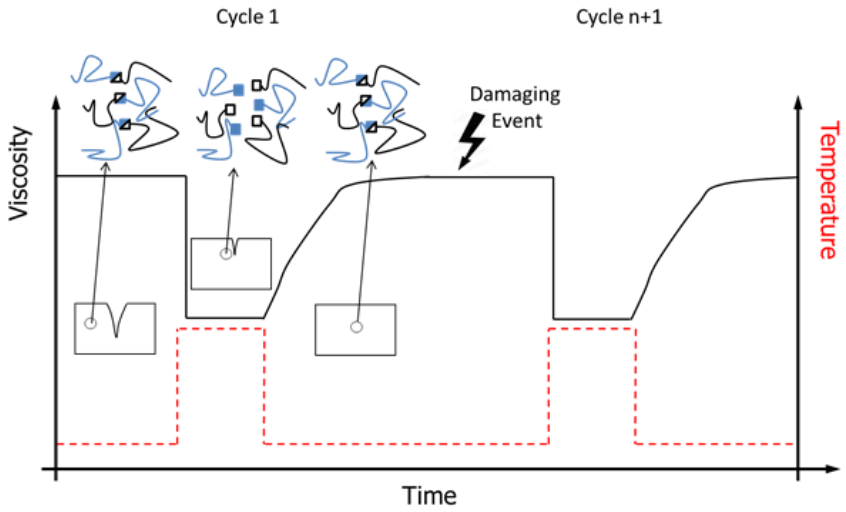

Figure 1.4: General concept of matrix healing using intrinsic healing concepts.

Three distinct polymer concepts can be employed: i) reversible covalent bonds [41]; ii) supramolecular interactions [42]; and iii) shape memory polymers [43]. Additionally, blends of conventional matrix polymers and polymers with intrinsic healing potential have been proposed to create healing capabilities while improving the mechanical properties of matrix [44]. These four approaches/concepts will now be discussed in more detail.

1.3.1 Reversible covalent bonds

Probably, the most known and widely used reversible covalent bonds in intrinsic healing are those based on Diels-Alder/retro-Diels-Alder interactions (DA/rDA). This reversible bond was first reported by Craven et al. in 1969 [45], but it was not until the beginning of the 21st century that it was used for reversible polymer matrices [46]. In this chemical reaction several di-enes and di-enophiles can be used with the furan-maleimide interaction (healing temperature range of 100-150 °C) being the one known best [47,48] (Figure 1.5). Polymers based on the DA-rDA reaction have already been employed in fibre-reinforced composites [49-52], as well as in self-healing hybrid nano-composites [53].

Disulphide bonds being part of a conventional epoxy based thermoset represent an interesting reversible covalent chemistry that has nevertheless not yet been implemented into Fibre Reinforced Polymers (FRPs) [54,55]. Research on functional composites for thermal conduction purposes based on such polymer matrices has shown promising results even for mild healing temperatures (65-75 °C) [56,57].

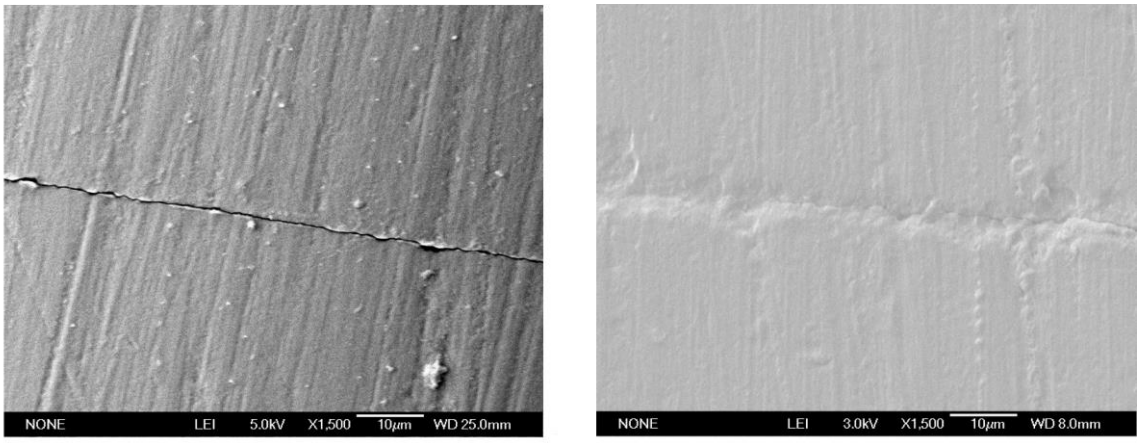

Figure 1.5: Self-healing capabilities after a thermal cycle of a rDA based polymer [48].

Provided the interfacial crack faces are in some form of local contact, healing of matrix/fibre interface can also be achieved with intrinsic self-healing methodologies. Peterson et al. [58] exploiting Diels–Alder reaction, demonstrated how maleimide-functionalized glass fibres and furan-functionalized polymer networks create a thermo-reversible matrix/reinforcement interface (Figure 1.6). Micro-droplet single fibre pull-out tests revealed an overall average of 41% recovery of interfacial strength upon healing for. The researchers reported multiple healing events up to five times where the healing efficiency dropped to about 10%. The drop in healing efficiency is not related to the loss of healing as such but reflects the detrimental effects of multiple successive local fracture events upon the crack opening distance and the decrease in topological registry across the separated interfaces.

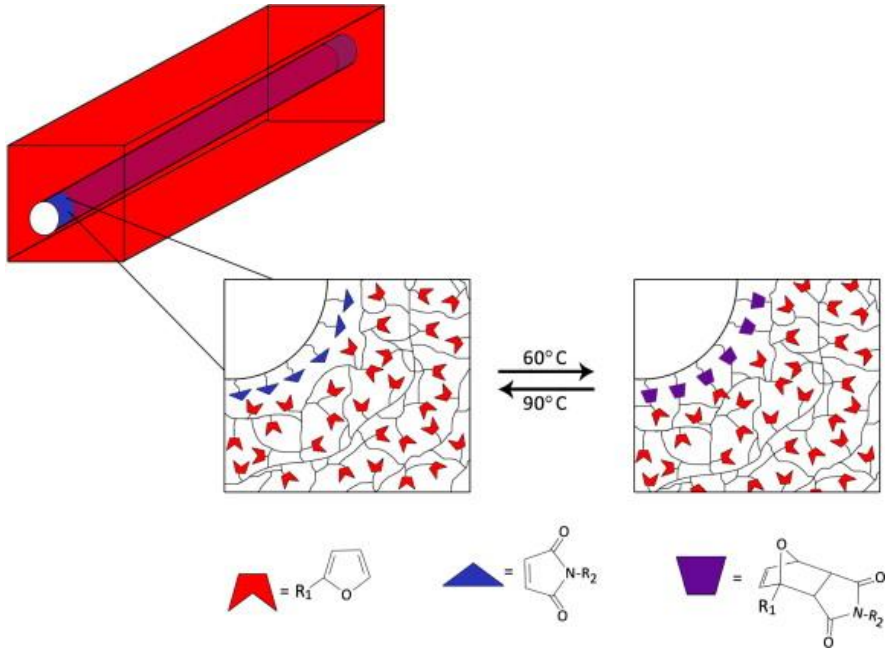

Figure 1.6: Intrinsic interfacial healing concept based on Diels–Alder reaction, failed bonds between furans and maleimides are restored after a thermal cycle [58].

1.3.2 Supramolecular interactions

Supramolecular interactions are by definition reversible and are ideal mechanisms to create self-healing polymer matrices [42]. Currently, hydrogen bonding is one of the most established supramolecular self-healing mechanism. A very successful approach was introduced by Sijbesma et al. [59]. In their work, a strong reversible polymer system based on quadruple hydrogen bonding was developed and the concept proven. The work was successfully further developed by Leibler et al., in collaboration with Arkema [60,61], leading to the very first commercially available

intrinsic self-healing elastomer. Recently new chemistries have been presented using supramolecular reversible bonds as encountered in perfluoropolyethers [62], polyethyleneimine additives in nitrile rubbers [63] and via polydimethylsiloxane chains in traditional self-healing rubbers [64].

New intrinsic healing polymer systems based on π-π interactions were reported by Burattini et al. and there are interesting developments in the field of cellulose based nanocrystal reinforced self-healing nanocomposites [65-67]. Furthermore, a metal ligand system, which heals upon exposure to higher light fluxes, was recently reported by Burnworth et al. [68].

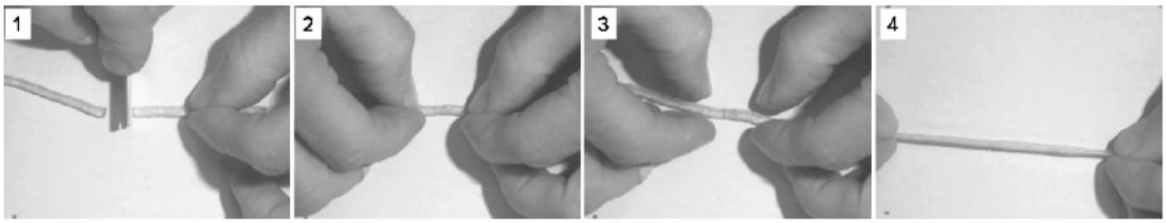

Figure 1.7: Self-healing supramolecular rubber: a) cutting, b) mending, c) healing, d) stretching [61].

Finally, another type of non-covalent reversible interactions is found in ionomers. These are polymer systems containing acid groups in the form of ionic metal salts bonded to the polymer backbone creating electrostatic interactions. As a result, ionic clusters are formed within the polymer structure, which have a positive effect on the mechanical and physical properties of the material [69]. Most of the work done on self-healing ionomers has focused on autonomous healing after high-speed ballistic impact [70-74], but stimulated self-healing after more quasi static damage production has also been demonstrated [75]. An extensive discussion of the self-repairing ability shown by these materials is addressed in the following paragraphs.

1.3.3 Shape memory polymers

A third category of matrix healing processes involves Shape Memory Polymers (SMPs). These polymers have the ability to plastically deform yet to return to their original shape upon exposure to external stimuli, a phenomenon called the Shape Memory Effect (SME). In order to induce the SME, the SMP system requires both a stable polymer network and the possibility of a Reversible Switching Transition (RST). The stable polymer network determines the original shape, whereas the RST, commonly based on crystallization or vitrification, is responsible for the shape recovery [43,76].

Although SMPs show some potential as self-healing matrices, they have relatively low strength limiting their use in structural applications. As a possible solution, fibre reinforced SMP composites are developed improving the mechanical properties of SMPs [77,78]. However, the additional rigidity that is supplied by the fibres lowers the SME and thereby the healing properties of the polymer matrix. Additionally, these polymer systems often need a pre-training step that determines the fixed shape, which will be difficult to realise in technical composites [79].

As mentioned above, SMPs can be used for healing purposes although they have the intrinsic limitation that they only close the crack, yet do not restore mechanical strength across the final interface [80]. As an alternative, Li et al. [81] proposed a close-then-heal (CTH) scheme using a SMP matrix filled with thermoplastic particles. Under this concept, the material will first close the crack due to the SME and then seal due to the embedded thermoplastic particles upon heating. Nji et al. reported a couple of studies on the validation and experimental testing of this concept [82,83]. The shape memory assisted self-healing (SMASH) technique, introduced by Rodriguez et al., shows a similar approach by blending a SMP matrix with self-healing linear polymer chains [84,85].

Shape Memory Alloy (SMA) can also be utilised to reduce the crack opening distance; Bor et al. [86] and Neuser et al. [87] demonstrated that the substantial contraction of metallic SMA wires, upon a thermal input, will be beneficial for host healing system efficiency.

1.3.4 Polymer blends

Despite the interesting potential of the polymers based on reversible chemistries, their applications may be restricted as a result of their intrinsically low mechanical properties. In order to find a better balance between base mechanical properties and some healing capability, polymer blends have been proposed. Zako et al. [88] reported on the inclusion of melt processable thermosetting epoxy particles in a stable and rigid polymer matrix. In case of fracture, the additives melt when heated to about 100 °C and react at the damaged site, thereby healing the material. Hayes et al. [89,90] developed a single phase blend by dissolving a thermoplastic linear molecules, rather than thermoplastic particles in a conventional thermoset matrix. In this case long-range polymer diffusion across the interfaces of the crack may occur while the surrounding thermoset matrix remains unchanged. Both approaches require an external application of heat to induce healing. In an attempt to solve this issue, Swait et al. [91] have recently proposed the use of self-sensing carbon fibre reinforced matrix systems capable of detecting barely visible impact damage by measuring changes in resistance. A combination of this

matrix with a self-healing single phase blend and a self-heating mechanism could eventually result in a truly smart composite material. Other single phase self-healing epoxy matrices based on mechanical interlocking and interpenetrating networks have been demonstrated successfully yet at the proof of concept level and for unreinforced bulk polymer samples [92,93]. A fibre reinforced composite system containing a reactive thermoplastic additive (ethylene-co-methacrylic acid copolymer) that heals upon heating was developed by Meure et al. [94-97] and Varley et al. [98]. A recent study investigated the healing of these composites upon application of ultrasound [99]. The use of polymerization-induced phase separation to produce a poly(e-caprolactone)/epoxy blend that is capable of matrix healing by differential expansive bleeding has been proposed by Luo et al. [100]. The mechanical properties of these matrices were enhanced using carbon nanofibres without loss of the self-healing properties [101].

Supramolecular self-healing systems are also incorporated in blends in order to enhance their mechanical properties. For example, the blending of hydrogen-bonding brush polymers with a thermoplastic elastomer resulted in a polymer matrix that can heal without the requirement of external stimuli [102].

1.4 Damage management concept

In traditional materials, local damages occur for different causes (e.g. mechanical/thermal over-loads, fatigue loads, impacts) and they can propagate until the catastrophic failure of the entire structure. In this view, damage prevention and, nowadays, damage tolerance design philosophies have been developed in order to estimate damage propagation and then structure lifetime [103,104]. In the damage prevention approach, structures are designed in order to postpone as much as possible the formation and then the propagation of critical damages achieving the maximum possible safety margin and a reasonable lifetime of the structure [105]. On the other hand, the damage tolerance strategy admits damage propagation and particular attention is used for damage limit and damage growing in order to implement the right inspection and maintenance program [106] and also involving the capability of prediction of how the damage could evolve even with sophisticated numerical models [107-110].

The development of new materials with self-healing capabilities introduces the damage management concept in structural design [7]. This new class of materials has a built-in capability to repair damages, that may occur during structure operation, so as to partially or completely restoring initial proprieties. This particular feature leads to an understandable increase in interest

in self-healing materials [111], also in the aerospace field where the reliability of the structures and at the same time the maintenance costs reduction play a fundamental role.

As presented in Figure 1.8, an ideal self-healing material has an unlimited ability to completely repair damages which may occur achieving, theoretically, an infinite lifetime compared with tradition and improved materials. However this ideal behaviour has not yet been reached and the developed self-healing materials show partial initial property restoring and limited healing events.

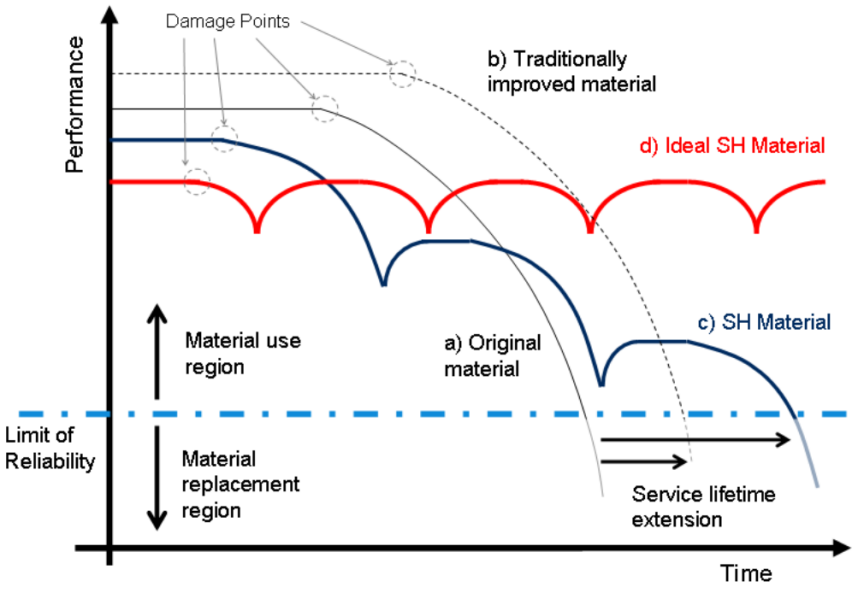

Figure 1.8: Traditional materials vs self-healing materials [112].

1.4.1 Damage modes and reported healing efficiencies

1.4.1.1 Damage due to static (over-) loading

Quasi-static fracture tests are widely used to assess performances of self-healing polymers and composites. The monotonic low strain rate loading condition is generally not so relevant for real life applications, yet this mode of testing is highly controlled both for the generation of damage and a relatively straightforward and (semi-) quantitative evaluation of the restoration of properties upon healing. The most common techniques, usually adopted for matrices and composites, are double-cantilever beam (DCB), its tapered (TDCB) or width-tapered (WTDCB) variants and end-notched flexure (ENF) tests. Other procedures, also used to evaluate global mechanical properties after healing, include tensile, three-point bending and four-point bending experiments.

Kessler et al. [113,114] studied the self-healing behaviour of both glass and carbon FRPs loaded with different DCPD/Grubbs' catalyst microcapsule systems. After mode I fracture experiments, a maximum average interlaminar fracture toughness recovery of 66% was reported for specimens healed at 80 °C for 48 h. Comparable results were obtained by Yin et al. [115] using a micro-encapsulated epoxy/latent curing agent system; after a healing cycle at 130 °C for 1 h and 24 h at room temperature, 51% fracture toughness recovery was measured.

Different systems based on a micro vascular approach (i.e. using one or two interconnected networks of hollow fibres containing one or two healing agents respectively) were developed by Trask et al. [25]; healing efficiency of previously damaged FRPs hosting glass hollow fibres filled with a two-part epoxy healing agent were measured under flexural loads. After heating for 2 h at 100 °C were employed a strength recovery of about 80% for glass and carbon reinforced composites was reported. Following the intrinsic self-healing approach Hayes et al. [89] employed poly(bisphenol-A-co-epichlorohydrin) as solid healing agent in a commercial epoxy resin demonstrating the ability of such system to recover up to the 70% of its fracture strength after thermal healing cycle (140 °C). Other studies, revealed the potential of polyethylene-co-ethacrylic acid (EMAA) as a thermally activated thermoplastic healing agent [98, 116]. Produced carbon FRPs laminates tested under different static experiments are able to completely restore both mode I and mode II fracture toughness after a thermal cycle of 30 min at 150 °C. Melting and infusion of EMAA along the crack plane and strong EMAA-epoxy bonding are responsible for crack bridging detected during after healing fracture test (Figure 1.9).

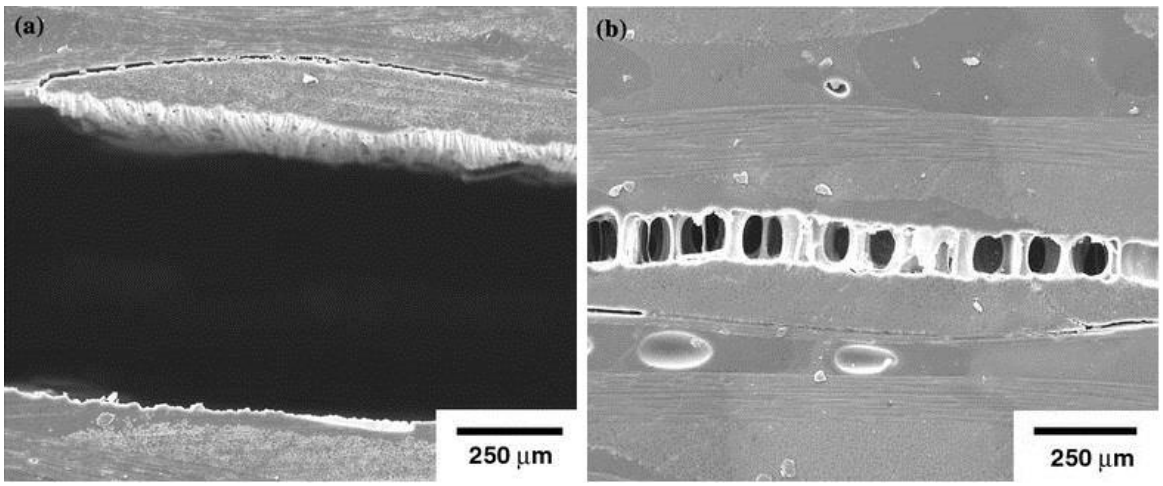

Figure 1.9: Crack path during static mode I fracture test for virgin (a) and healed (b) sample [116].

While the results of experiments aimed to demonstrate healing after quasi static loading are certainly interesting and encouraging, it should be pointed out that the test configurations are such that the crack opening distance is generally kept at a low value by careful reposition of the fracture surfaces or even the application of a minimal crack closing force In real life applications this may not always be the case or be possible.

1.4.1.2 Damage due to fatigue loading

Fatigue damage is of great relevance in polymer mechanics and the development of self-healing systems able to operate during cyclic loading is still a relatively new challenge for researchers working in the self-healing field. Promising studies on the fatigue behaviour of microcapsule loaded epoxy matrix have been presented in the literature. Brown et al. [117] demonstrated how a self-healing system based on a microencapsulated DCPD healing agent and Grubbs' catalyst dispersed into a commercial epoxy resin can arrest and retard fatigue crack growing. As reported by the authors, fatigue life-extension, investigated using a TDCB geometry, stems from the viscous flow of the healing agent in the crack plane and from its subsequent polymerization providing a short-term adhesive effect and a long term crack closure effect. It is important to underline that better results in terms of healing efficiency and life-extension were obtained in fatigue experiments with a rest period of 10 h in order to allow a complete cure of the healing agent (Figure 1.10). Jones et al. [118], using a wax-protected Grubbs' catalyst, extended the fatigue life of such system even further.

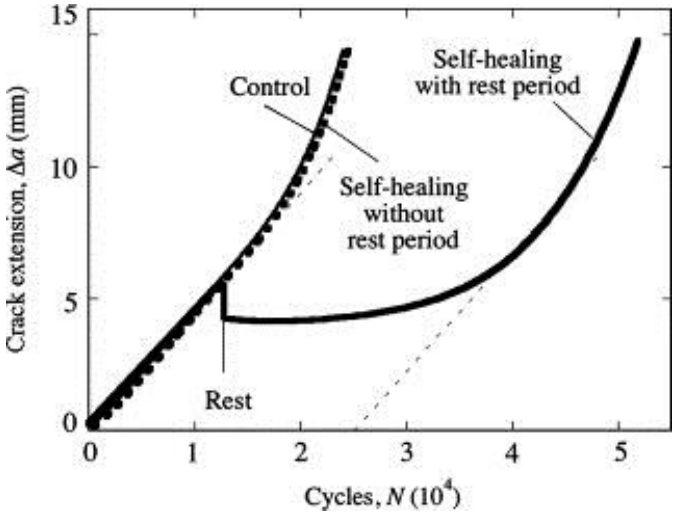

Figure 1.10: Evolution of crack length under fatigue loading with and without rest period [117].

Relevant results were also obtained by Yuan et al. [119]; in their research they developed an epoxy/mercaptan/tertiary amine microencapsulated healing system proving its fatigue crack retardation, arrest and healing capabilities.

Preliminary results on FRPs with intrinsic self-healing capability were presented by Pingkarawat et al. [116]. In their study, a carbon fibre/epoxy laminate containing particles or fibres of an EMAA thermoplastic polymer were tested under fatigue interlaminar loading. Delaminated specimens, upon a thermal cycle at 150 °C for 30 min, partially restored their fatigue resistance demonstrating that the EMAA is an effective agent for the healing of fatigue cracks. However, researchers detected a lower healing efficiency in samples tested under fatigue loading then in those tested under static conditions.

1.4.1.3 Damage due to impact loading

In composite systems, damages generated by impact events range from Barely Visible Impact Damage (BVID) to large-scale breakage like target penetration depending on projectile velocity and energy. Both scenarios are taken in account by researchers working in the self-healing field and different approaches have been developed to heal such kind of damages.

BVID, usually caused by quasi-static point loading or by low velocity impacts, are characterised by intra-ply microcracking and inter-ply delaminations; a common test adopted by researchers to evaluate the various levels of impact damage and the recovery of post impact strength in a FRP laminate with self-healing ability is the Compression After Impact (CAI) protocol.

Microcapsule based self-healing systems were adopted by Yin et al. [120] and Patel et al. [121] to produce woven glass fabric composites using bisphenol-A epoxy healing agent with a latent hardener dispersed in the matrix and DCDP/Grubbs' catalyst approach, respectively. CAI experiments revealed the healing capability of such systems. However the recovery of compression strength becomes marginal for the higher impact loads, probably due to the small quantity of healing agent available given the size of the crack volume created. Micro-vascularised fibre reinforced polymer composite systems, requiring a pressure source to supply the healing agents, can potentially provide enough healing agent to fill cracks generated during high-energy low velocity impacts. Williams et al. [122] and Norris et al. [26] designed FRPs employing different methodologies to create a vascular system in the composite. In the first study, a resin filled hollow glass fibre system was distributed within the laminate, in the second one, open channels were directly generated inside the composite during production by means of PTFE coated steel wire

vascular pre-forms removed after the post-cure cycle. Both studied reported a significant compression strength recovery (>90%) after impact.

High velocity impact damages typically appear in the form of perforation; these damages cannot be healed with the previously presented techniques. However, a particular class of thermoplastic materials, copolymers and ionomers based on EMAA, have shown self-healing behaviour after high velocity impacts over wide range of impact velocities [70-75]. These results clearly suggest that there is real potential for using self-healing thermoplastic matrix in structural composites to heal high velocity impact damage.

1.5 Self-healing behaviour of EMAA based copolymer and ionomers

Thermoplastic ionomer, developed in the early sixties, contain a certain percentage of ions (usually up to 20%) along the polymer chains [123]. They find significant applications in packaging and sport items (for ex. golf balls). Thanks to their self-healing behaviour, they are currently considered also for applications in various fields of advanced engineering. In addition, this class of polymers have attracted researchers for their unusual mechanical properties. Akimoto et al. [124] studied the effect of aging conditions on mechanical behaviour and proposed a model for the morphologic changes during material deformation; Scogna et al. [125,126] verified the applicability of Ree-Eyring model to the yielding of ethylene-co-methacrylic acid ionomers.

Despite more than four decades of widespread commercial use, only in the last decade researchers have disclosed the self-healing capability of EMAA based ionomers after ballistic impacts (Figure 1.11).

The repair of damages is autonomous and instantaneous without any external intervention. The process can virtually be repeated many times and this is a distinctive feature of these materials, especially when compared with other approaches that usually allow only a limited number of repeated repair cycles. Ionomers based on ethylene-co-methacrylic acid copolymer are one of the first class of polymeric materials which have been found to exhibit such self-healing capability and these peculiarities suggest a number of potential applications in environments prone to impact damages since impact itself can activate healing.

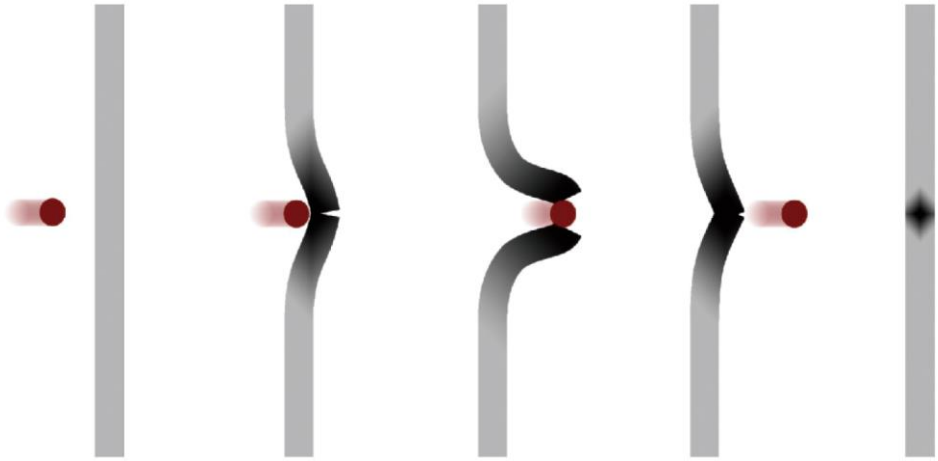

Figure 1.11: Schematic representation of the self-healing process during high-energy impact in EMAA based polymers [7].

In recent years, this self-repairing behaviour after high energy impacts has been studied and described by Kalista et al. [70,71] and Varley et al. [72-74]. These studies were mainly focused on the self-healing behaviour after ballistic impacts and they investigated the effects of test and environment conditions on the hole closure efficiency (Figure 1.12). Further researches followed thereby, to achieve a better understanding of the self-mending mechanism and new test methods were also developed [75].

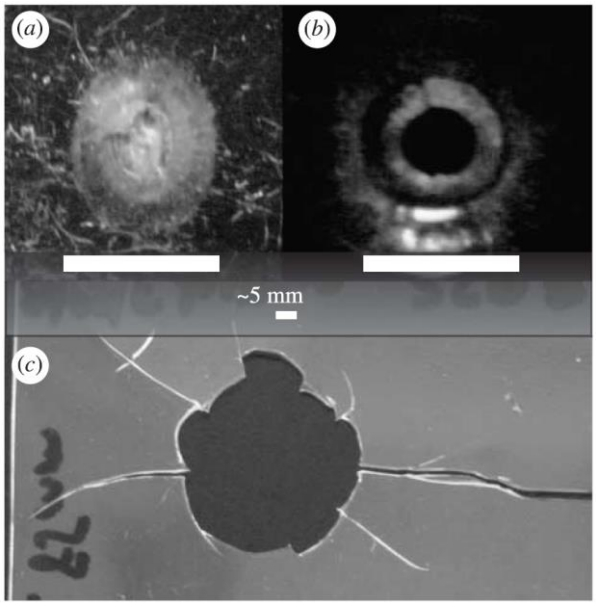

Figure 1.12: EMAA sample following puncture tested at room temperature (a), high temperature (b) and low temperature (c) [70].

The self-healing phenomenon occurs spontaneously after impacts with energy high enough to allow the projectile to pass through the material in a very short time. The amount of energy transferred to the damaged material is thus believed as one of the main aspect influencing the healing capability, since it was well evidenced that the autonomic mending takes place only under defined conditions of temperature, speed and shape of the impacting object; nonetheless, the exact relationship between the mechanical properties and the healing efficiency is still unclear.

A two stage healing mechanism for ionomers was proposed: in a first stage, elastic/viscoelastic recovery is supposed to bring to hole or damage closure, while in a second stage, some local melting/solidification process leads to full or partial welding [70-71]. This healing mechanism was further supported by Varley et al. [73] where they showed that ultimate healing level depends on the elastic response during the impact and post-viscous flow of the material.

Recent results obtained by Kalista et al. [127] showed a different response after ballistic impact of EMAA based ionomer depending on neutralization level and environmental temperature (Figure 1.13). In particular the ionomer with the 30% of acid groups neutralised with sodium ions exhibited the largest temperature range in which the self-healing behaviour appears. However, all tests were performed maintaining constant projectile dimension/shape (4.5 mm pointed bullet) and speed (about 180 m/s).

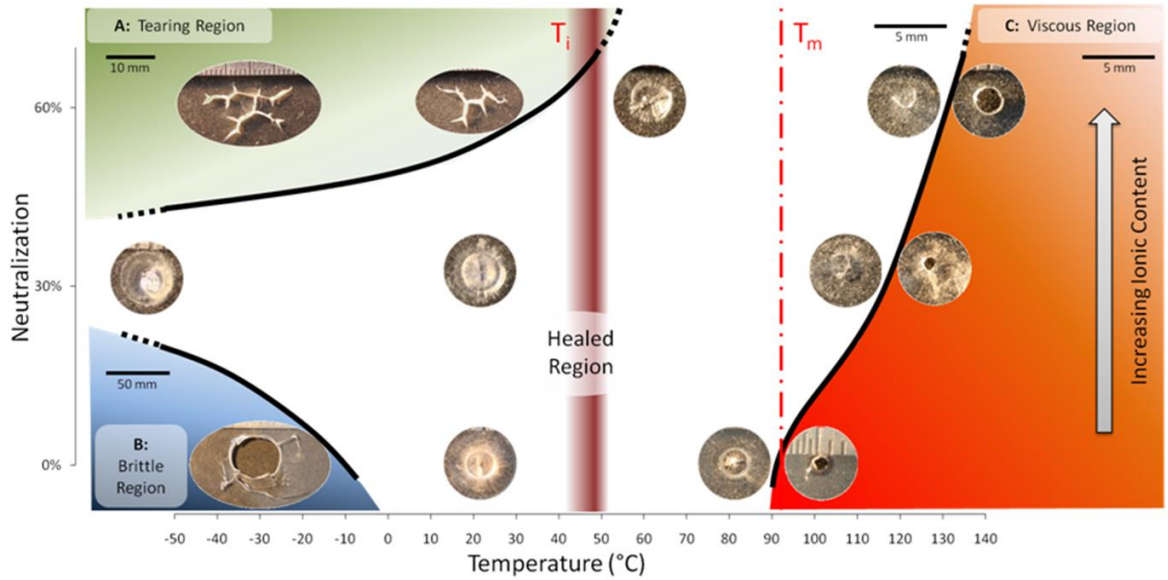

Figure 1.13: Proposed self-healing "phase diagram" after ballistic impact for EMAA based copolymer and Na ionomer as a function of temperature and ionic content [127].

As is apparent from the presented results, these materials are suitable for many potential applications and it is therefore understandable the remarkable interest in the study of their characteristic repair process in order to develop new materials with similar ability over an extended range of conditions.

1.6 Outline

The rapid developments in various healing strategies over the last two decades have created the notion that incorporation of self-healing capability in polymeric systems will seriously contribute to the reliability of these materials for both non-structural and structural applications by making them more damage resistant. Despite encouraging lab scale results using well controlled samples and modest damage levels, large steps still have to be taken to bring this new technology to the right "Technology Readiness Level" where self-healable polymer based products can be manufactured in an economically justifiable way on a routine basis. Additional and improved experimental activities under several testing conditions are required to prove and evaluate the self-healing behaviour of new polymeric systems in order to adopt such materials in real applications.

In this research, a particular class of polymers, EMAA based copolymers and ionomers, which exhibits a self-healing behaviour after high-energy impact, was deeply studied investigating the response of these materials under different experimental conditions and relating such characteristic feature with polymer microstructure, thermo-rheological and mechanical behaviour (Chapter 2-3). On the basis of obtained results new EMAA based systems were developed and presented in Chapter 4 and Chapter 5. Finally, Chapter 6 provides an overview on the potential applications in the aerospace field of the new self-healing polymeric systems, along with new perspectives on future work.

Chapter 2 - Rate dependent self-healing behaviour of an EMAA based ionomer

2.1 Introduction

In this chapter, both mechanical and self-healing properties of ethylene-co-methacrylic acid ionomers with 30% of acid groups neutralized with sodium ions (EMAA-30Na) were evaluated through high-energy bullet impacts and tensile tests, studying the response of the material under different experimental conditions. The autonomic repair response of the ionomer has been studied by ballistic puncture tests under different conditions, which were assessed by varying sample thickness and projectile diameter; the same bullet shape was maintained: metallic spheres were launched in all performed tests. In view of possible applications such as in multilayer structures of space vehicles/stations or in anti-leakage protections for vehicle/aircraft fuel tanks, impact experiments were performed at low velocity, mid velocity and hypervelocity, thus extending the speed range investigated in previous studies [70-74].

After all experiments, the healing efficiency was evaluated by applying a pressure gradient. Hole closure was tested both by following vacuum decay and by checking for possible flow of a fluid droplet placed at the damage zone with the applied pressure difference. A morphology analysis of the impact zones was also made observing all samples by scanning electron microscope (SEM) both in the bullet entrance and exit sides. The results showed a different behaviour of the material subjected to impacts at different rates. At low bullet speed, a full melting process does not seems to take place; however, SEM analysis revealed small melted zones in the impact site. Furthermore, the self-healing behaviour was detected up to a specific sample thickness/bullet

diameter ratio (t/d). Similar results were obtained in tests at mid bullet speed; in this case an extension of the melted zone was also observed.

Conversely, in hypervelocity tests, a completely different morphology of the damaged areas was detected. Melting of the material in the impact zones occurred still maintaining in some condition an effective self-healing behaviour. The promising self-healing response after hypervelocity impact tests suggests to consider the use of ionomers in multi-layer composite materials for space applications such as inflatable structures.

Material heating during bullet puncture may be the result of different contributions such as strain energy dissipation, bullet friction and heat conduction from bullet to polymer. In order to get information about the relevance of thermal effects due to viscoplastic dissipation, tensile tests were performed at different strain rates and temperatures. In room temperature tests, samples were also observed with an IR camera in order to assess the variation of temperature during stretching. Even though strain rates employed in tensile tests were consistently lower than those experienced by the material during bullet impact a remarkable temperature increase was observed, which suggests a strong interdependence between thermal/mechanical behaviour and healing capacity.

2.2 Experimental

2.2.1 Materials

Several grades of ionomers are commercially available, which differ in the percentage and kind of cations used for acid group neutralization (e.g. sodium, zinc, magnesium and lithium). In this work an ionomer based on ethylene-co-methacrylic acid copolymer, provided by DuPont® in pelletized form, was used (grade Surlyn® 8940). This ionomer is characterized by a content of 5.4 mol% acid groups, 30% of which neutralized with Na ions; its measured density and melting temperature are 0.95 g/cm^3 and 94 °C, respectively.

A hot press was used for the production of square plates (120x120 mm) with variable thickness from 0.5 up to 5±0.2 mm; the temperature of the mould was set at 180 °C and a moulding pressure of 5 bars was employed with a cooling rate of about 20 °C/min; the pressure was maintained during cooling stage, until the removal of samples. Prior to production, the material was dried under vacuum at 60 °C for 5 hours.

Dog-bone specimens for tensile tests, according to ASTM D1708, were obtained from plates with 2 mm thickness. For bullet puncture tests, instead, square plates of different thickness were used.

Before tensile and ballistic tests, the specimens were stored in a controlled environmental chamber at 23 °C for 30 days in order to reach stable mechanical properties after aging [126,128, 129].

2.2.2 Tensile tests

Two different sets of tensile tests were performed. The first set investigated the rate dependency of stress-strain curves and the temperature rise in the material during uniaxial tensile tests. In these tests, force-displacement curves at 23 °C were obtained with an MTS 858 testing system. Employed crosshead speeds ranged from 0.1 mm/s to 500 mm/s, corresponding to strain rates from $4.5 \cdot 10^{-3}$ s^{-1} to 22.7 s^{-1}. An infrared (IR) camera, Nikon S270 model, was used to monitor the temperature variation of the specimens during the experiments. The second set was aimed at verifying the dependence of mechanical properties both on temperature and strain rate. In this case, uniaxial tensile stress-strain curves in a temperatures range varying from -40 °C to 60 °C were recorded with an Instron 4302, equipped with an Environmental Chamber 3119 including a liquid nitrogen cooling system. The crosshead speeds employed ranged from 10 mm/min to 500 mm/min, corresponding to strain rates from $7.5 \cdot 10^{-3}$ s^{-1} to $3.8 \cdot 10^{-1}$ s^{-1}. This second set of uniaxial tensile tests was also aimed at validating the Ree-Eyring model for yielding stress, extending previous results obtained by Scogna et al. [126].

2.2.3 Ballistic Tests

Three different types of ballistic tests were carried out: the first test investigated self- healing ability of studied material after a low velocity impact, while the second explored the ability to repair a damage following an impact at mid velocity. The last set of tests was aimed to study the self-healing response after impact at hypervelocity, a typical impact condition of the space environment consequent to the impact of micrometeoroids or debris.

The low velocity tests were performed by shooting steel balls of different sizes using an air gun; this firing system allows to obtain a bullet velocity of about 180±5 m/s. Actual bullet speed was measured using a Phantom v5.1 high-speed digital camera. Several tests were performed varying sphere diameter from 2.5 to 14.4±0.15 mm and target samples thickness from 0.6 to 2.6±0.2 mm.

Tests at mid velocity speed were carried out in a shooting lab; steel spheres with a diameter ranging from 1.5 to 7.5±0.1 mm were fired with a shotgun, model Hatsan Optima, on samples with thickness of 0.5, 1, 2 and 3±0.2 mm. The resulting speeds of spheres varied between 380 m/s

and 440 m/s. In this case, projectile velocity was measured using an optical chronograph, model CED M2 Millennium.

Hypervelocity impact tests were performed at CISAS - Hypervelocity Impact Facility at Padova University, using a two-stage Light-Gas Gun (LGG) [130]. Velocities from 2 to 4 km/s, and target samples with thickness of 2, 3 and 5±0.1 mm were explored. In this case, aluminium spheres with equal diameter of 1.5 mm were fired.

2.2.4 Healing evaluation

The healing evaluation after ballistic tests was performed using two different techniques: microscopic observation and leakage test. The impact areas of all specimens were observed using an Hitachi Ltd., model TM-3000 scanning electron microscope. Both bullet entrance and exit sides were analysed in order to verify the hole closure and to evaluate the morphology of damaged surfaces. To better investigate the grade of healing, pressure leakage tests were also executed using a specific-designed device developed for this purpose (Figure 2.1). The close chamber of the experimental system was sealed with the sample and a pressure gradient of 0.9 bar was applied by a vacuum pump. When the hole was healed, no appreciable vacuum decay was detected compared to not punctured specimens during an observation time up to 15 minutes, while non-healed samples showed a vacuum decay within few seconds.

Figure 2.1: Air-flow test device.

2.3 Results and discussion

2.3.1 Tensile tests

Tensile tests of ionomeric samples were performed at different temperatures and strain rates. The first set of tests was performed at room temperature and at varying strain rate. An IR camera was also used in order to measure temperature variations of tested samples during stretching. Obtained results revealed a marked dependence of the mechanical behaviour of studied material on strain rate; in particular an increase in the deformation rate gives an increase in the instantaneous Young modulus, yield and post yield stress level. A decrease of strain at break was, instead, detected.

In specimens stretched to highest strain rate, a remarkable heating effect due to the dissipated deformation energy was detected, with increase of temperature up to 32 °C. All specimen presented extensive plastic deformation with strain at break always exceeding 190 %. Observing specimens through IR camera during tensile tests (Figure 2.2), it seems that the temperature is homogenous throughout samples suggesting an equally homogenously distributed plastic deformation.

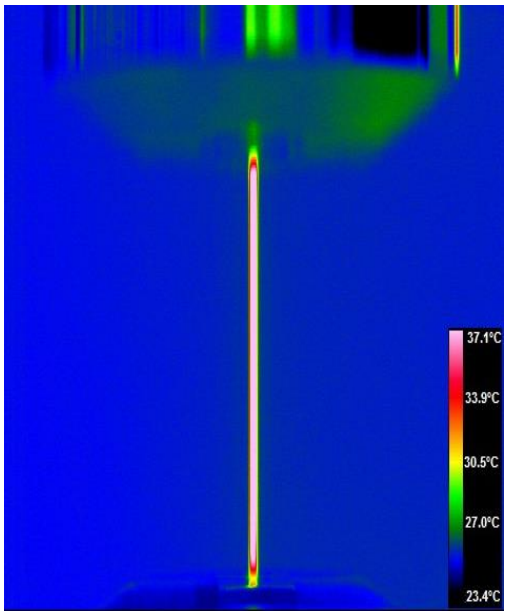

Figure 2.2: IR camera frame during tensile test.

In Figure 2.3 the evolution of temperature in tested samples at the different strain rate is presented; in the same figure, the resulting stress-strain curves are superposed. It can be observed that on increasing strain rate and corresponding temperature the “strain hardening”

progressively reduces; a thermal softening effect is apparent. However, it is expected that specimen temperature is affected by heat transmission from the sample to the external environment by convection and conduction, which cannot be avoided.

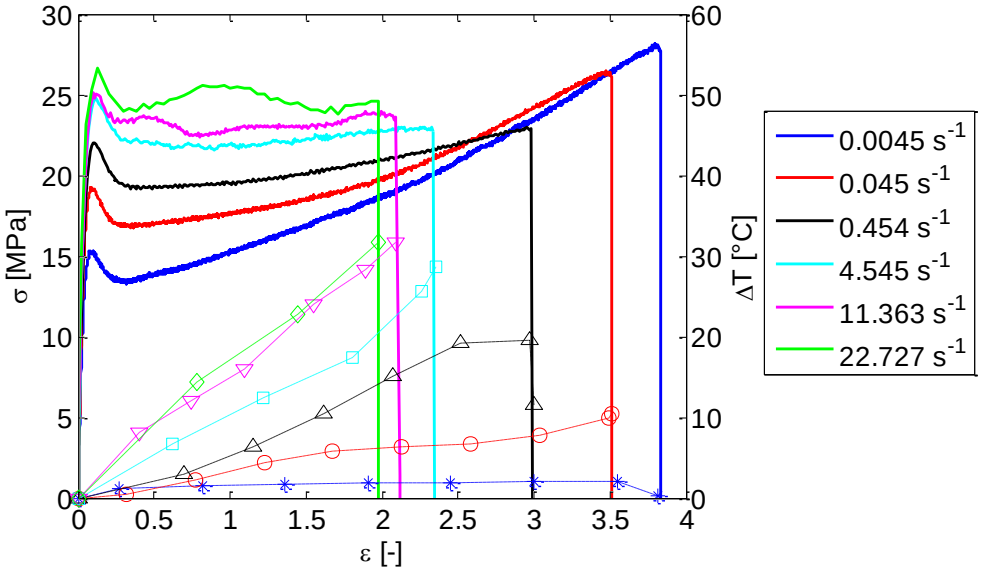

Figure 2.3: Temperature rise superposed on stress-strain curve for tensile test at different strain rates at room temperature.

In order to study in depth the yielding and breaking behaviour of the material, tensile tests at different temperature and different, but lower, strain rates were also performed. In these experiments, the actual temperature of the sample can be considered equal to the one set in the environmental chamber due to low applied strain rates. An example of the temperature dependence of stress-strain curves at a strain rate of 0.136 s^{-1} is reported in Figure 2.4.

As expected, mechanical properties such as the instantaneous Young modulus and the yield stress, decrease with increasing temperature. A change in the fracture behaviour was also noticed during the tests: at -40°C an abrupt break occurs immediately after necking, while at higher temperatures consistent flow takes place and a viscoplastic behaviour is promoted. An interesting observation is that the increase of temperature from -40 °C leads to a continuous increase of the ultimate deformation and reduction of ultimate stress up to 40 °C.

At 60 °C the opposite trend was observed and a change in morphology underlined by the whitening of the specimen (Figure 2.5) was evidenced; an easier strain induced crystallization process due to stretching and chains alignment probably occurred. Moreover, at this temperature a peak stress at yielding point is not so evident as at lower temperatures because the transition

related to the melting of secondary crystals has already happened and aging effects were not presented [126,128,129].

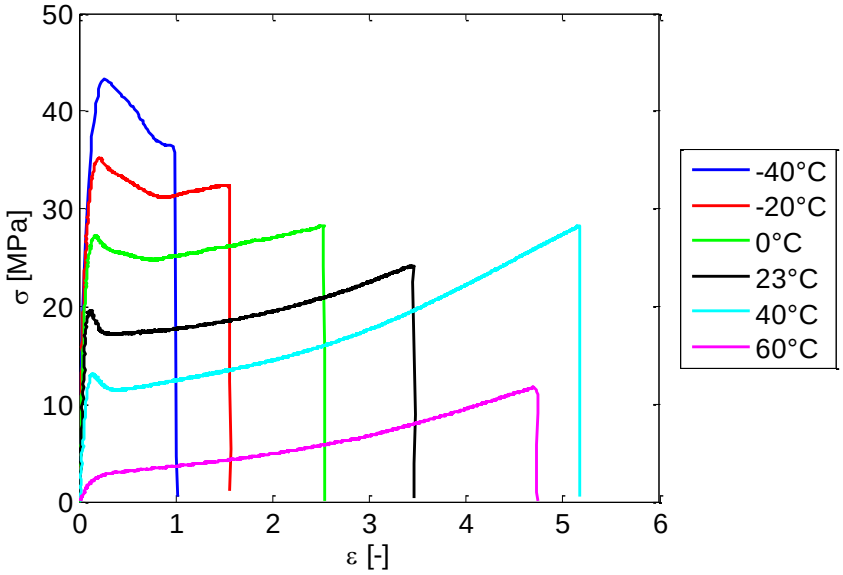

Figure 2.4: Stress-strain curves at different temperature at strain rate of 0.136 s^{-1}.

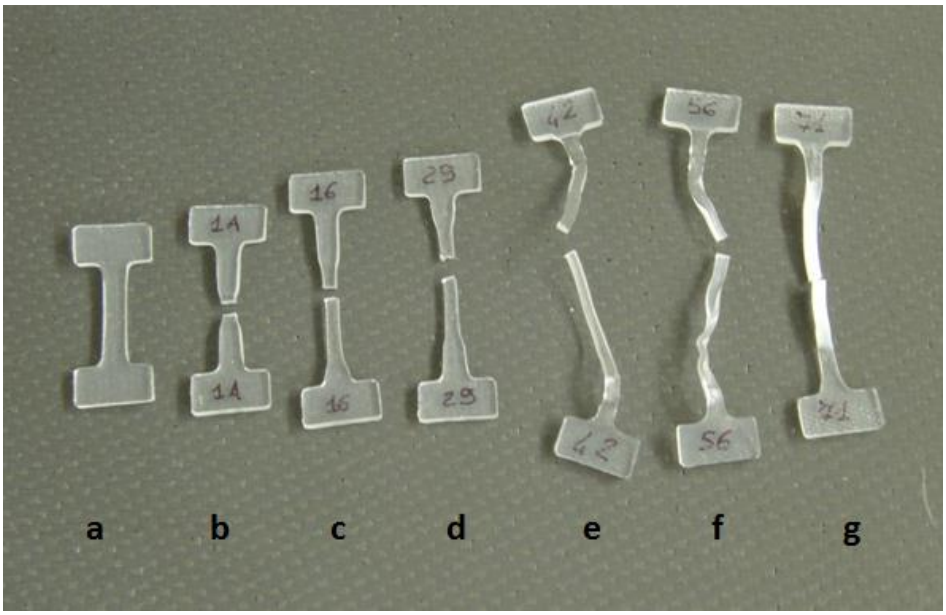

Figure 2.5: Evolution of type of fracture with temperature: untested sample (a), -40 °C (b), -20 °C (c), 0 °C (d), 23 °C (e), 40 °C (f) and 60 °C (g).

The yield stress values resulting from this last set of tests performed at different temperatures and strain rates were determined as the local maximum of stress-strain curves; results are shown in Figure 2.6.

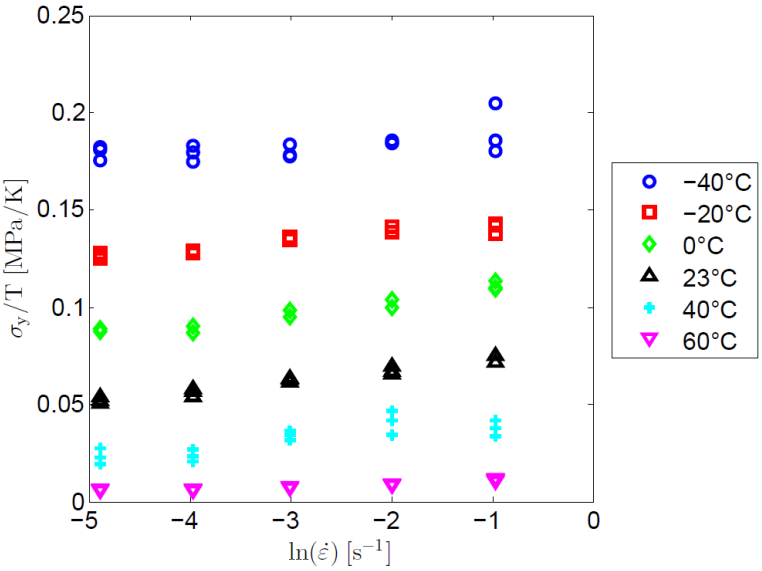

Figure 2.6: Measured yield stress at various strain rates and the temperatures.

Assuming that a single relaxation process is involved, the yield stress was modelled with the Ree-Eyring equation:

$$\frac{\sigma_y}{T} = \frac{R}{v} sinh^{-1}\left[\frac{\dot{\varepsilon}}{\dot{\varepsilon}_0}\exp\left(\frac{\Delta H}{RT}\right)\right] \tag{2.1}$$

where R is the gas constant, v is the activation volume, $\dot{\varepsilon}$ is the applied strain rate, $\dot{\varepsilon}_0$ is a constant pre-exponential factor, ΔH is the activation energy and T the absolute temperature. The results achieved by fitting the measured yield stress at different strain rates and temperatures with Ree-Eyring model are summarized in Table 2.1.

Table 2.1: Ree-Eyring model fit parameters.

v [nm^3]	ΔH [kJ/mol]	$\dot{\varepsilon}_0$ [s^{-1}]
5.00	190.16	$2.28 \cdot 10^{27}$

Exploiting the superposition principle is also possible to build a master curve which, selecting a reference temperature, describes the yield stress of the studied material over a wide range of strain rates; in particular the tests at lower temperature give an insight on the response of the material at higher strain rates, characteristic of ballistic impacts.

Data sets taken at various temperatures were superposed to create the master curve at the reference temperature ($T_{ref} = 23$ °C). The horizontal shift factors, s_x, are given by an Arrhenius expression:

$$s_x = -\frac{\Delta H}{R}\left(\frac{1}{T_{ref}} - \frac{1}{T}\right) \tag{2.2}$$

with activation energy ΔH obtained for the Ree-Eyring process. The master curve at the reference temperature is shown in Figure 2.7.

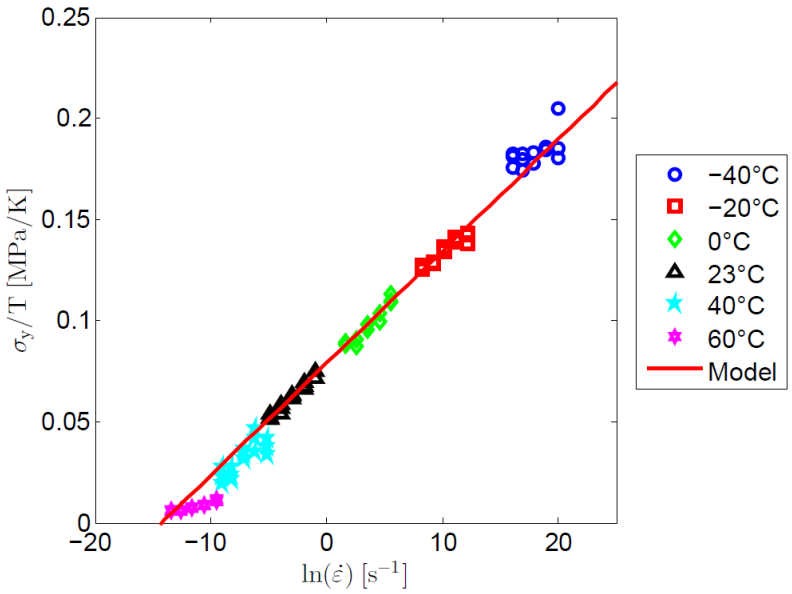

Figure 2.7: Obtained master curve at T_{ref} = 23 °C.

These results show how the stress-strain behaviour of studied material is deeply dependent on strain rate and temperature showing also a coupling between mechanical and thermal response when subjected to large deformations. Definitely, these interrelations may play an important role in the self-healing behaviour after ballistic impact of studied material; further analysis can give the necessary insight for a complete understanding of this phenomenon.

2.3.2 Low velocity impact tests

The low velocity impact tests, performed by firing steel spheres on EMAA-30Na plates, showed how this material is able to self-heal even under these experimental conditions. Tests were carried out varying the thickness of impacted plates and the diameter of fired balls. The velocity of the spheres was set at 180 m/s for all performed tests. The healing was tested applying pressure difference in the damage zone and following vacuum decay. Sealed samples did not show an appreciable variation of pressure over time, otherwise, in the unrepaired specimens, vacuum decay was instantaneously recorded. These tests allowed to identify a critical ratio between sample thickness (t) and bullet diameter (d) below which full repair was not observed. This ratio can be recognized as a peculiar parameter to discriminate the impact behaviour of flat panels. Results presented in Table 2.2 show how above a 0.2 t/d ratio a complete self-healing behaviour is well maintained; on the other hand, below this specific ratio, an effective hole closure did not occur. Pictures of a specimen entry side after low velocity bullet impact are presented in Figure 2.8.

Table 2.2: Low velocity impact test results (no Self-Healing for shaded cells);
t = sample thickness [mm], d = sphere diameter [mm].

		Sphere diameter [mm]							
	t/d [-]	**2.35**	**3**	**5**	**6.34**	**8**	**10**	**12**	**14.27**
Thickness [mm]	**0.6**	0.26	0.20	0.12	0.09	0.08	0.06	0.05	0.04
	1.0	0.43	0.33	0.20	0.16	0.13	0.10	0.08	0.07
	1.9	0.81	0.63	0.38	0.30	0.24	0.19	0.16	0.13
	2.6	1.11	0.87	0.52	0.41	0.33	0.26	0.22	0.18

Microscope analysis after low velocity ballistic tests highlighted different morphologies of the impacted areas compared with those previously obtained in other studies; however, some similarities can be still recognized.

In the bullet entry side (Figure 2.9), it is possible to see radial striations in the direction of the impact point caused by plastic deformation both in healed and no healed samples.

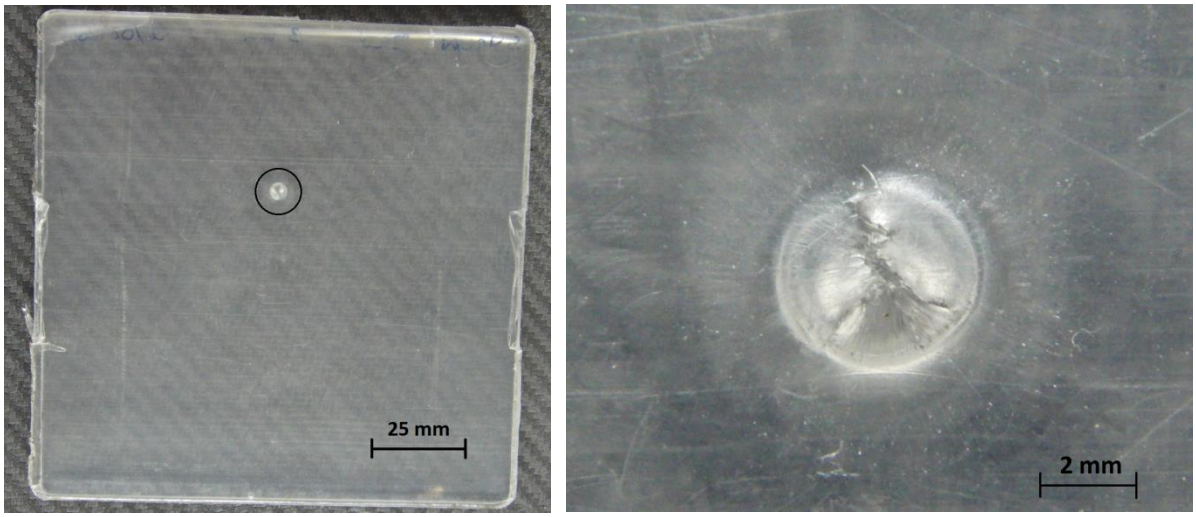

(a) (b)

Figure 2.8: Optical images of the impacted area (entry side) in a repaired sample, t = 3 mm, d = 12 mm tested at low velocity.

Some significant differences in the response of the material after impact were detected; the morphology of the damaged area in healed samples presented petaling phenomenon (Figure 2.9-a, Figure 2.10-a) with a melted zones on the apex of the petals (Figure 2.10-b).

These melted areas, even if small, are responsible for the sealing of the hole caused by the bullet, thus becoming a crucial factor for the global self-healing behaviour exhibited by the studied material.

On the other hand, non- healed samples present a circular hole with clearly defined edges (Figure 2.9-b), which evidence removal of material preventing the repair. Regarding the exit side, healed samples show the same petal morphology although a clear melted zone is not detectable (Figure 2.11-a): this behaviour suggests that in the entry side an additional contribution to temperature increment may derive from the friction forces between bullet and impact surface; such friction is expected to be lower in the exit side as consequence of material deformation. Unrepaired samples present instead morphology quite similar to that presented in the entry side (Figure 2.11-b).

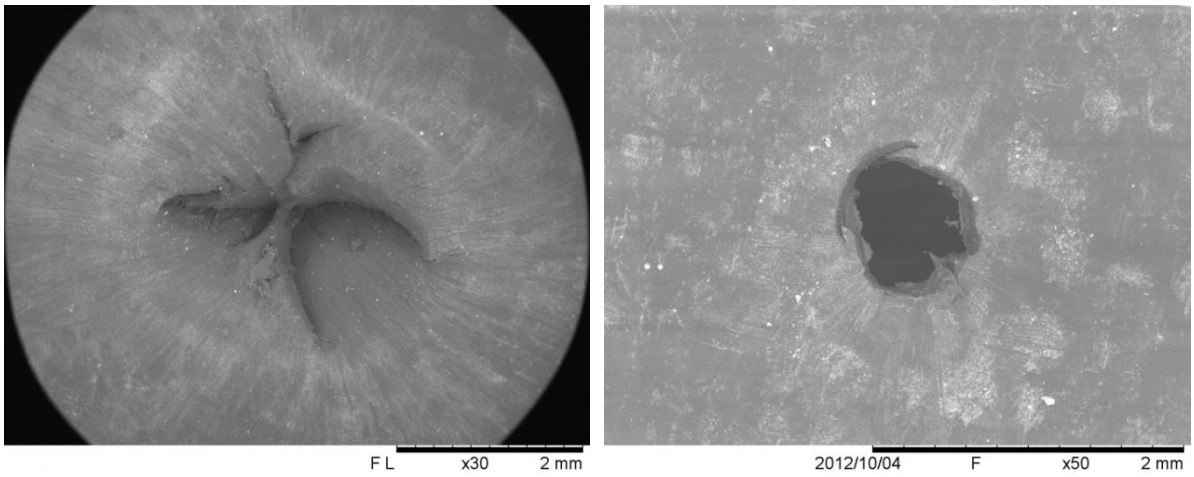

(a) (b)

Figure 2.9: Entry side in a repaired sample (a), t = 1.9 mm, d = 8 mm, and unrepaired sample (b), t = 0.6 mm, d = 3 mm, tested at low velocity.

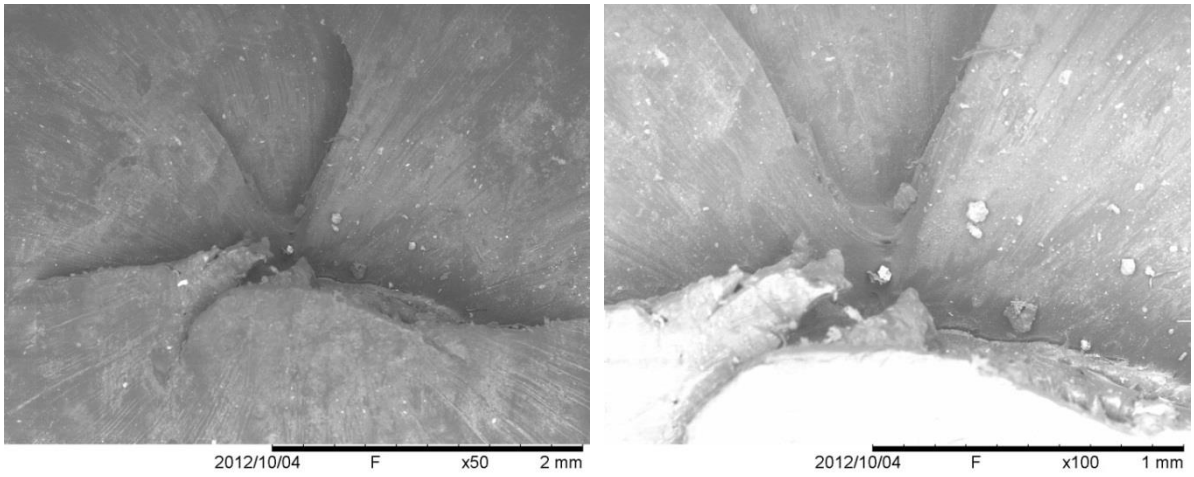

(a) (b)

Figure 2.10: Entry side in a repaired sample, t = 2.6 mm, d = 10 mm, 50x magnification (a) and 100x magnification (b), tested at low velocity.

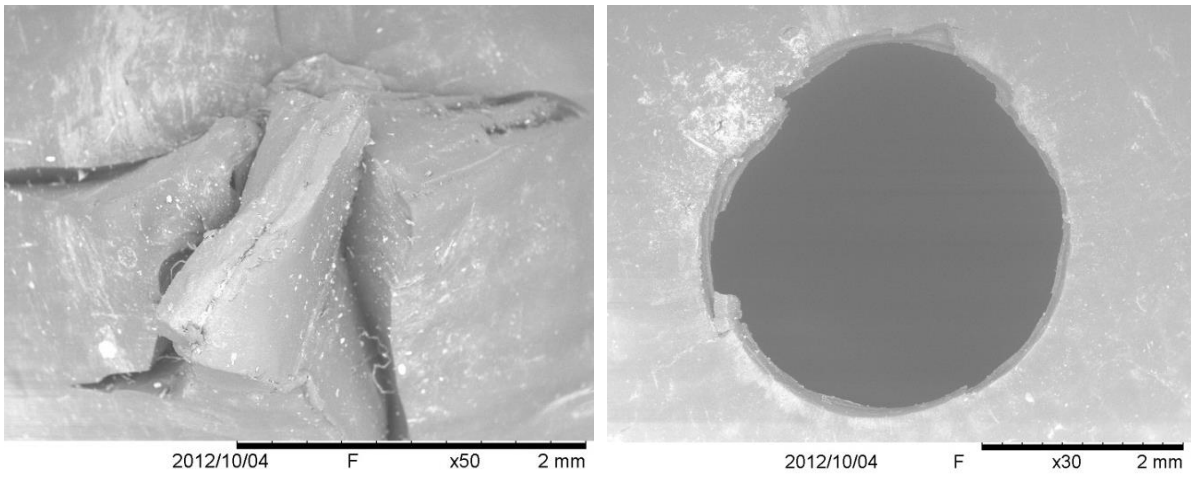

(a) (b)

Figure 2.11: Exit side in a repaired sample (a), t = 2.6 mm, d = 10 mm, and unrepaired sample (b), t = 1 mm, d = 5 mm, tested at low velocity.

Furthermore, thermal analysis performed during impact allowed to evaluate temperature evolution and extension of the damaged area in the specimen (Figure 2.12). In a circular region with a diameter equal to about 6.5 mm an instantaneous temperature increment was recorded. Maximum measured temperature in this zone for impact at 180 m/s was 119.6 °C, well above the melting temperature of the polymer (94 °C). Therefore, it is possible to affirm that also a ballistic test at low speed provides enough energy to melt the material and promote an effective sealing of the hole produced by a projectile.

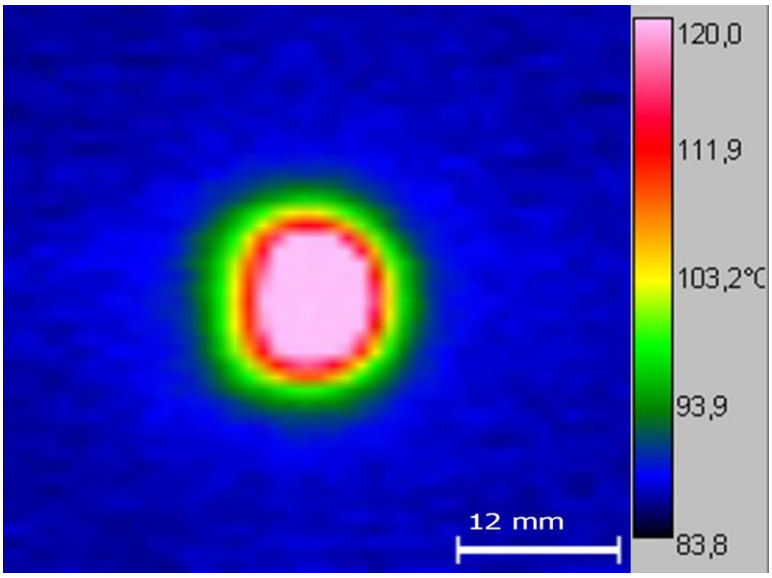

Figure 2.12: Measured temperature during low velocity impact (projectile enter side), t = 2 mm, d = 10 mm.

Analysing the frames recorded by the IR camera, it is also possible to obtain the temperature evolution with time in the impacted area (Figure 2.13). Immediately after the impact, the temperature dropped in less than 0.5 s from the maximum reached (about 120 °C) to 90 °C. The self-sealing phenomenon is therefore very rapid, and can be explained as an instantaneous melting of the damaged area and an equally quick solidification of the same region.

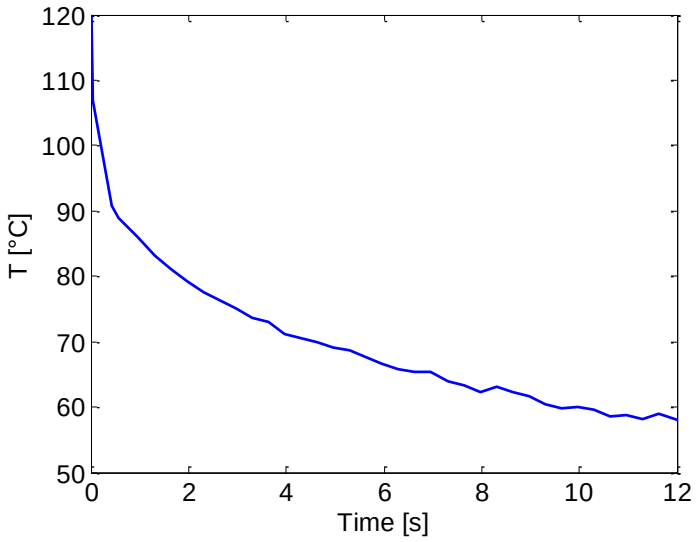

Figure 2.13: Temperature evolution at impact site after projectile passage.

However, it is important to underline that the temperature measured by the IR camera correspond to the actual temperature of the surface of the sample. From the micrographs, it can be assumed a higher temperature in the area of impact with respect to the projectile output zone mainly due to the friction forces generated. Moreover, the supply heat due to deformation energy conversion is not negligible, as shown by the performed tensile tests.

Further analysis are required to better understand the roles and the weights of the different phenomena occurring during a high energy impact and during the subsequently healing event in the studied material.

2.3.3 Mid velocity impact tests

In these tests, as in the previous case, steel spheres of different diameter were fired on square samples with thickness varying between 0.5 and 3±0.2 mm; results of mid velocity impact tests are presented in Table 2.3. Also at this impact speed, a critical t/d ratio, between 0.3 and 0.4, can be valued, below which self-healing behaviour did not appear. In few cases, a clear distinction

between complete or partial hole closure is not possible: about the 50% of thin samples (0.5 mm) fired with 1.5 and 2.5 show an effective repair.

Table 2.3: Mid velocity impact test results (no or partial Self-Healing for shaded cells); t = sample thickness [mm], d = sphere diameter [mm].

		Sphere diameter [mm]					
	t/d [-]	**1.5**	**2.5**	**3.9**	**4.5**	**6.2**	**7.5**
Thickness [mm]	**0.5**	0.33	0.20	0.13	0.11	0.08	0.07
	1.0	0.67	0.40	0.26	0.22	0.16	0.13
	2.0	1.33	0.80	0.51	0.44	0.32	0.27
	3.0	2.00	1.20	0.77	0.67	0.48	0.40

no SH

50% SH

For repaired samples, SEM analysis revealed morphology of the impact sites with a clear melted zone in the centre of the crater and radial striations due to extensive deformation (Figure 2.14-a). On the other hand, unrepaired sample present clear-cut holes similar to those obtained after low velocity impacts. However, in some cases a competition between these two failure modes occurred. In Figure 2.14-b both a clear break and a melted zone still attached to the material removed by the projectile impact can be observed.

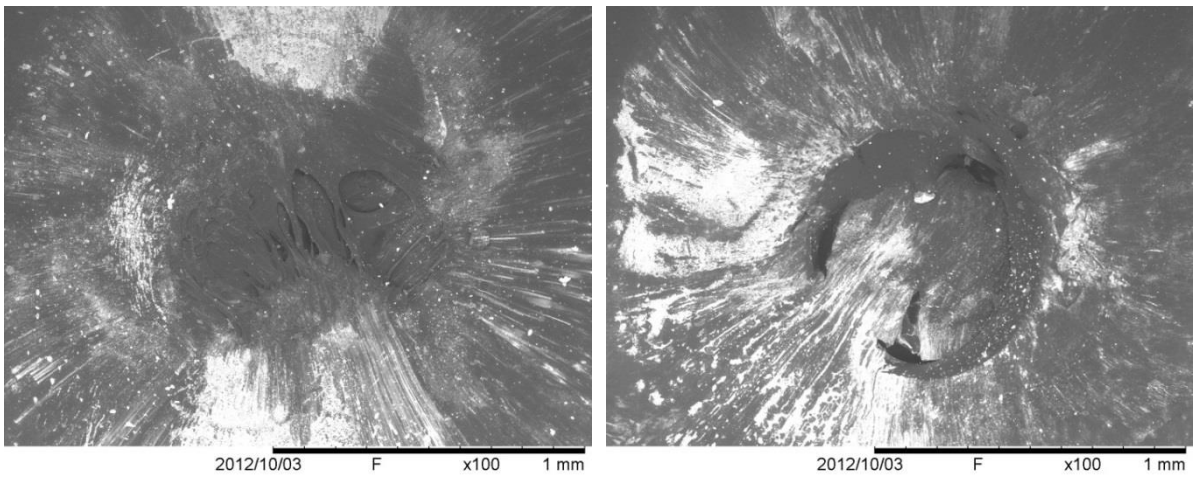

(a) (b)

Figure 2.14: Entry side in a repaired sample (a), t = 1 mm, d = 1.5 mm, and unrepaired sample (b), t = 0.5 mm, d = 1.5 mm, tested at mid velocity.

2.3.4 Hypervelocity impact tests

Impact experiments performed at hypervelocity with 1.5 mm diameter spheres prove the healing behaviour of EMAA-30Na at the two tested speed ranges, i.e. 2 km/s and 4 km/s; results are summarized in Table 2.4. At the lowest projectile velocity, 2 km/s, all ionomeric samples visually exhibited complete hole closure, but leakage tests showed a loss of pressure of the 3 mm thick specimen. Conversely, at the highest bullet speed, 4 km/s, only the 3 and 5 mm thick samples exhibited complete hole closure.

Table 2.4: Hypervelocity impact test results.

Diameter [mm]	Velocity [km/s]	Thickness [mm]	t/d [-]	Healing (hole closure)	Healing (leakage test)
1.5	1.93	2	1.33	Yes	Yes
1.5	1.80	3	2.00	Yes	No
1.5	1.64	5	3.33	Yes	Yes
1.5	3.90	2	1.33	No	No
1.5	4.00	3	2.00	Yes	Yes
1.5	4.10	5	3.33	Yes	Yes

Morphological analysis after hypervelocity tests showed a completely different conformation of the impacted sites from those previously analysed; some differences were also detected among the various tested samples. In all tested plates, on the inlet side, debris of the fired aluminium sphere can be observed, nevertheless on the other side no residues of the projectile were detected (Figure 2.15-9).

Samples of 2 mm thickness impacted at 2 km/s and samples of 2 and 3 mm thickness impacted at the highest speed presented the same morphology of the damaged area. The bullet entry zones show an indented surface (Figure 2.15-a, Figure 2.16-.a and Figure 2.17-a); on the other hand, the morphology of the impact area on the back part of these samples exhibit a clearly defined melted zone of approximately the same diameter as spherical projectile in the first case (Figure 2.15-b) and of about 4 mm in the second case (Figure 2.16-b, Figure 2.17-b). In addition, the presence of voids caused probably by the generation of volatile substances during the impact, can be inferred from observations. All other tested samples show an impact crater with similar characteristics both in the entry and exit sides. As presented in Figure 2.18, on each side a melted zone can be observed together with some filaments of flowed polymer starting from the impact site.

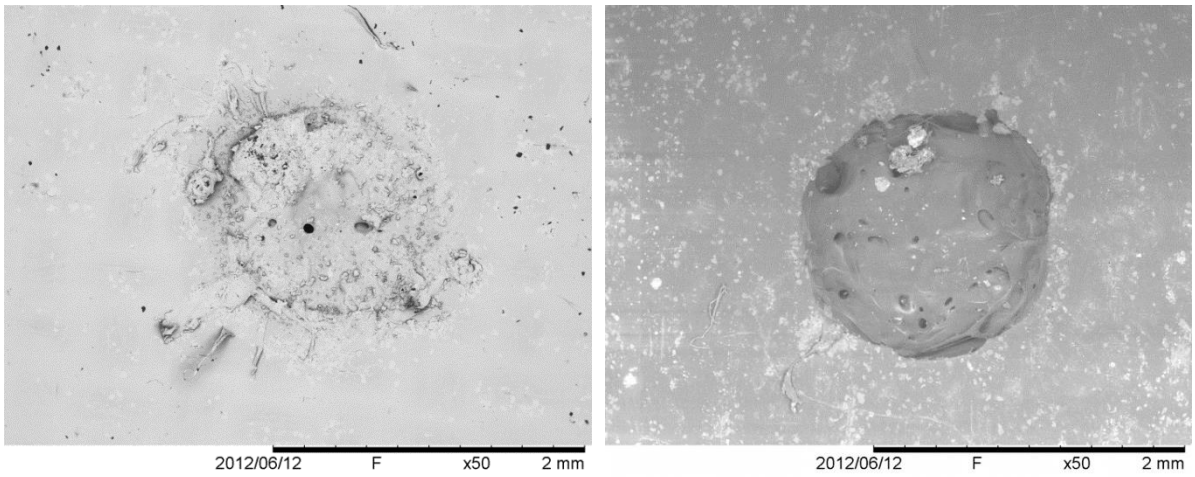

(a) (b)

Figure 2.15: 2 mm thickness sample tested at 2 km/s, entry side (a), exit side (b).

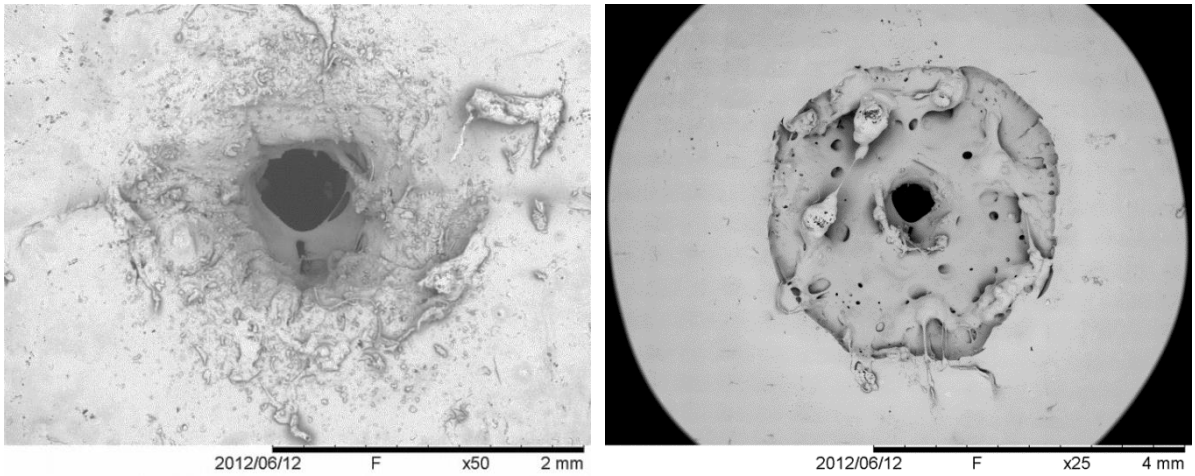

(a) (b)

Figure 2.16: 2 mm thickness sample tested at 4 km/s, entry side (a), exit side (b).

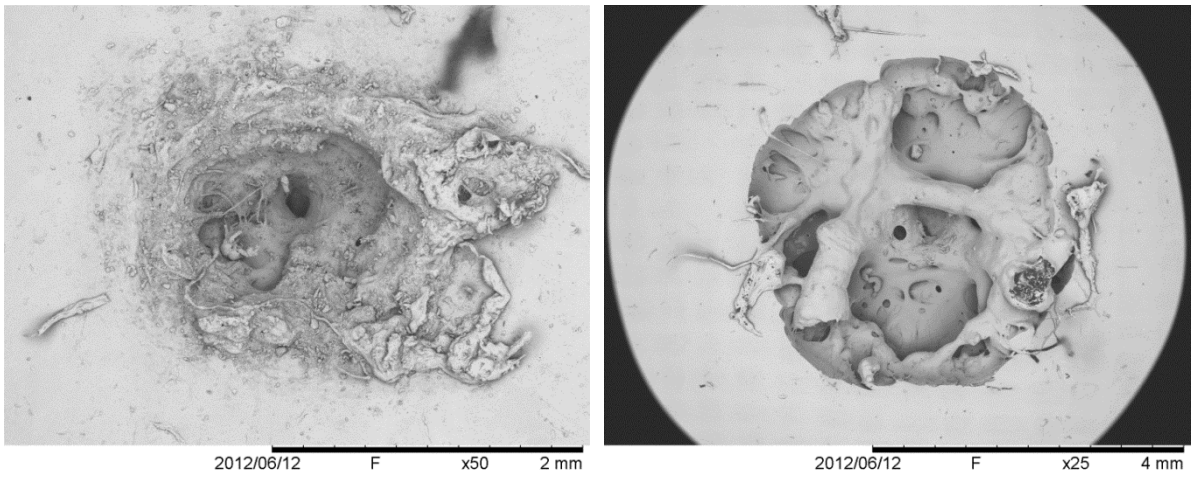

(a) (b)

Figure 2.17: 3 mm thickness sample tested at 4 km/s, entry side (a), exit side (b).

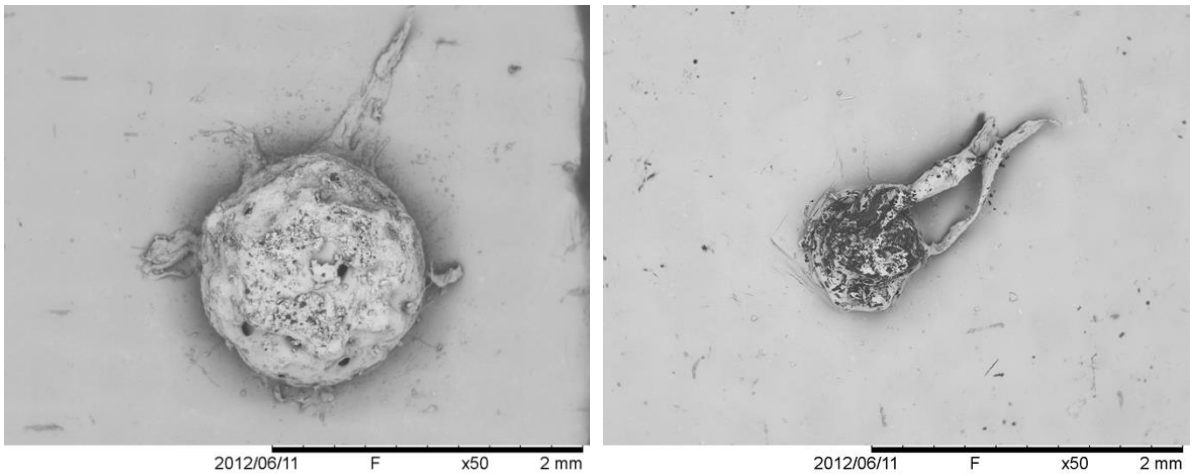

(a) (b)

Figure 2.18: 3 mm thickness sample tested at 2 km/s, entry side (a), exit side (b).

2.4 Conclusions

Self-healing behaviour after ballistic puncture tests and mechanical properties of EMAA-30Na ionomer were investigated under different experimental conditions. Impact tests were carried out firing spherical projectiles at different speeds ranging from low, 180 m/s, up to hypervelocity, 4 km/s. After ballistic tests, healing efficiency was checked by SEM micrographs and air leakage tests.

Apparently, at low velocity impact tests a clear melted zone is not detectable in both sides; however a more extensive microscopic analysis clarified the presence of small melted areas in bullet entry sides. An increase of temperature due to the plastic deformation and to bullet friction can be assumed according to the results obtained in mechanical tests. This rise in temperature during the bullet passage promoted the repair even for these low speed impacts allowing the hole sealing immediately after the elastic recovery. A critical t/d ratio of 0.2 for low velocity impact tests was found.

Mid velocity impact tests revealed instead a competition between two different failure behaviours; still, a critical t/d relationship was evidenced. Also in this case, the melting of the polymer in the area of impact plays an important role for the complete hole closure after projectile passage.

Moreover, hypervelocity tests showed the ability of studied material to self-heal even under these severe test conditions suggesting a possible use of EMAA-30Na in the space field. Microscope analyses after impact detected a complete different morphology of the damaged areas not comparable with the previous cases.

Mechanical tests and temperature recordings showed how the heat generated by plastic deformation may consistently give a fundamental contribution to the sealing of the hole after high energy impacts. Tensile tests performed at different strain rates allowed to evidence and measure the increment of temperature of specimens during the experiments.

Chapter 3 - Effect of Na neutralization on the self-healing behaviour of EMAA ionomers

3.1 Introduction

EMAA based ionomers have shown self-repairing capability after high-energy impact; a two stage model was suggest to explain the self-healing behaviour [70,71]: (i) initial elastic recovery and (ii) interdiffusion and sealing mechanism. It was also proven that ion content is not necessary for the healing behaviour after ballistic impacts [127] but it may affect the process efficiency.

Ionomers formation mechanism and multiplet-cluster model, early studied by Eisenberg et al. [131,132] and Tadano et al. [133], was further investigated by Han and Williams [134]. In their research, ionomers with different alkaline metal (Li, Na, K, Rb and Cs), alkaline earth metal (Mg, Ca, Sr and Ba) and transition metal (Cu and Zn) ions were produced and deeply analysed trough Fourier transform infrared spectroscopy (FTIR) experiments proving the existence of an additional ionomer formation mechanism.

Neutralization of acid group with metal cations (Figure 3.1) and related aggregation of these ionic groups are responsible of the complex morphology of EMAA based ionomers. In recent years, Wakabayashi et al. [135] proposed a nanostructure morphology including four distinct phases:

- thick primary crystals;
- small interlamellar crystallites;
- amorphous polyethylene chain segments;
- ionic aggregates.

Primary crystals, formed after cooling, and small crystallites (secondary crystal phase), growing during aging, lead to a dual melting behaviour [129]. This secondary crystal phase can also be observed in EMAA copolymers, however the amount is limited. In ionomers, instead, the fraction of crystallites is larger than in the previous case. By means of thermal annealing, Tsujita et al. [136] have also demonstrated the possibility to modify the melting behaviour of the secondary crystal phase in EMAA based ionomers. In particular, the melting peak connected to the small crystallites, observed in DSC experiments, can be shifted to higher temperature increasing annealing temperature and time. These results suggest the lack of physical cross-links, thus allowing molecular motion and re-organization of polymer chains.

Furthermore, Scogna et al. [125,126] and Spencer et al. [137] have recently studied the effects of metal cations neutralization of EMAA based ionomer on several physical properties obtaining similar results formerly presented by Hirasawa et al. [138] and Kohzaki et al. [139]. In these researches, both the tensile modulus and the yield strength increase with increasing neutralization level up to a critical level; rheological properties also increase with increasing ions content, however in this case, also MAA concentration plays an important role.

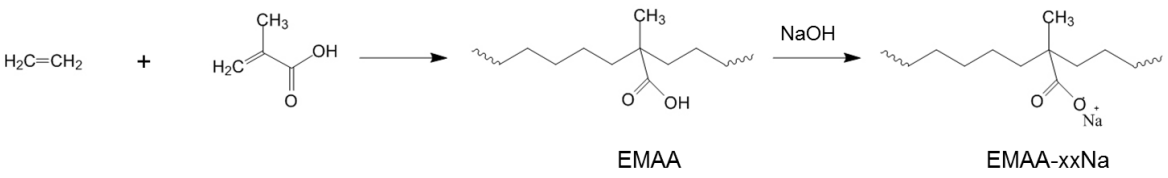

Figure 3.1: Acid groups neutralization by Na ions.

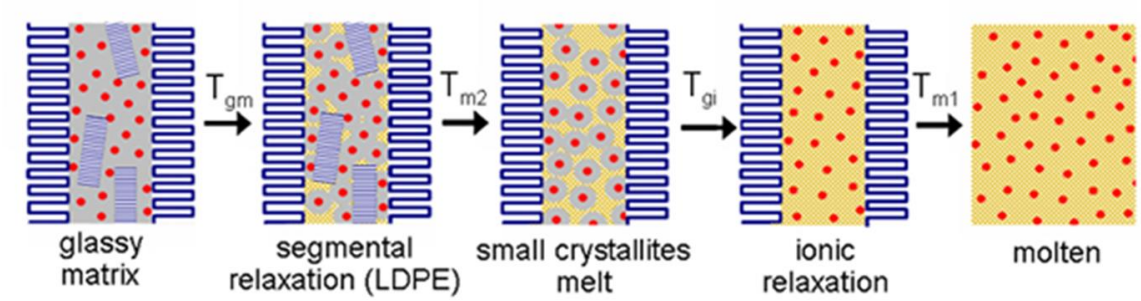

Figure 3.2: Morphology structure in EMAA ionomers [135].

From all presented research works, it can be deduced that metal ion type, neutralization level, aging time, processing condition and related thermal history strongly influence ionomer structure morphology. Thermo-mechanical and viscoelastic behaviour are then deeply dependent of such

complex morphology structure and it is therefore reasonable to assume also an influence on the global self-healing behaviour exhibited by EMAA based ionomers.

In this chapter the Na ionic content effects on nanostructure morphology, thermo-mechanical properties and self-healing capability has been investigated trough several experimental techniques. FTIR, small angle (SAXS) and wide-angle (WAXS) X-ray scattering analyses, aimed to study polymer nanostructure, were performed. Differential scanning calorimetry (DSC), rheological and tensile tests have been carried out to investigate thermal, viscoelastic and mechanical behaviour, respectively.

As in the previous chapter, the EMAA ionomers with different neutralization levels were also tested by ballistic impact experiments varying sample thickness, projectile speed and diameter. An example of tested specimens is presented in Figure 3.3. These experiments allowed to define a critical ratio between sample thickness and bullet diameter below which the SH behaviour does not appear. Obtained results show how the Na ions content influence the SH capability of studied materials, in particular the EMAA copolymer with the highest Na neutralization level does not show a complete hole closure after low velocity impact test. Conversely, increasing projectile speed, all the polymers exhibit nearly the same SH behaviour.

Healing efficiency was evaluated with the same pressure test protocol, optical and SEM investigations already presented (Chapter 2). These analyses revealed different characteristic features in the damaged zones of tested polymers impacted at different projectile speed.

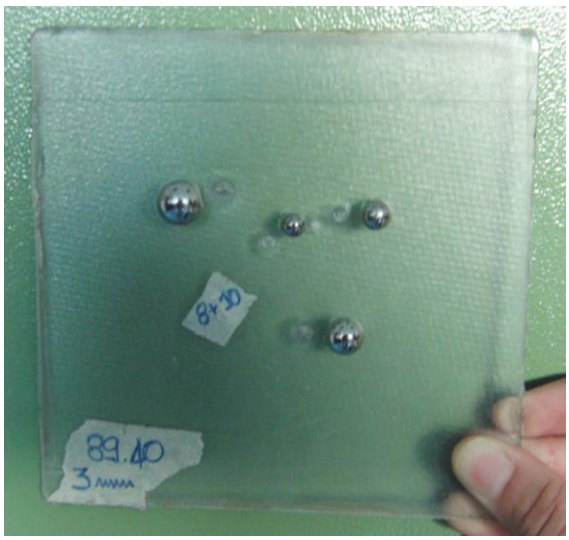

Figure 3.3: Example of specimen used in ballistic experiments.

3.2 Experimental section

3.2.1 Materials

EMAA based copolymers and ionomers are available on the market with different trade names (e.g. Nucrel® and Surlyn®). In this research an EMAA copolymer and a sodium ionomer were analysed. Pellets of the different polymers were supplied by DuPont®. All studied materials have the same acid part content, 5.4 mol%, with 0% (EMAA) and 60% (EMAA-60Na) of the acid groups neutralized by Na ions. Previous studied EMAA-30Na ionomer (Chapter 2) was also studied for comparison purpose. General properties provided by DuPont® are summarized in Table 3.1.

Table 3.1: Properties of EMAA based copolymer and ionomers.

Polymer	Density [g/cm^3]	Melting point [°C]	Melt flow index (190 °C) [g/10 min]
EMAA	0.94	91	60
EMAA-30Na	0.95	94	2.8
EMAA-60Na	0.95	88	0.9

After drying received pellets in vacuum at 60 °C for 5 hours, square samples (120x120 mm) of 0.5, 1, 2, 3±0.1 mm thickness were produced by compression moulding setting the mould temperature at 180 °C for all materials. Prior to testing, all specimens were stored in a controlled environmental chamber at 23 °C, low humidity, in order to avoid moisture effect.

3.2.2 Measurements

The self-healing capability of the different polymers was studied by impact experiments. Two different types of ballistic tests were carried out: low velocity impact and mid velocity at 180 m/s and 400 m/s respectively.

As in Chapter 2, metallic spheres of different diameters were fired on flat specimens with thickness ranging from 0.5 to 3.0±0.1 mm in order to evaluate the already presented critical value between sample thickness and projectile diameter. All impact tests were performed on samples aged for about 30 days.

After all experiments, the healing efficiency was evaluated by applying a pressure gradient; hole closure was tested by following vacuum decay. A morphology analysis of the impact zones was

also made observing all samples by optical microscope and SEM both in the bullet entrance and in the exit sides. Figure 3.4 presents collected micrographs of the same damaged zone obtained with the two different techniques.

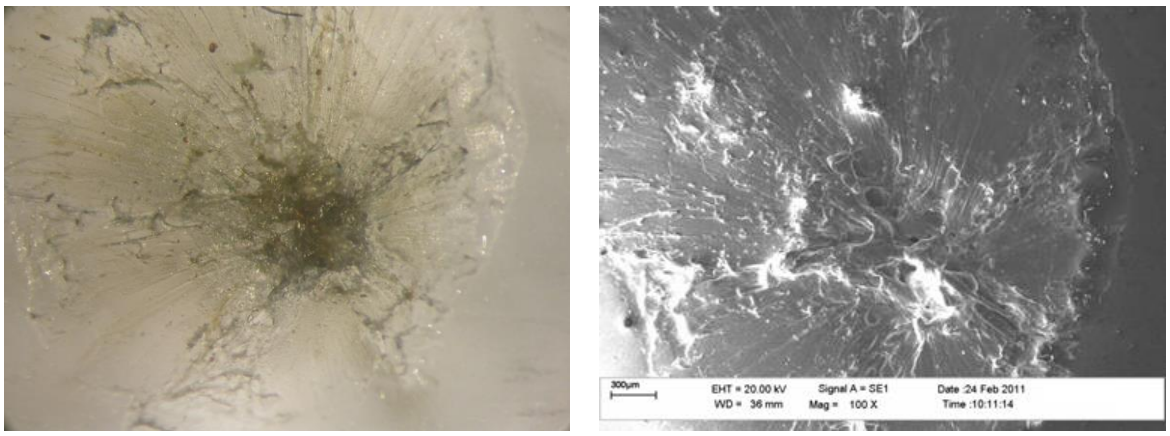

(a) (b)

Figure 3.4: Optical (a) and SEM (b) micrographs of a same impacted zone.

In order to explain and evaluate the difference in the self-healing behaviour exhibited by the three different polymers, several experimental techniques have been adopted.

FTIR tests were performed using a Perkin-Elmer Spectrum 100 FTIR. The spectra for the different polymers were obtained using 8 scans across a range of 4000 to 550 cm^{-1}. All the IR spectra were normalized using the peak at 2916 cm^{-1} related to the C-C bond. A background scan was performed before each series of experiments. Aged samples (30 days) were analysed.

X-ray diffraction studies were performed using a Bruker AXS D8 Discover diffractometer, all measurements were performed at room temperature using monochromatic Cu Kα radiation (λ = 0.1542 nm). Wide-angle XRD experiments were performed using a distance of 6 cm between the sample and the detector and setting the exposure time to 2 min. For SAXS analysis, the sample-detector distance was set at 30 cm and exposure time was set to 10 min. The samples for both WAXS and SAXS measured 1±0.1 mm thickness. The effect of aging time was also investigated testing 0, 1, 7 and 30 days aged samples. XRD experiments carried out by Varley and Kalista [140] at the Australian Synchrotron were also analysed.

A TA Instruments DSC Q100 was used to carried out DSC analysis in nitrogen atmosphere (50 ml/min); a heating/cooling rate of 10 °C/min was set for all DSC tests. Every polymers was tested in the temperature range between 20 °C and 120 °C. Measurements were conducted on 8-13 mg specimens encapsulated aluminium pans. A first heating/cooling cycle was performed to delete

any previous thermal history; samples were then tested after various aging time. Melting point and enthalpy for both primary and secondary crystal phase were determined as peak temperature and peak area of the endothermic peaks, respectively.

Dynamic mechanical thermal analysis (DMTA) was performed with two different systems. Dynamic tensile experiments were performed on rectangular samples using a Perkin Elmer Diamond DMTA instrument in a temperature range from -10 °C to 110 °C with a heating rate of 2 °C/min and at 1 Hz frequency. Shear storage modulus (G') and shear loss modulus (G'') measurements were instead obtained with TA Instruments AR-2000EX rheometer.

Rheological properties were investigated using the same rheometer equipped with parallels plates. Circular samples with 25 mm diameter and thickness of about 1 mm were analysed. Each specimen was tested in a frequency range from 0.1 Hz to 100 Hz and temperatures between 90 °C and 180 °C.

Uniaxial tensile tests were conducted following the same procedure presented in Chapter 2, moreover, the evolution of mechanical properties such as tensile modulus and yield stress were also studied performing experiments at various aging times.

3.3 Results and discussion

3.3.1 Impact tests

Ballistic impact test performed firing spherical projectile at low velocity and mid velocity allowed to identify in most of cases a critical ratio between sample thickness and bullet diameter below which self-healing behaviour did not appeared. Moreover, the tested materials exhibited a neutralization level and projectile speed dependent self-healing response.

EMAA copolymer, tested at low velocity impact speed, showed a self-repairing behaviour similar to the polymer with the 30% of acid groups neutralised with Na ions (paragraph 2.3.2). Results presented in Table 3.2 show how, also in this case, a ratio between sample thickness and projectile diameter of 0.2 t/d is required for an efficient self-healing. Below this critical ratio, a complete hole sealing did not occur.

Nevertheless, morphology analyses demonstrate a clear different feature of the impacted zones between non-neutralised (EMAA) and neutralised (EMAA-30Na) polymer: EMAA healed samples did not present petaling (Figure 3.5-a), which appeared instead in EMAA-30Na (Figure 2.9); a small melted zone in the central part of the damaged areas was detected in both cases. On the other

hand, in non-repaired samples a similar morphology between these two polymers was detected (Figure 3.5-b).

Table 3.2: EMAA low velocity impact test results (no Self-Healing for shaded cells).

		Sphere diameter [mm]							
	t/d [-]	**2.35**	**3**	**5**	**6.34**	**8**	**10**	**12**	**14.27**
Thickness [mm]	**0.5**	0.21	0.17	0.10	0.08	0.06	0.05	0.04	0.03
	1.0	0.43	0.33	0.20	0.16	0.12	0.10	0.08	0.07
	2.0	0.85	0.67	0.4	0.32	0.25	0.20	0.17	0.14
	3.0	1.28	1.00	0.6	0.47	0.37	0.30	0.25	0.21

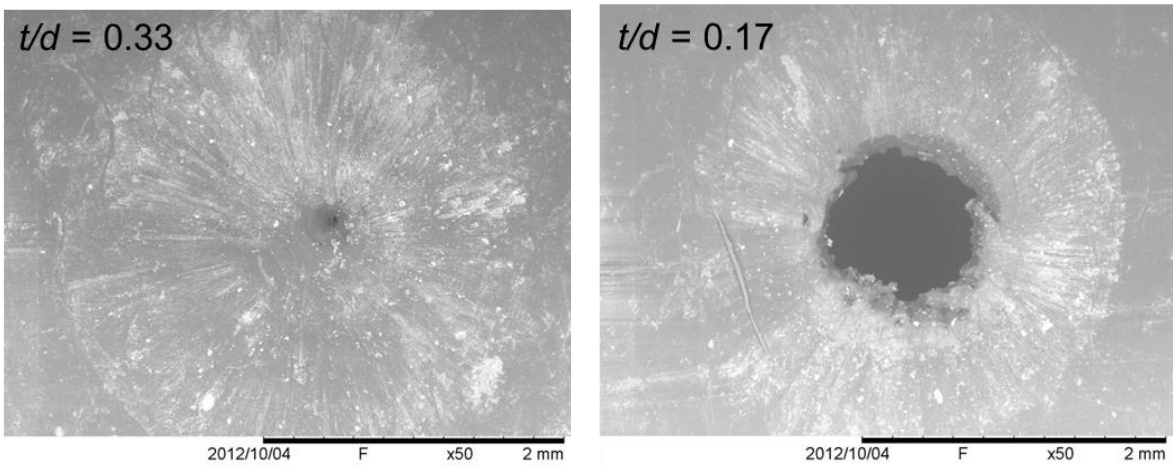

(a) (b)

Figure 3.5: SEM micrographs of EMAA healed (a) and non-healed samples (b) tested at low projectile velocity.

A completely different response was instead observed for EMAA-60Na. The ionomer with the highest neutralization level tested at low projectile impact velocity did not show any self-healing capability for all the t/d ratios (Table 3.3).

Observing damaged areas, this polymer shows a brittle fracture and material removal can be also assumed after most of the impacts (Figure 3.6-a); in few cases, in particular for low t/d ratios, the portion of the removed material remained for a small side still attached to the sample, as presented in Figure 3.6-b., Furthermore, in all the specimens a clear melted zone, required for an efficient sealing of the hole produced by bullet passage, cannot be detected. However, for the highest t/d ratios, hole reduction was observed.

Table 3.3: EMAA-60Na low velocity impact test results (no Self-Healing for shaded cells).

		Sphere diameter [mm]							
	t/d [-]	2.35	3	5	6.34	8	10	12	14.27
Thickness [mm]	0.5	0.21	0.17	0.10	0.08	0.06	0.05	0.04	0.03
	1.0	0.43	0.33	0.20	0.16	0.12	0.10	0.08	0.07
	2.0	0.85	0.67	0.4	0.32	0.25	0.20	0.17	0.14
	3.0	1.28	1.00	0.6	0.47	0.37	0.30	0.25	0.21

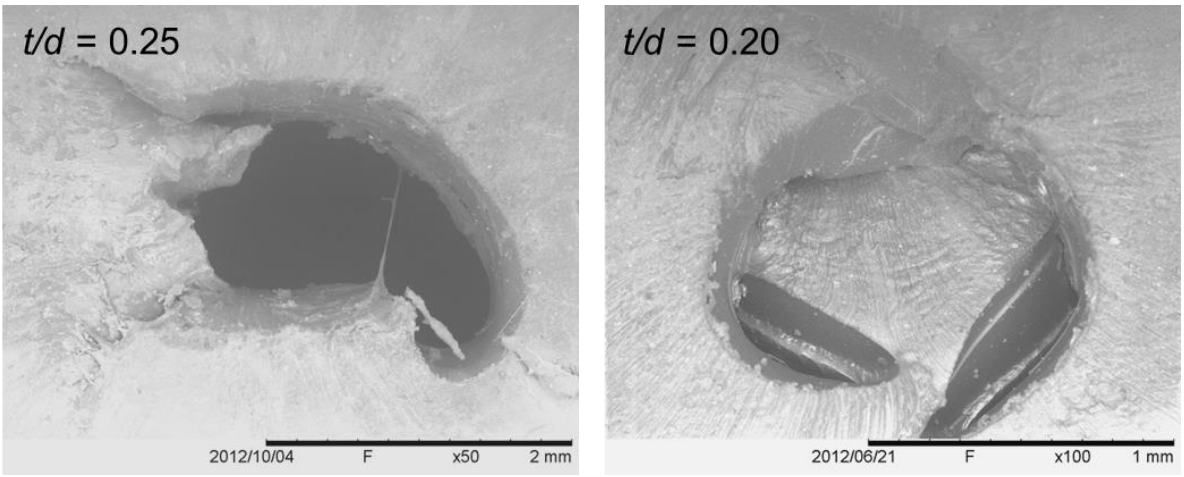

(a) (b)

Figure 3.6: EMAA-60Na tested at low projectile velocity.

Tests performed in the mid velocity projectile range (about 400 m/s) on EMAA copolymer confirmed a similar self-healing capability compared to EMAA-30Na with a critical t/d ratio of about 0.3 (Table 3.4). An extension of the melted zone due the impact (Figure 3.7-a) and substantial damage average diameter reduction (Figure 3.7-b) were also observed.

Table 3.4: EMAA mid velocity impact test results (no or partial Self-Healing for shaded cells).

		Sphere diameter [mm]					
	t/d [-]	1.5	2.5	3.9	4.5	6.2	7.5
Thickness [mm]	0.5	0.33	0.20	0.13	0.11	0.08	0.07
	1.0	0.67	0.40	0.26	0.22	0.16	0.13
	2.0	1.33	0.80	0.51	0.44	0.32	0.27
	3.0	2.00	1.20	0.77	0.67	0.48	0.40

no SH

50% SH

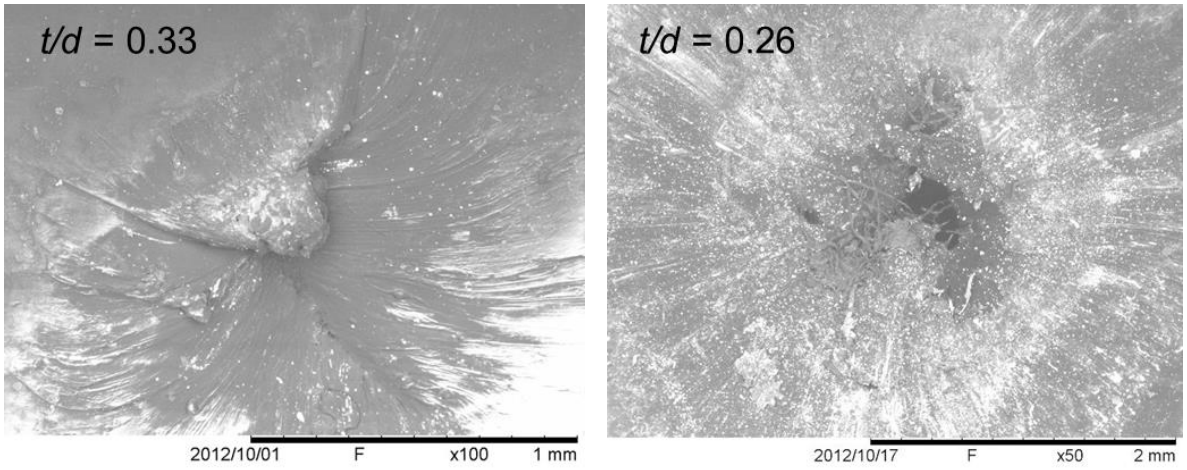

(a) (b)

Figure 3.7: EMAA samples at mid projectile velocity.

In similar way, also EMAA-60Na ionomer, which did not present self-healing capability at low projectile speed, exhibited an efficient hole sealing in these testing conditions for t/d ratios above a critical value of 0.3 (Table 3.5). Probably due to the greater energy transferred from the projectile during the impact, the melting of the material is adequate to allow the self-healing phenomenon. This hypothesis is supported by the SEM analysis of damaged areas. As shown by Figure 3.8-a, an extend melted zone is present in healed samples, whilst morphology analysis of not repaired specimens indicated, in some cases, a competition between brittle fracture failure mode and melting behaviour (Figure 3.8-b).

Table 3.5: EMAA-60Na mid velocity impact test results (no or partial Self-Healing for shaded cells).

		Sphere diameter [mm]					
	t/d [-]	**1.5**	**2.5**	**3.9**	**4.5**	**6.2**	**7.5**
Thickness [mm]	**0.5**	0.33	0.20	0.13	0.11	0.08	0.07
	1.0	0.67	0.40	0.26	0.22	0.16	0.13
	2.0	1.33	0.80	0.51	0.44	0.32	0.27
	3.0	2.00	1.20	0.77	0.67	0.48	0.40

no SH
50% SH

Obtained results highlight a different self-healing response after ballistic impact for the three EMAA based polymers with different sodium neutralization level. The most noticeable differences were observed after low velocity impact tests with a complete lack of capacity for the EMAA-60Na

ionomer. Conversely, at mid impact speed, despite a similar self-healing behaviour for all the polymers (almost equal critical t/d ratio), slight differences were found in the morphology of the damaged areas.

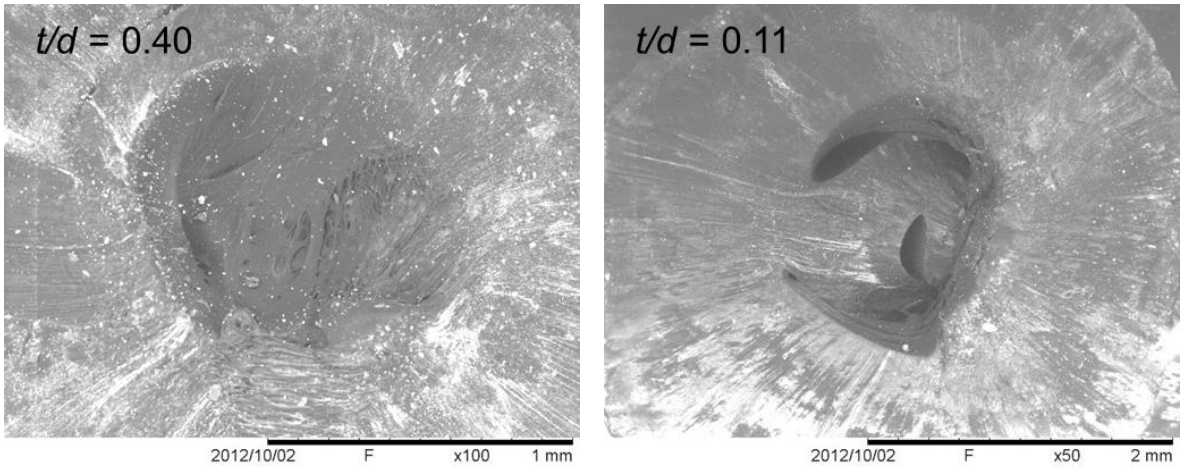

(a) (b)

Figure 3.8: EMAA-60Na samples tested at mid projectile velocity.

3.3.2 Microstructure characterization

Polymer structural characterization was carried out with two different techniques commonly adopted in material science: FTIR and XRD analysis.

Figure 3.9 shows the evolution of the FTIR spectra for the EMAA copolymer and EMAA-Na ionomers. The asymmetric methyl deformation peak at 1464 cm^{-1}, the methyl rocking peak at 719 cm^{-1}, and the peaks at 1407 and 1381 cm^{-1} [141,142] do not seem to undergo significant changes with the neutralization level, being this an indication that the main polymer backbone is not altered by this process. However, when neutralization takes place, there is a significant decrease in the absorption band of the carbonyl stretching vibration located at ~1697 cm^{-1} [143]. Moreover, the presence of Na cations in the polymer structure, introduces a new peak at about 1535 cm^{-1} assigned to the sodium neutralised carboxylic groups [142]. From the broad out-of-plane O-H bending peak at ~938 cm^{-1} it is clear that carboxylic acid groups exist predominantly as dimers in the polymer backbone as it was reported in a previous research [144]. The number of dimers is highly reduced in the Na ionomers with respect to the dimer content in the EMAA sample (peak becomes almost negligible at 938 cm^{-1}) even for the ionomer with the 30% of acid groups neutralised with sodium ions.

As demonstrated by WAXS/SAXS experiments, sodium neutralization has also significant effect on polymer crystal structure. Figure 3.10-a shows the WAXS spectra of the three EMAA based polymers. Both sodium ionomers show two WAXS peaks, the one at higher scattering angle corresponding to the primary polyethylene (PE) crystal, while the one at low angle corresponding to the scattering between ionic aggregates [125,145,146]. On the other hand, the copolymer do not exhibit the "ionic" peaks, as expected. Furthermore, there is a clear decrease in the XRD signal at high 2θ (20°) suggesting that the organization of PE crystals in the EMAA-Na ionomers is altered due to neutralization, in particular less-perfect crystal are presents.

The same trend was observed in SAXS experiments, where the peak at lower scattering angle, associated to small crystallites [146], decrease in intensity increasing neutralization level (Figure 3.10-b). Moreover, a broad peak, related ionic aggregates, was detected for the ionomers consistent with the results obtained in WAXS analyses.

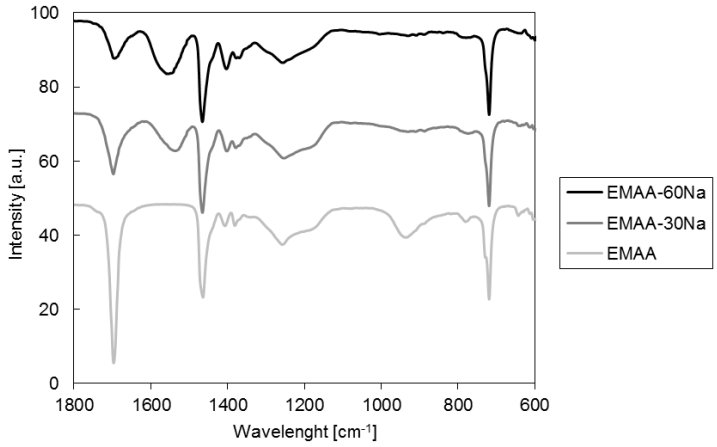

Figure 3.9: FTIR spectra.

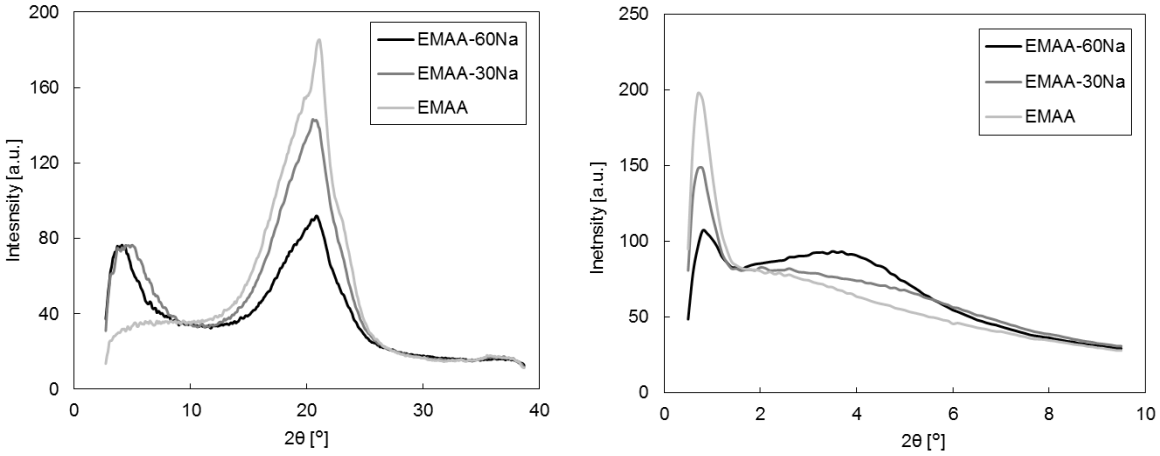

(a) (b)

Figure 3.10: WAXS (a) and SAXS (b) spectra.

In order to consolidate the dual crystal phase microstructure of these polymers, SAXS experiments performed by Varley and Kalista [140] at different temperature were also studied. In these tests the same polymers were investigated and a set of SAXS spectra was collected during sample heating/cooling from room temperature up to 120 °C at a constant heating rate. Figure 3.11 illustrates an example of SAXS data obtained during an experiment on the EMAA-30Na ionomer. From these SAXS data the position of the "crystallite" peak over time was extracted and the related scattering vector calculated as $q = (4\pi/\lambda)\sin\theta$, ($\lambda = 0.1032$ nm). This values is directly linked to the spacing between the scattering entities [146]. As shown in Figure 3.12, increasing the temperature the vector *q* decreases until the disappearance of the associated peak indicating the dissolution of the scattering entities (the secondary crystals) that reformed during cooling as soon as the crystallization temperature was reached.

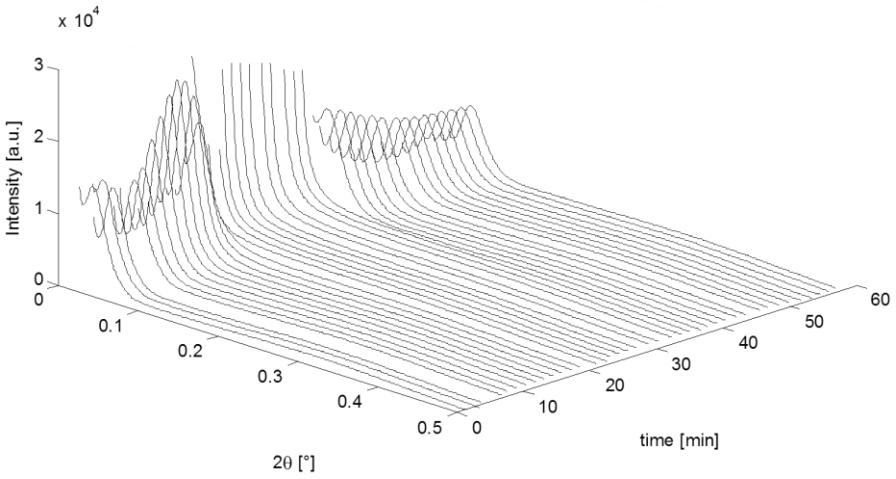

Figure 3.11: SAXS spectra of EMAA-30Na ionomer collected at different time/temperature.

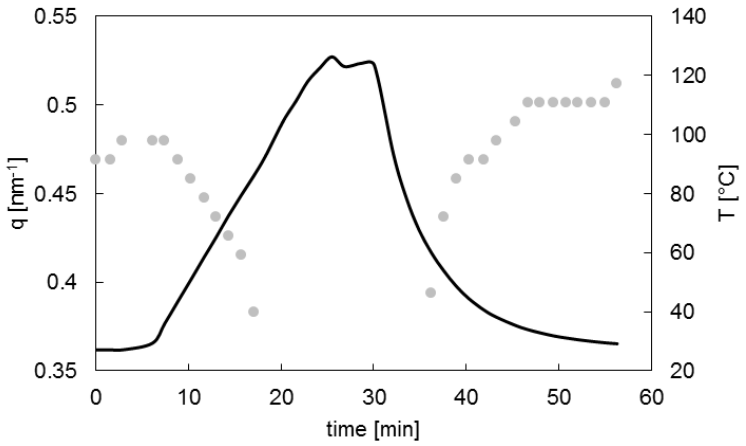

Figure 3.12: Time evolution of scattering vector peak position (•) and temperature (-) during SAXS experiment on EMAA-30Na.

3.3.3 Thermal analysis

DSC experiments clearly show the dual melting behaviour of the three EMAA based systems. All the polymers after aging exhibited two distinct melting peaks. The first melting peak in the EMAA based systems appeared between 40 °C and 60 °C, depending on the neutralization level. This endothermic flow can be associated to the thin crystallites. Increasing the temperature, a second melting event around 90 °C was also present for all polymers and it is related to primary crystal phase. Typical DSC thermograms (30 days aging) are presented in Figure 3.13; as comparisons, the single melting peak thermal behaviour of PE (polyethylene) is also shown. From these results it can be noticed that only the presence of MAA caused the two fundamental endothermic peaks, moreover, MAA produces a marked crystallinity reduction in the copolymers. In PE long ethylene chains can crystallize as larger lamellar crystals with fewer defects and therefore much higher melting temperature compared to EMAA copolymer and ionomers. In addition, some differences between the polymers can be recognised suggesting also an influence of the ionic clusters on the crystallization process, final crystals morphology and distribution. As first observation, the secondary melting peak shifts to higher temperature increasing the neutralization. Less evident is the influence of neutralization on the primary crystal phase leading to a different shape of the related melting peak; this behaviour could be attributed to a broad melting range of higher neutralized copolymers caused by the fringed-micellar or bundle-like crystals with a broad size distribution [129].

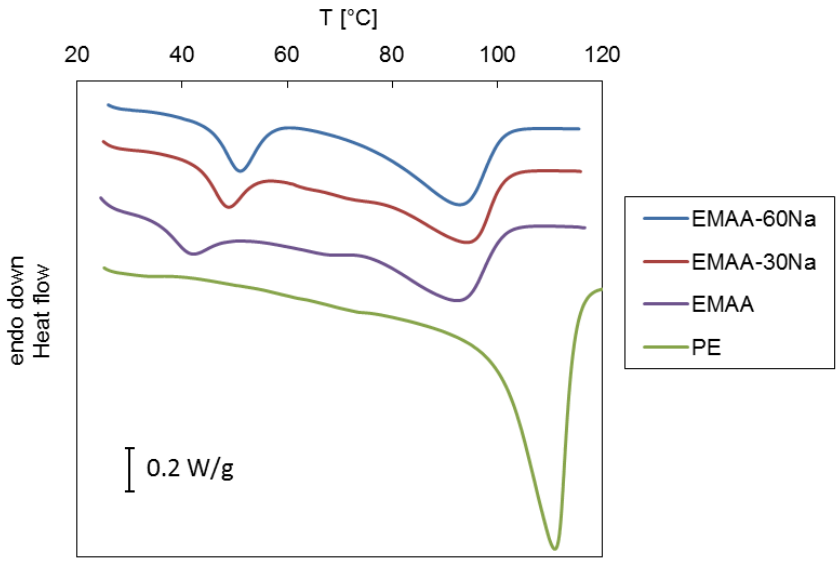

Figure 3.13: DSC thermograms of EMAA base polymers with different ions content and polyethylene.

In order to investigate the role of ionic content, DSC tests were also performed at different aging times; results are summarised in Table 3.6. An example of obtained thermograms of EMAA-30Na ionomer aged for 0, 1, 7 and 30 days are also presented in Figure 3.14. In these experiments for all EMAA based polymers, the lower melting peak shifts to higher temperature (Figure 3.15-a) and it changes in shape, becoming shaper and greater, increasing aging time; as reported in Figure 3.15-b an increment in the enthalpy with time related to this secondary crystal phase melting was measured. The same trend was also observed increasing neutralization level. These results might indicate a more homogenous crystallite lamellar thickness as the degree of neutralization or aging time increases [138]. On the other hand, the primary crystal phase seems to not be affected by aging time; more remarkable instead is the dependence on neutralization level producing an increment in enthalpy associated to this phase melting transition.

Comparing crystallinity, calculated respect the melting enthalpy of crystal polyethylene (293 J/g), emerged how the polymer with the highest neutralization level holds a large amount of ethylene crystallites that could affect the self-healing capability. As showed in the following paragraph, this feature has also an effect on mechanical properties.

Table 3.6: Thermal properties obtained by DSC experiments.

Polymer	Aging [days]	T_t [°C]	ΔH_t [J/g]	T_m [°C]	ΔH_m [J/g]	Crystallinity[a] [%]
EMAA	0	-	-	93.8±0.7	23.8±0.1	8.1
	1	39.3±0.7	2.7±0.1	93.7±0.6	24.0±0.4	9.1
	7	41.0±0.4	3.8±0.1	93.7±0.6	24.2±0.3	9.5
	30	41.1±0.3	4.9±0.3	93.3±0.3	24.7±0.8	10.1
EMAA-30Na	0	-	-	94.4±0.5	20.8±0.4	7.1
	1	44.7±0.1	4.2±0.1	94.3±0.5	21.8±0.7	8.9
	7	46.5±0.3	6.4±0.1	94.5±0.5	22.1±0.6	9.7
	30	48.2±0.2	7.2±0.3	94.5±0.5	22.2±0.3	10.0
EMAA-60Na	0	-	-	91.8±0.6	32.8±0.7	11.2
	1	46.8±03	7.1±0.4	91.8±0.7	33.8±1.6	14.0
	7	49.0±0.5	10.2±0.4	92.2±0.6	33.3±1.2	14.9
	30	51.0±0.1	11.8±0.5	92.6±0.6	33.1±0.7	15.3

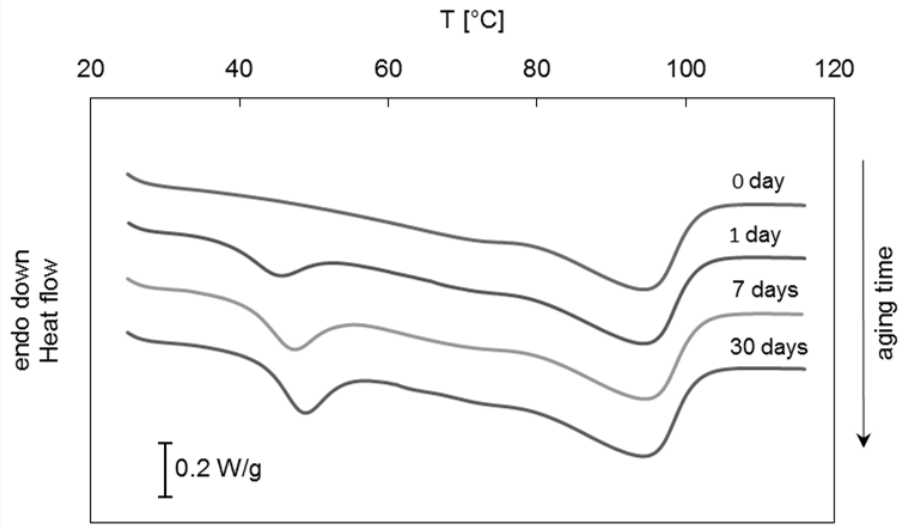

Figure 3.14: DSC curves of EMAA-30Na ionomer aged at different times.

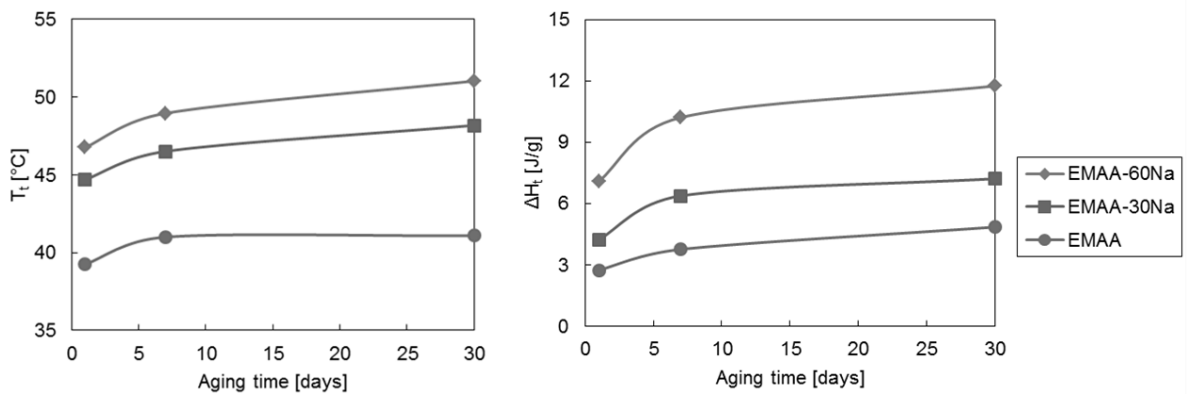

(a) (b)

Figure 3.15: Evolution of melting temperature (a) and enthalpy (b) over aging time.

3.3.4 Rheological tests

Healing phenomenon of studied systems after high-energy impact includes melting of the polymers and related deformation, recover and relaxation of material in the near of the impacts site. The elastomeric properties of the polymer melt allow to reach high strain level before failure even at high deformation rates. Moreover elastic rebound and chain mobility bring to a complete hole closure and sealing of the damage area, respectively. In this view, rheological measurements can provide valid information about the polymers behaviour in the molten state.

Steady shear viscosity of EMAA based copolymer and ionomers as function of shear rate measured at 150 °C is shown in Figure 3.16-a. All polymers exhibited a shear-thinning behaviour that becomes more evident as the degree of neutralization increases. Indeed, EMAA copolymer

showed a Newtonian plateau in a large shear rate range (0.001 - 10 s^{-1} at 150 °C). This behaviour is not detectable in the ionomers and probably the plateau shifts to even lower shear rate. Regarding viscosity value, EMAA-60Na show the highest viscosity followed by the polymer with the 30% of neutralized acid groups and the EMAA copolymer. Accordingly to these results, ionic content have also effect on the viscosity level, in particular, at low shear rate, it increased more than one order of magnitude in molten ionomers respect to the non-neutralized polymer.

Figure 3.16-b shows the steady shear viscosity of EMAA-30Na at various temperature; as expected, temperature increment produces a monotonically decrease of viscosity. EMAA and EMAA-60Na also exhibited a similar behaviour.

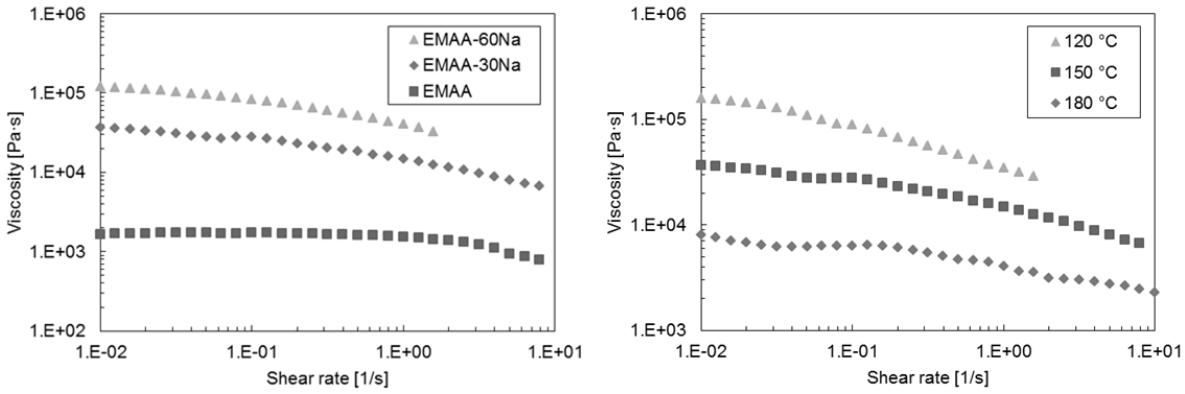

(a) (b)

Figure 3.16: Effect of Na neutralization on steady shear viscosity (T = 150 °C) (a) and temperature on EMAA-30Na ionomer (b).

Steady shear experiments provided a clear view on viscosity evolution at low shear rate. These results are useful to understand the overall effect of neutralization level on rheological properties of the polymer melt. However, no consideration can be done about the rheological properties of the different materials under high deformation rates. To obtain qualitative information about the behaviour of the materials under conditions more similar to those sustained during high energy impact additional dynamic rheological tests were carried out.

Dynamic tests performed at different temperature revealed, as also found in steady experiments, the shear thinning behaviour of the studied polymers (Figure 3.17). Moreover, employing the time-temperature superposition principle [147], it is possible to obtain master-curves of rheological properties by horizontally shifting the original data. The constructed master curves are valid for a specific reference temperature giving the opportunity to evaluate the response of the material in a wide frequency range. The proposed technique was successfully used to study the

rheological behaviour of various complex polymeric systems as hyperbranched polyesters [148] and also ionomers [149]. In addition, the resulting shift factors (a_t) as a function of temperature can be interpolated by the Arrhenius relation:

$$lna_t = \frac{E_a}{R(1/T - 1/T_0)} \tag{3.1}$$

where R is the universal gas constant, T_0 the reference temperature and E_a the flow activation energy. From the calculated E_a it seems that the higher degree of neutralization led to a greater flow activation energy suggesting stronger ionic interactions (Table 3.7). Moreover, the obtained results are comparable to those presented in other research activities studying similar ionomeric systems [149].

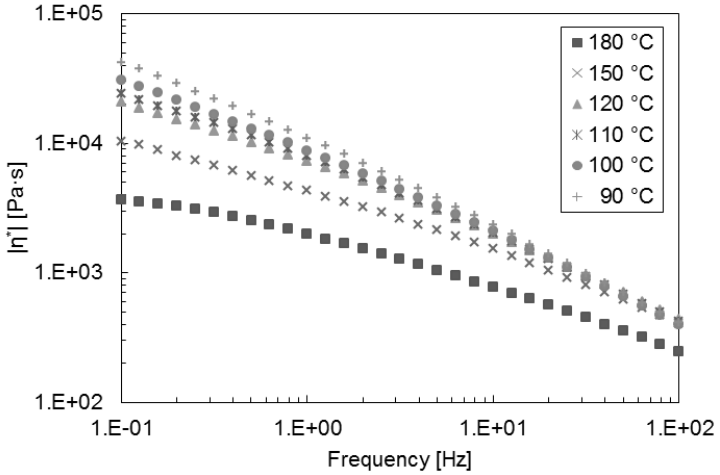

Figure 3.17: Evolution of complex viscosity with temperature for EMAA-30Na.

Table 3.7: Calculated flow activation energies.

Material	E_a [kJ/mol]
EMAA	64.65
EMAA-30Na	69.39
EMAA-60Na	76.59

Figure 3.18-a and 3.18-b show frequency-temperature master curves of complex viscosity (η^*) and storage modulus (G') at the reference temperature of 120 °C, respectively. EMAA-60Na complex viscosity exhibited the highest values in all the frequency range, however, the difference with the other polymers decreases with increasing the frequency. Similar considerations can be obtained by analysing G' master curves where EMAA-60Na showed the highest elastic behaviour in the melted state followed by EMAA-30Na ionomer and finally EMAA.

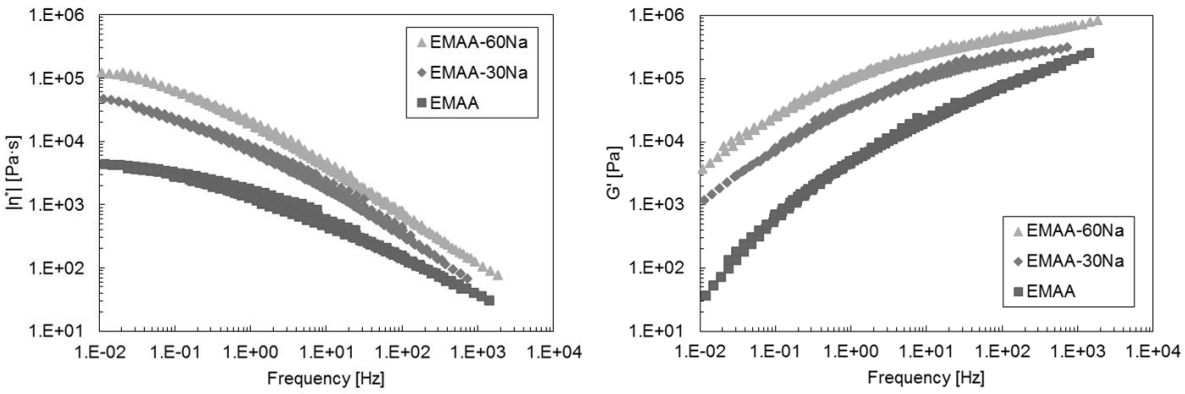

(a) (b)

Figure 3.18: Complex viscosity (a) and storage modulus (b) frequency-temperature master curves at 120 °C.

The resulting steady and dynamic rheological properties investigated with the different techniques can be combined together with the well-known Cox-Merx rule [150] to get steady shear viscosity (η) in a wider range of shear rates (Figure 3.19), thus, these new can be interpolated using an appropriate constitutive equation for polymer melts [151], the Cross model was selected [152]:

$$\frac{\eta - \eta_\infty}{\eta_0 - \eta_\infty} = \frac{1}{1 + (k\dot{\gamma})^n} \tag{3.2}$$

where η_0 is the zero shear-rate Newtonian viscosity, η_∞ is the infinite shear-rate viscosity, k is a time constant associated with the rupture of linkages and n is a power-law index. The fitting parameters for the three studied polymers are presented in Table 3.8; an example of obtained master curve for the EMAA copolymer is shown in Figure 3.19. These results confirm the different melt flow behaviour related to ions content at lower shear rates (highest zero shear-rate viscosity

for the EMAA-60Na ionomer), moreover, at the higher shear rate, all the polymers have similar viscosity values indicating a less ionic interaction due to the break of the physical crosslink.

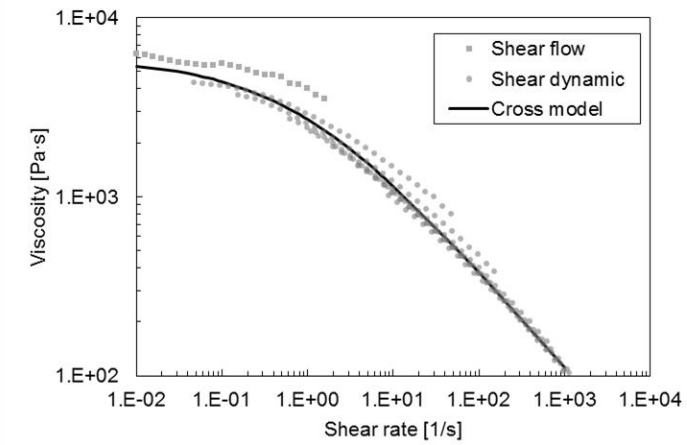

Figure 3.19: EMAA steady shear viscosity master curve at 120 °C obtained by Cox-Merz rule interpolated with the Cross model.

Table 3.8: Cross model fitting parameters.

Material	η_0 [Pa·s]	η_∞ [Pa·s]	k [s]	n [-]
EMAA	5835	$1.5 \cdot 10^{-6}$	1.314	0.549
EMAA-30Na	45180	$4.9 \cdot 10^{-6}$	1.524	0.704
EMAA-60Na	133600	$7.1 \cdot 10^{-6}$	1.639	0.755

This behaviour could be directly correlated to the self-healing characteristic of the polymers. The low flowing feature exhibited by the ionomer with the higher neutralization level produces the inability to repair at the lower projectile velocity. Conversely, at mid bullet speed, where more energy is transferred by the projectile during the impact, also EMAA-60Na ionomer showed an extended flow ability and thus, an efficient self-healing behaviour

3.3.5 Dynamic MTA

DMTA experiments, performed to investigate the effect of cations content, show a clear distinction between non-neutralised and neutralised polymers. Dynamical mechanical spectra were determined for all the different systems (Figure 3.20). EMAA based ionomers have similar elastic properties, on the other hand, the copolymer exhibits a lower storage modulus (G').

Furthermore, ionomers show an evident mechanical relaxation between 40 and 60 °C; in the EMAA instead, this transition occurs at lower temperature (20-40 °C). This relaxation, exhibited by all the three polymers, is caused by the melting of the secondary crystal phase already observed in the DSC tests.

Other secondary transitions between -40 and 0 °C, related to the glass transition of the amorphous phase, have also been investigated and identified in different research works [153].

DMTA experiments were also performed on sample with different aging time (not presented here) observing a slight decrease in the storage modulus around the detected transition temperature. Similar considerations have been derived also from dynamic tensile experiments.

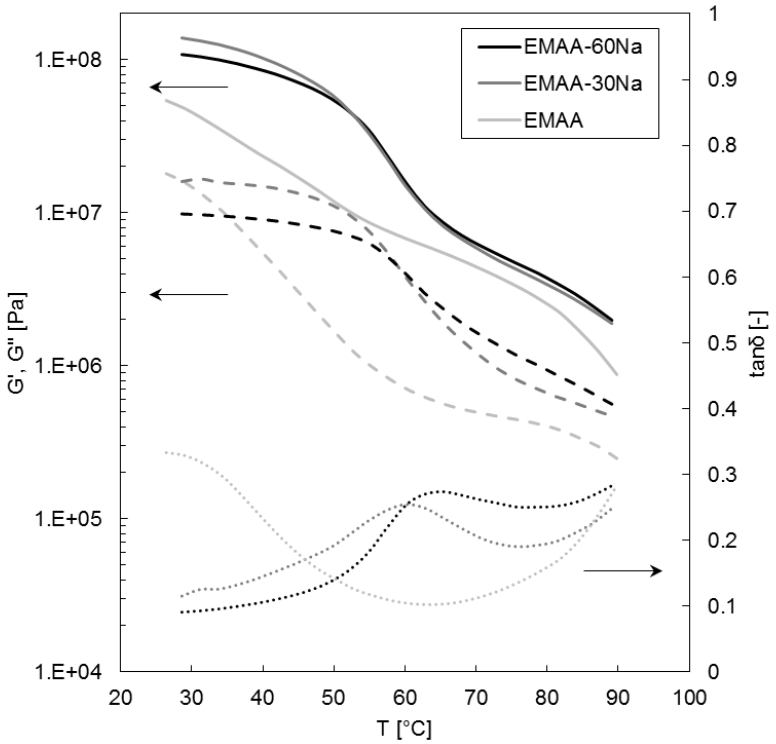

Figure 3.20: DMTA data obtained at 1 Hz and 10 °C/min, G'(—), G''(--) and tanδ (⋯).

3.3.6 Mechanical tests

Different quasi-static tests were performed in order to study the effect of neutralization level on mechanical properties. Tensile experiments performed at different temperature and strain rate revealed, as expected, a strong influence of such parameters; the same experimental framework adopted in Chapter 2 was employed and fully aged samples were tested. IR camera was also used

to measure temperature evolution during high strain rate tensile experiments and results, similar to those already presented in the previous chapter, were obtained.

Figure 3.21 reports an example of the behaviour of EMAA-60Na (a) and EMAA (b) tested at different temperatures and constant strain rate. The ionomer showed a higher stress level compared to the non-neutralised polymer, however this difference becomes less noticeable as the temperature decreases. For all polymers, EMAA, EMAA-60Na and EMAA30Na (refer also to Figure 2.4), both yield strength and ultimate strength increase with neutralization level and decreasing temperature, on the other end, strain at break decrease following the same criteria.

At greater temperature (from 60 °C to 23 °C), EMAA copolymer exhibited lower global mechanical properties than ionomers (yield stress and strain at break are respectively lower and higher). This trend can be observed up to 0 °C; around this temperature the non-neutralised polymer presented a stress level comparable to those shown by the ionomers, furthermore, a large strain at break reduction was also detected. This behaviour could be related to different mechanical characteristics and amount of the amorphous phase in the copolymer and ionomers as indicated by Wakabayashi et al. [153]; in these studies, researchers proposed to employ a two-phase model to quantify the effect of ionic neutralization on the amorphous phase modulus, in particular, Davies model was adopted.

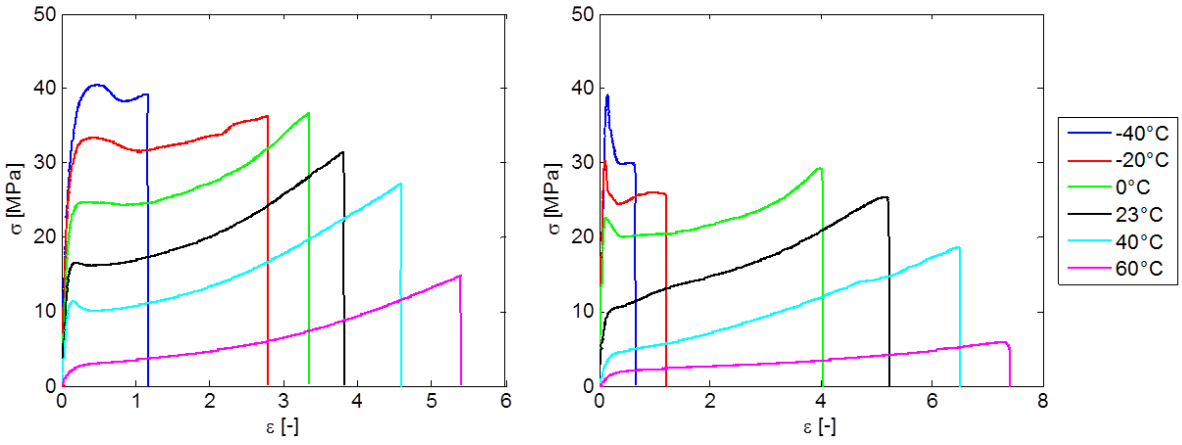

(a) (b)

Figure 3.21: Stress-strain curves of EMAA-60Na (a) and EMAA (b) tested at different temperature and constant strain rate (0.136 s^{-1}).

As in the previous chapter, following the approaches proposed by Scogna et al. [126,154] the yielding behaviour of the tested polymer was investigated adopting the Ree-Eyring model. Obtained curves and model fitting parameters are presented in Figure 3.22 and Table 3.9,

respectively. From the derived data an increase of the activation volume increasing the neutralization level was detected. On the other hand, activation energy seems that have a minimum for 30% acid group neutralization level, however the reason for this behaviour is unclear.

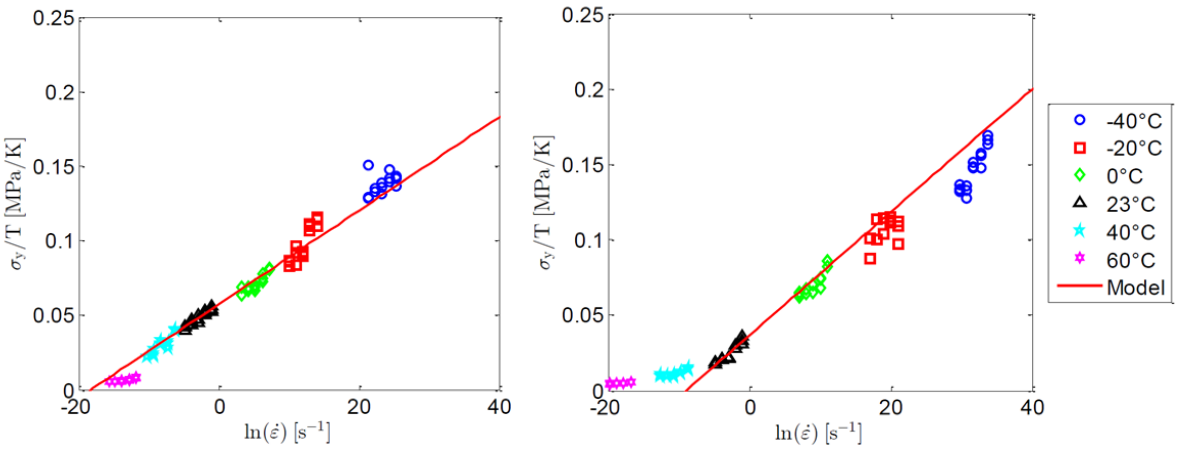

(a) (b)

Figure 3.22: Ree-Eyring fitting for EMAA-60Na (a) and EMAA (b).

Table 3.9: Ree-Eyring model fitting parameters.

Material	v **[nm^3]**	ΔH **[kJ/mol]**	$\dot{\varepsilon}_0$ **[s^{-1}]**
EMAA	4.10	350.54	$8.97 \cdot 10^{57}$
EMAA-30Na	5.0	190.16	$2.28 \cdot 10^{27}$
EMAA-60Na	5.30	239.25	$1.86 \cdot 10^{34}$

The effect of aging time, as already shown by XRD and DSC experimental activities, has an influence on microstructure morphology and thermal behaviour of the different polymers. In this view, tensile tests, performed at 0, 1, 7 and 30 days after samples production, were also carried out. Prior to being tested, all the specimens were stored in an environmental chamber under dry condition and room temperature. A constant rate of 1 mm/s was adopted for the tensile tests; indentation tests (not presented here) were also performed to evaluate the evolution of Young modulus with aging time catching basically the same results obtained with stretching experiments.

Figure 3.23 presents an example of the stress-strain curves obtained. For all the three studied EMAA based polymers. Both Young modulus and yield stress increase with time reaching a plateau after about 30 days aging (Figure 3.24). This behaviour is directly linked to the secondary phase reorganization and growth. Moreover, the highest mechanical properties are presented by the EMAA-30Na in opposition with compared to that observed in DSC experiments (higher crystal phase content for EMAA-60Na). These results indicate a critical limit of ion content on mechanical properties and may be related to the different yielding behaviour showed by the three polymers. Further analyses are required in order to clarify this aspect.

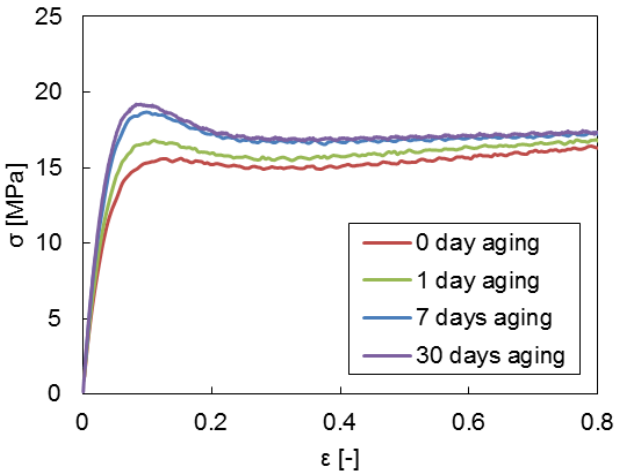

Figure 3.23: Effect of aging time on EMAA-30Na ionomer tested at 1 mm/s at room temperature.

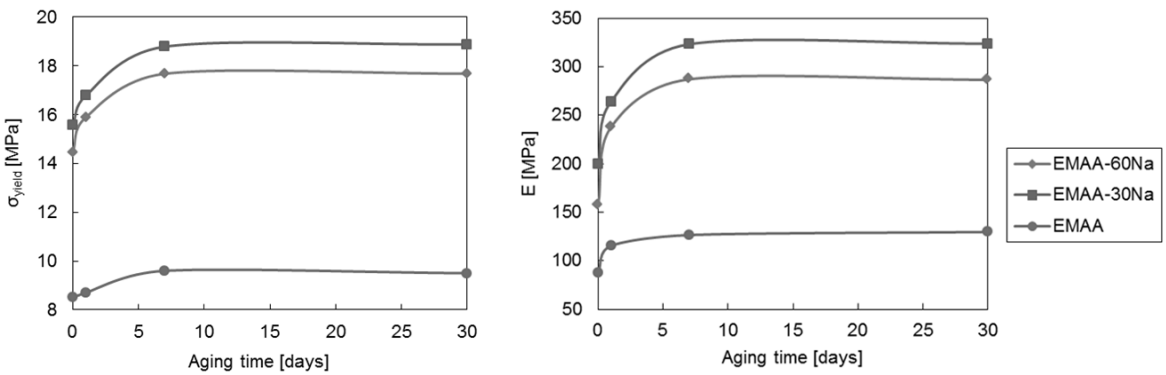

(a) (b)

Figure 3.24: Evolution of yield stress (a) and tensile modulus (b) with aging time.

3.4 Conclusions

The self-healing behaviour after ballistic puncture tests of EMAA based copolymer and Na ionomers were investigated under different experimental conditions. Impact tests were carried out firing spherical projectiles at different speeds ranging from 180 m/s, up to 400 m/s. At low velocity impact a clear self-healing behaviour was not detectable for the EMAA-60Na ionomer; the other tested polymers show instead an efficient self-repairing capability. Mid velocity impact tests revealed instead a similar self-healing feature for all studied polymers allowing to identify critical t/d ratios; however some difference between the tested polymers in the morphology of the impacted sites can still be recognised.

Moreover, performed physical tests showed how the balance between the different phases present in the studied polymers controls both thermo-rheological and mechanical properties, thus affecting the global self-healing behaviour of the polymeric systems.

Chapter 4 - Multilayer composites with self-healing capability based on an EMAA ionomer

4.1 Introduction

Ionomers based on EMAA are one of the first class of polymeric materials which have been found to exhibit an effective self-healing behaviour after high energy impacts. In view of an extension of the properties range required in different potential applications, self-healing blends based on ionomers with the addition of different crystalline, elastomeric polymers and modifiers have been prepared and investigated as presented in Chapter 5. However, the use of EMAA based polymers is currently limited to those events that pierce the material and despite this self-healing behaviour, these materials cannot be used in primary structural components due to their low mechanical properties.

A possible solution to this issue can be the use of EMAA ionomers in multilayer composite structures to improve mechanical performance providing also a self-healing behaviour. These types of structures are very common in many different fields because of their versatility.

Multilayer composite structures are widely used in aerospace industry for matching the best properties of different materials. In aeronautical components, sandwich structures are particularly used to increase the flexural stiffness and the ultimate buckling strength with a minimal increase of mass.

In space systems, multilayer structures are commonly used to achieve a “multifunctional material” given by the combination of the peculiar properties of each layer. For example, multilayer covering systems with thermal insulation and electromagnetic shielding layers have

been developed; for special missions some dedicated layers can be added to primary structures such as ablative heat shield or impact protection for planetary exploration missions.

In this chapter, the self-healing behaviour of various ionomer based multilayer composites was investigated under several ballistic impact conditions; in particular four different configuration of multilayer systems were prepared and tested:

- hybrid EMAA, EMAA-30Na or EMAA-60Na / aramid fabric multilayer composite (EMAA-0,30,60Na/AF);
- EMAA-30Na / carbon foam core sandwich composite (EMAA-30Na/CF);
- EMAA-30Na / carbon fibre reinforced polymer (CFRP) multilayer composite (EMAA-30Na/CFRP);
- EMAA-30Na / honeycomb core / CFRP sandwich composite (EMAA-30Na/H/CFRP).

The choice of reinforcing or core materials is based on the peculiar characteristics that each of the following materials has.

Aramid fabrics are widely used for flexible ballistic protections thanks to their tenacity and impact energy absorption capacity; aramid reinforced composite based find also extensive employment in rigid armour [155-158]. Different methodologies were developed to improve ballistic performance of these composite laminates; moreover, Carrillo et al. [159] studied aramid fabric/polypropylene multilayer systems demonstrating that both the ballistic limit and the perforation threshold energy increase for such systems compared to dry aramid fabrics with similar areal density. The improvement in the impact resistance can be explained by the ability of the thermoplastic matrix to maintain the orientation and position of the fibres during an impact event and to distribute the load caused by the impact among the fibres. Similar results were obtained by Lee et al. [160] investigating the ballistic properties of woven aramid fabrics impregnated with a fluid that exhibit the shear thickening effect.

Carbon foams present particular mechanical and thermal properties, which make them interesting in a number of structural applications. These foams, due to their low density, relatively easy machine tooling, stiffness and homogeneity could be employed in a sandwich panel as core or filling material [161]. Moreover, in spite of its brittle general behaviour, this kind of material due to its cellular structure and mechanical behaviour could have interesting ballistic properties by exploiting the compressive behaviour of the material. Subsequent impacts against cells walls as well as strain rate dependency of mechanical limits lead to high energy absorption as demonstrated by Janszen et al. [162-164]. In these studies they showed promising carbon foam ballistic performance after low velocity impacts (Figure 4.1). Under certain experimental condition

foams with different density were able to stop and in some cases hold a 5 mm diameter stainless steel sphere shot at a speed up to 240 m/s [164].

Figure 4.1: Low velocity impact on carbon foam sample [164].

Thanks to their excellent mechanical properties and low weight, CFRP are widely used in many applications, especially in the aerospace industry satisfying the growing request to produce light and efficient structures, with high standards of performance and safety. Honeycombs based sandwich structures are also often used in different engineering fields to improve the weight/strength ratio and absorb energy during impacts [165-167].

The main function of the honeycomb cores in a sandwich panel is to carry the normal and shear loads in the surfaces perpendicular to the axis of the hexagonal prisms (Figure 4.2). Honeycombs are particularly strong and stiff in this direction as compared with the two in-plane directions.

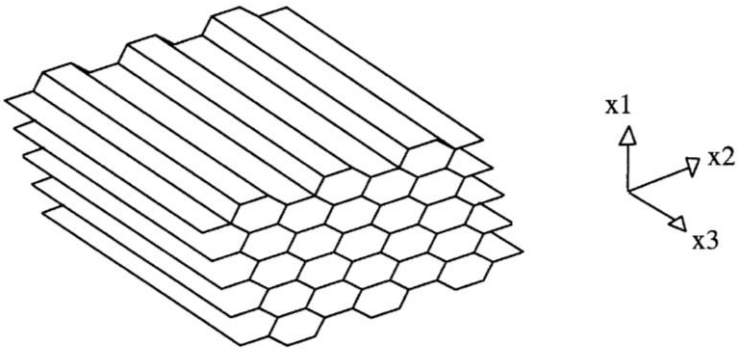

Figure 4.2: Honeycomb core.

A typical sandwich panel consists of two stiff skins (metal or fibre reinforced composite), separated by a lightweight honeycomb core. The separation of the skins by the core increases the moment of inertia of the panel with little increase in weight, producing an efficient structure for resisting bending and buckling loads.

The coupling of aramid fabrics, carbon foams CFRPs or honeycomb cores with polymers, as EMAA based ionomers, able to restore, at least partially, the continuity of the material may significantly extend the performances of such systems ensuring better reliability and response to impact effects.

Prepared multilayer systems were tested under different experimental conditions proving that self-healing behaviour of ionomeric layers can be maintained also in composites after low and high speed ballistic impact tests.

4.2 Experimental section

4.2.1 Materials

EMAA based ionomers are available on the market with Surlyn® trade name. Different grades are characterized by different amount of acid group, different cations used for neutralization (e,g Na, Zn, Mg, Li) and different neutralization level. As in the previous chapters, EMAA based ionomers with different level of sodium neutralization were used (0%, 30%, 60%).

Various materials were used as reinforcement or core, in particular aramid fabric, carbon foam, CFRP panel and honeycomb core.

Aramid fabric, STYLE 281 was provided by Seal SpA; Table 4.1 shows the general properties of the employed fabric.

Table 4.1: Aramid fabric properties.

	Threads x cm		**Linear density [dTex]**		**Th. [mm]**	**Weight [g/m^2]**			**Weave**
	warp	weft	warp	weft		warp	weft	total	
STYLE 281	6.7	6.7	1270	1270	0.25	86.5	86.5	173	plain

Carbon foam, FPA-35, supplied by GrafTech International, is characterized by a bulk density of 0.56 g/cm^3. Properties are summarized in Table 4.2.

Table 4.2: Carbon foam properties.

Bulk density [kg/m^3]	Modulus [GPa]	Compressive strength [MPa]	Porosity [%]
560	3.5	60	61

CFRP plates were produced using [0/+45/-45/0] stacking sequence of a pre-preg Satin 5H, 285 g/m^2, fabric obtaining a final thickness of about 1 mm. Cure cycle in autoclave was employed.
The physical and mechanical properties of the honeycomb are strongly dependent on the characteristics of the manufacturing material, the density and the geometry of the cell. In this research, honeycomb core, supplied by Hexcel®, was the Hexweb® A1-48-3. General geometrical and mechanical properties provided by the supplier are presented in Table 4.3.

Table 4.3: Honeycomb properties.

Material	Cell size [mm]	Density [kg/m^3]	Thickness [mm]	Strength* [MPa]	Modulus* [MPa]
Nomex®	3.2	48	6.35	2.40	138

*Stabilised compression

4.2.2 Multilayer composites manufacturing

Ionomeric plates of 120x120 mm with thickness of 0.5, 1, 2 and 3 mm were produced by compression moulding using a hot platens hydraulic press following the same procedure and conditions adopted in Chapter 2. Multilayer hybrid composites were produced using a similar technique; in the specific, previously produced 1 mm thick polymeric plates were used as outer layers in the stacking sequence (Figure 4.3). All layers, ionomeric plates, aramid fabric, carbon foam or CFRP were positioned within the mould and then lightly pressed for 10 minutes at 120 °C in order to allow the adhesion between the different “plies”.
In case of aramid reinforcement, up to 5 fabric layers were employed and partial impregnation was obtained. Plates with a thickness of 1 mm of the three different polymers (EMAA, EMAA-30Na and EMAA-60Na) previously studied in Chapter 3 were used as outer layers.

Regarding, carbon foam slices of 10 mm thickness were instead employed for the production of EMAA-30Na/CF multilayer composites. In order to allow adhesion between the layers, carbon foam slices were preheated in oven at 120 °C and then stacked up in the mould with 1 mm EMAA-30Na ionomeric plates.

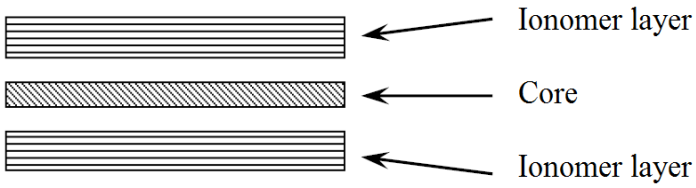

Figure 4.3: Representation of the different multilayer composites.

EMAA-30/CFRP multilayer systems were produced with a similar procedure coupling and pressing 1 mm CFRP and EMAA-30Na plates in the mould at 120 °C (Figure 4.4-a).

EMAA-30Na /H/CFRP sandwich composites were produced in a different way. The different layers bonded with an acrylic adhesive (Figure 4.4-b). Also in this case 1 mm CFRP and EMAA-30Na plates were employed.

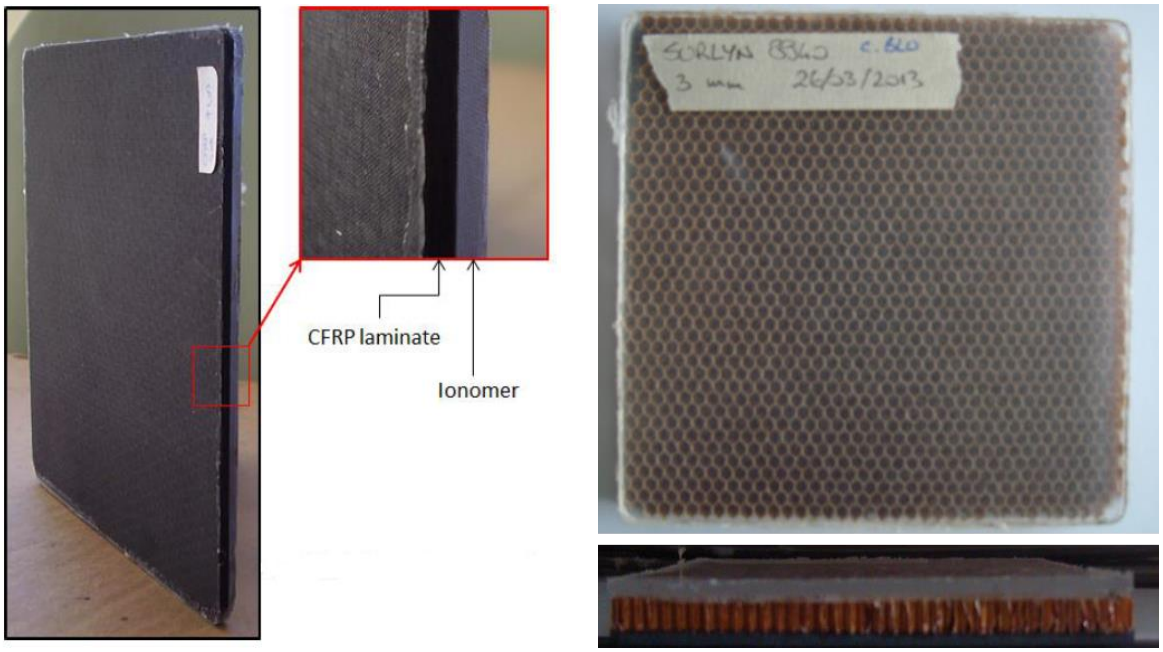

(a) (b)

Figure 4.4: Produced EMAA-30Na/CFRP (a) and EMAA-30Na/H/CFRP (b) multilayer systems.

After productions, all samples were stored in temperature and humidity controlled chamber (25 °C/ 50% RH) prior to testing.

The choice to use EMAA-30Na for the production of the majority of the multilayer systems was made to maximize the repairing effect minimizing the number of samples to be tested since this polymer exhibited better self-healing behaviour in a large projectile velocity range as shown in Chapter 3.

4.2.3 Ballistic tests and healing evaluation

Ballistic puncture tests on multilayer plates were performed in a ballistic laboratory by shooting with a fire gun, model Thompson G2 Contender, 5.65x20 mm pointed bullets through 120x120 mm square samples. The speed of bullets during ballistic tests was measured using an optical chronograph (model CED M2 Millennium) and it ranged between 700 and 730 m/s. All tests were performed at about 23 °C. An example of EMAA-30Na/AF tested multilayer composites is presented in Figure 4.5. Impact test on dry aramid fabrics were also carried out for comparison purpose.

Preliminary test were also performed on standalone polymeric plates (EMAA, EMAA-30Na and EMAA-60Na) with thickness ranging from 0.5 to 3 mm in order to confirm the self-healing capabilities under these test conditions.

Impact tests on EMAA-30Na/H/CFRP multilayer systems were instead performed firing spherical projectiles at low velocity (180 m/s) adopting the experimental procedure presented in Chapter 2.

A scheme of performed impact tests is presented in Table 4.4.

Healing evaluation for all tested samples was performed both with image analysis (optical and SEM) and pressure tests.

Table 4.4: Impact tests performed on multilayer systems and standalone polymeric plates.

System ID	Velocity [m/s]	Bullet shape	Bullet diameter [mm]
EMAA-(0,30,60)Na	700	pointed	5.65
EMAA-(0,30,60)Na/AF	700	pointed	5.65
EMAA-30Na/CF	700	pointed	5.65
EMAA-30Na/CFRP	700	pointed	5.65
EMAA-30Na/H/CFRP	180	spherical	from 2.35 to 14.27*

* same testing conditions adopted in Chapter 2

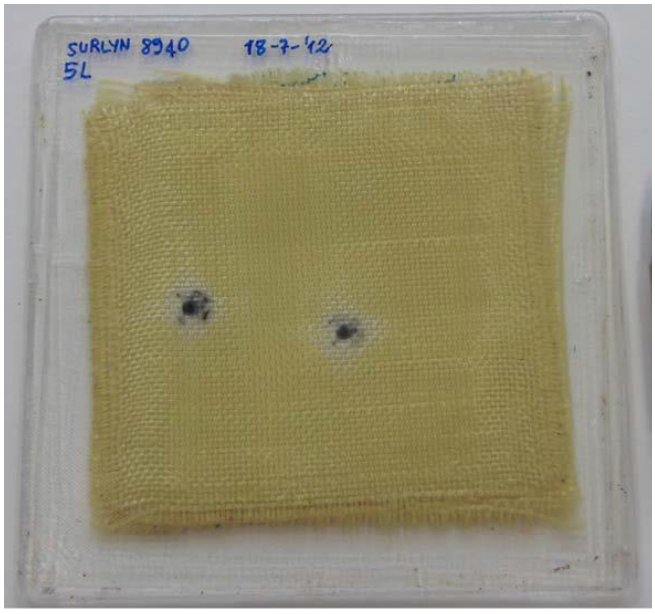

Figure 4.5: EMAA-30Na /AF multilayer composite after high velocity impact test.

4.3 Results and discussion

4.3.1 EMAA copolymer and EMAA-Na ionomers

Experimental activities presented in the previous chapters showed how EMAA based polymer and ionomers exhibit an effective self-healing behaviour after ballistic impact tests under different experimental conditions. In order to further explore this self-healing capability, preliminary impact tests on standalone polymeric plates were performed with 5.65 mm diameter bullets fired at 700 m/s; also in these case the self-healing behaviour was well maintained for all the three studied polymers. Only the 0.5 mm thickness samples did not show a complete hole closure and sealing.

Microscope observations of healed polymeric samples after ballistic tests evidenced a complete hole closure and a clear melted zone in the centre of the crater (Figure 4.6-a); the great energy exchanged during the puncture due to impact, friction forces and deformation causes a local heating above the melting temperature of the polymer, promoting the hole sealing. Damaged area shows also the characteristic striations radially distributed around the crater caused by an intense plastic deformation during projectile passage through the sample.

Observing the back side (Figure 4.6-b), brittle radial cracks appeared in all cases probably indicating a petaling of the material during impacts. However, it is clearly observable a portion of the molten material at the centre of the damaged zone.

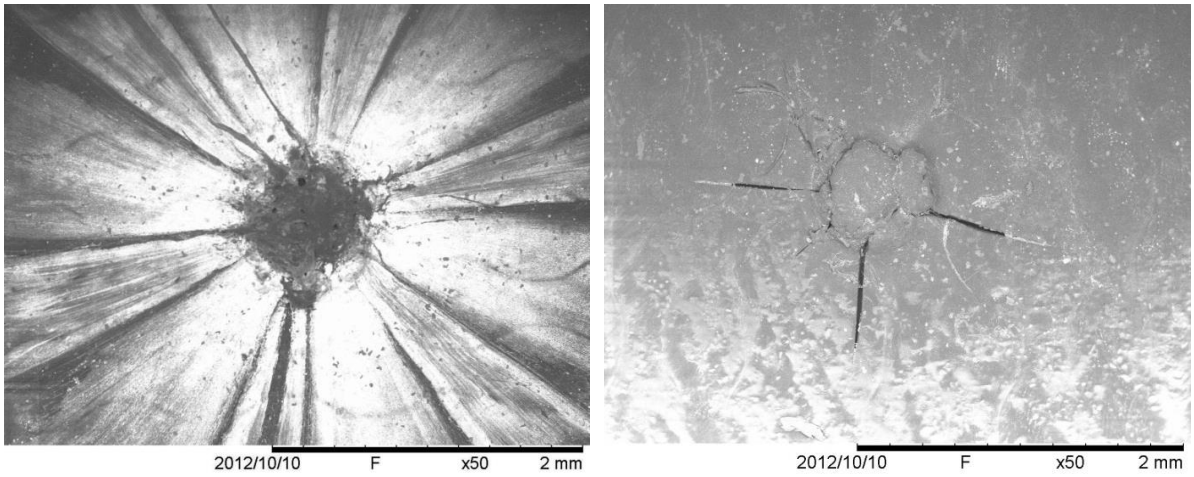

(a) (b)

Figure 4.6: Damaged area front side (a) and back side (b) micrographs of 2 mm EMAA-30Na sample after impact.

These results are in agreement with the two stage healing mechanism proposed for ionomers, where, viscoelastic recovery is supposed to bring to hole closure in the first stage, while, local melting process leads to full or partial hole sealing in the second healing stage [70].

4.3.2 Aramid fabric based multilayer systems

The tested multilayer composites exhibit different responses after ballistic impacts, however some common similarities with the previous case for those with aramid fabrics can still be recognized.

From Figure 4.7-a and Figure 4.8-a, it can be noted that for all tested samples, having a different number of fabric plies, hole closure occurred; however, leakage tests revealed that only samples with 1 and 2 fabric layers with EMAA-30Na and EMAA-60Na show a complete and efficient self-healing behaviour; results are summarised in Table 4.5.

Table 4.5: Impact test results on aramid fabric based multilayer systems.

Material / No. layers	1	2	3	4	5
EMAA-60Na	✓	✓/✗	✗	✗	✗
EMAA-30Na	✓	✓	✗	✗	✗
EMAA	✗	-	-	-	-

Comparing tests on multilayer plates with the ones on dry fabrics it can be derived that the reduced constrain exerted by the fabric in the impact area, allows, for all polymers, viscoelastic recovery; the texture of the fabric is restored after the passage of the projectile in the multilayer systems (Figure 4.7).

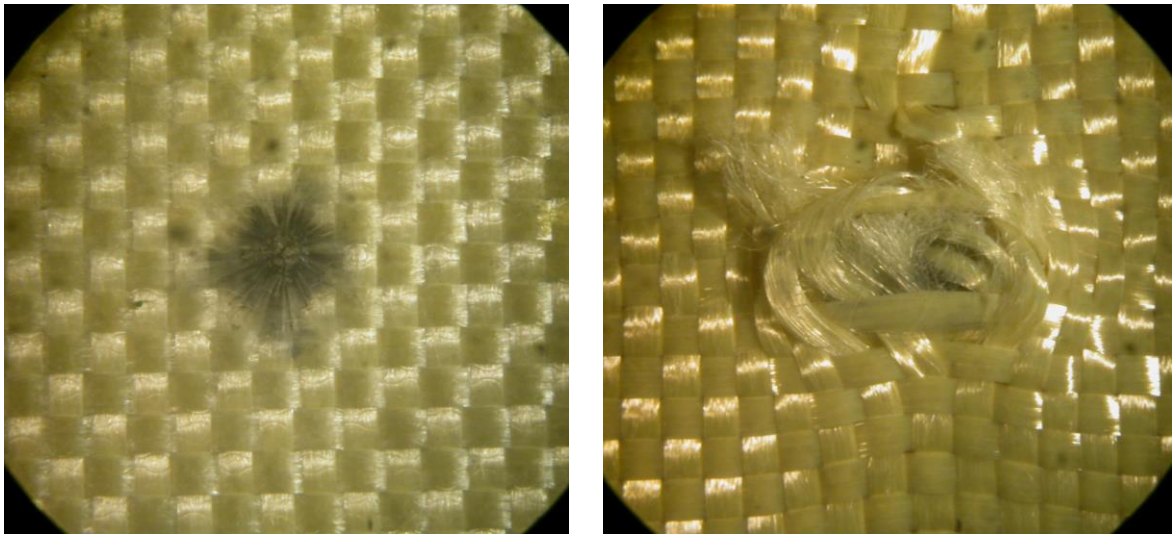

(a) (b)

Figure 4.7: Optical image of EMAA-30Na/AF (4 layers) composite (a) and dry aramid fabric after impact tests.

The morphology of the damaged area in all healed and no-healed samples presented striations with a melted zone at the impact site, as shown in Figure 4.8-a. In healed samples, this region is wide enough to allow the complete sealing of the hole.

Also in this case, observing the back side of tested samples, brittle radial cracks appeared (Figure 4.8-b); moreover in the projectile exit side a clear melted zone is not detectable as in the previous case (Figure 4.6-b) and aramid fibres are present within the cracks.

This behaviour suggests that the additional contribution to temperature increment deriving from the friction forces between bullet and impact surface was dissipated in the exit side as consequence of the presence of aramid fabrics, preventing the hole sealing in that zone.

4.3.3 EMAA-30Na/carbon foam multilayer systems

Ballistic experiments carried out on a sandwich made of EMAA-30Na plates with carbon foam core, revealed behaviour similar to the previous case. The self-repairing phenomenon of the ionomeric layers partially appeared only in the first polymeric layer hit by the bullet (inlet layer).

When the bullet passed through carbon foam, the outlet ionomeric layer did not exhibit the same self-healing ability, as revealed by leakage tests. It is conceivable that the bullet passage through the first polymer plate and carbon core reduces its energy so that no re-welding and healing of the ionomer is possible in the outer layer. Another possible cause of no healing of the outer ionomer layer could be attributed to the cloud of carbon microparticles generated during the impact of the projectile with the foam; these particles, deposited on the damaged area, may prevent the repair process. However, also in this case, at least partial hole closure was observed for all tested samples (Figure 4.9).

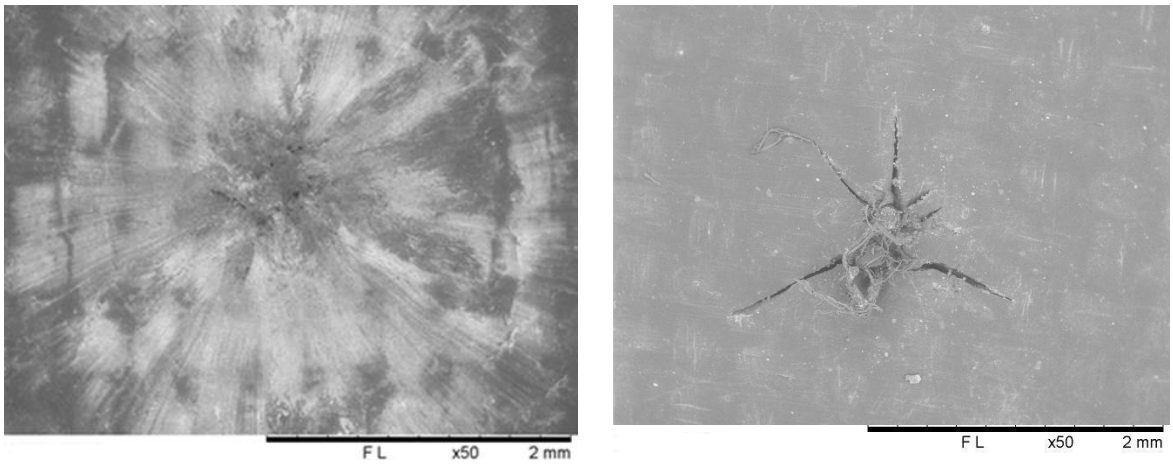

(a) (b)

Figure 4.8: SEM micrographs of EMAA-30Na/AF (1 layer) composite bullet entry side (a) and exit side (b).

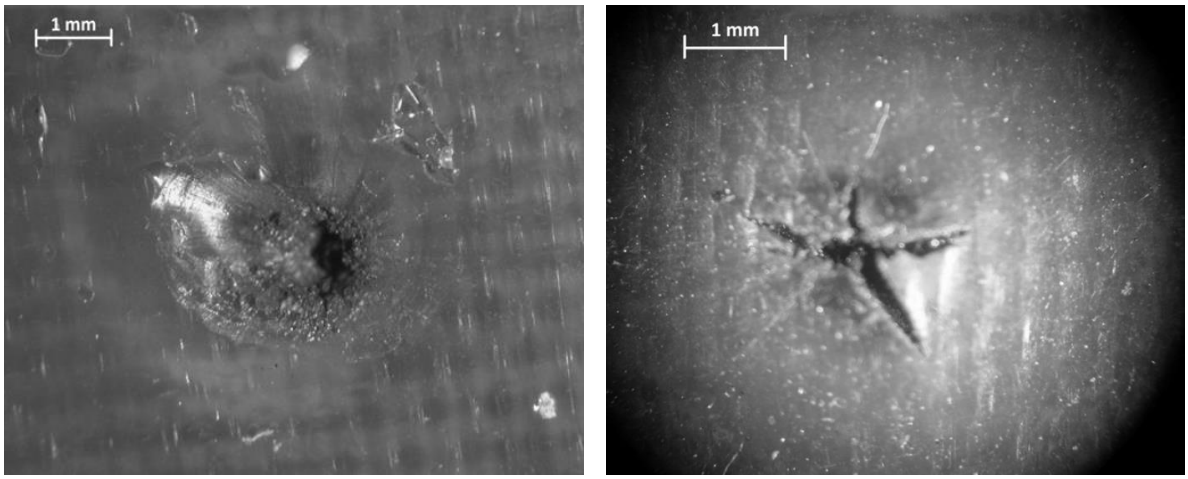

(a) (b)

Figure 4.9: EMAA-30Na/CF multilayer composite impacted area.

4.3.4 EMAA-30Na/CFRP multilayer systems

Results of ballistic tests on EMAA-30Na/CFRP multilayer system showed a completely different response from the previous cases. Tests were performed both CFRP and EMAA-30Na bullet entry side; no substantial differences were found.

Although the self-healing behaviour of the EMAA-30Na layer was not complete, however a remarkable hole reduction took place even under these testing conditions (Figure 4.10). CFRP layers instead present a clear circular hole of about the same diameter of the used projectile. After ballistic tests it can be also observed an extensive delaminated zone around impact sites (Figure 4.11).

The presence of a rigid layer, such as the CFRP one, prevents deformation of the ionomer ply. This behaviour has effects on the self-repair capability, which requires the melting of the polymer in the area of impact. Heat generated by plastic deformation and friction forces consistently give a fundamental contribution to the recovering and sealing of the hole and it seem that limited deformation cause the limitation of such phenomena, thereby preventing an efficient hole closure and repair.

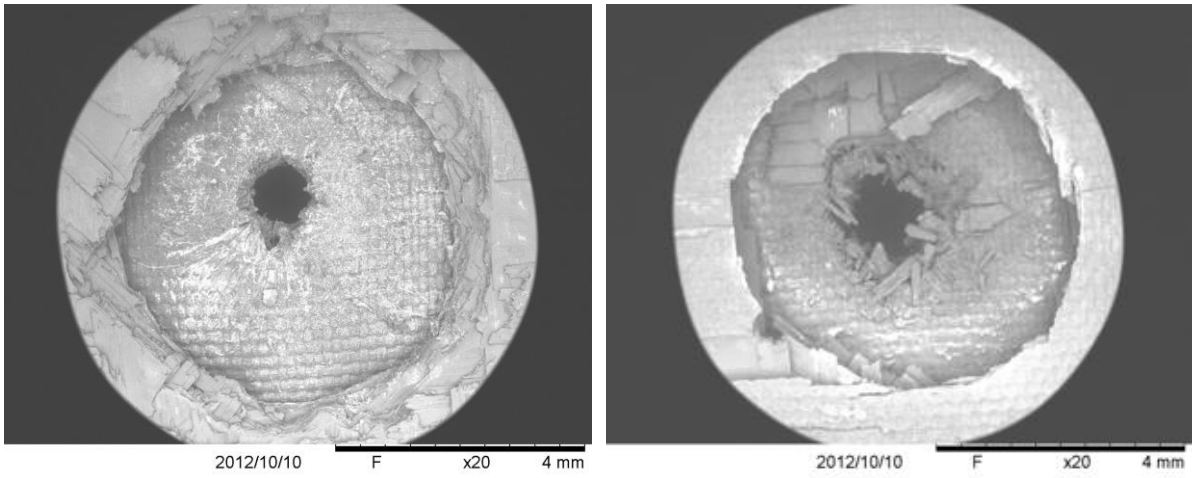

(a) (b)

Figure 4.10: EMAA-30Na/CFRP composite bullet entry side ionomer (a), entry side CFRP (b).

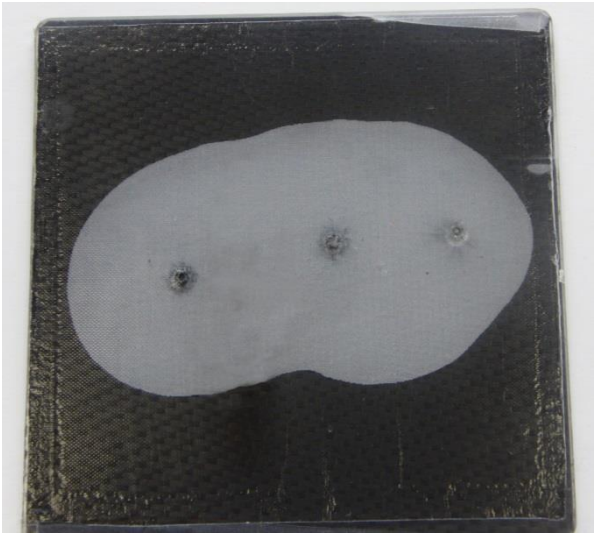

Figure 4.11: Delamination between ionomer layer and CFRP plate.

4.3.5 EMAA-30Na/Honeycomb/CFRP multilayer systems

Previous results, obtained on the different multilayer systems, underline the need of the ionimeric to deform in order to exhibit the self-healing ability. A possible solution to allow the deformation is to introduce after the self-healing polymer a lightweight compliant layer as the honeycomb. Moreover, a CFRP layer bonded as a skin on the other side of the honeycomb core can provide the required stiffness and strength in aerospace structures.

Impact tests performed at low velocity (180 m/s) firing spherical projectiles on sandwich panels with EMAA-30Na layers of 1, 2, and 3 mm revealed that the self-healing ability is maintained also for this sample configuration. Furthermore, a comparison between impacted stand-alone ionemeric plates (Table 2.2) and ionomer layers in an EMAA-Na/H/CFRP (Table 4.6) shows that similar t/d ratio is required for the self-healing event.

Table 4.6: Results of impact test on sandwich systems; t = EMAA-30Na layer thickness, d = sphere diameter.

		Sphere diameter [mm]							
	t/d [-]	**2.35**	**3**	**5**	**6.34**	**8**	**10**	**12**	**14.27**
Thickness [mm]	**1.0**	0.43	0.33	0.20	0.16	0.13	0.10	0.08	0.07
	2.0	0.85	0.67	0.40	0.32	0.25	0.20	0.17	0.14
	3.0	1.28	1.00	0.60	0.47	0.38	0.30	0.25	0.21

Observing the impacted areas (Figure 4.12-a), the morphology of the damaged zones exhibits the same characteristics features previous detected in stand-alone EMAA-30Na samples (Figure 4.12-b), including melted zone in the centre and petaling.

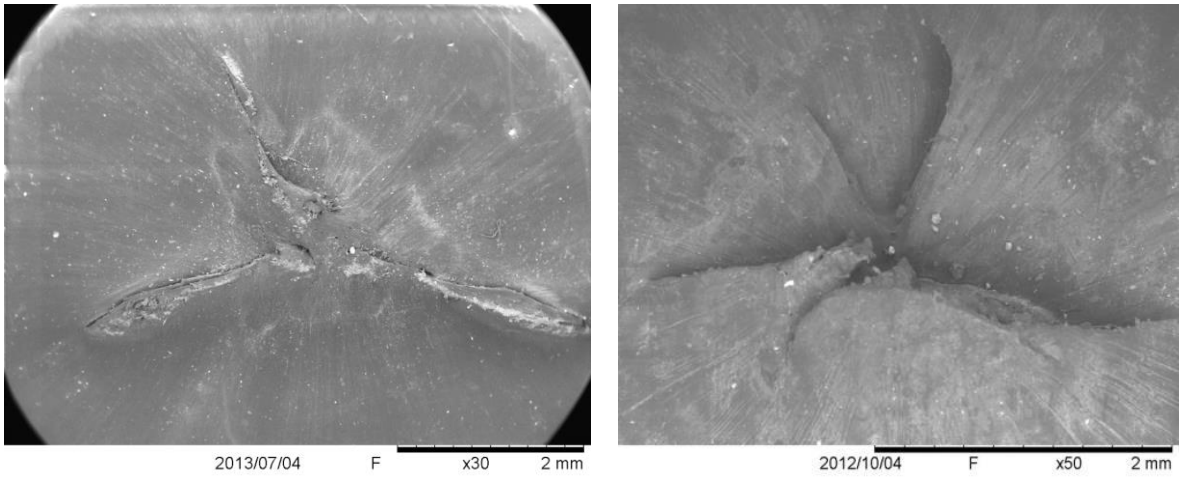

(a) (b)

Figure 4.12: Damaged areas of EMAA-Na layer in sandwich composite (a) and stand-alone ionomer plate (b).

In addition, bulletproof capability of the developed multilayer systems was investigated. In highest energy impacts (sphere diameter greater than 8 mm), projectiles pass through the specimens, perforating also the CFRP layer. Conversely, in the lowest energy impacts, spherical projectiles remain embedded in the honeycomb core, as reported in Figure 4.14-a; however substantial damages are detectable in the CFRP layers (Figure 4.14-b).

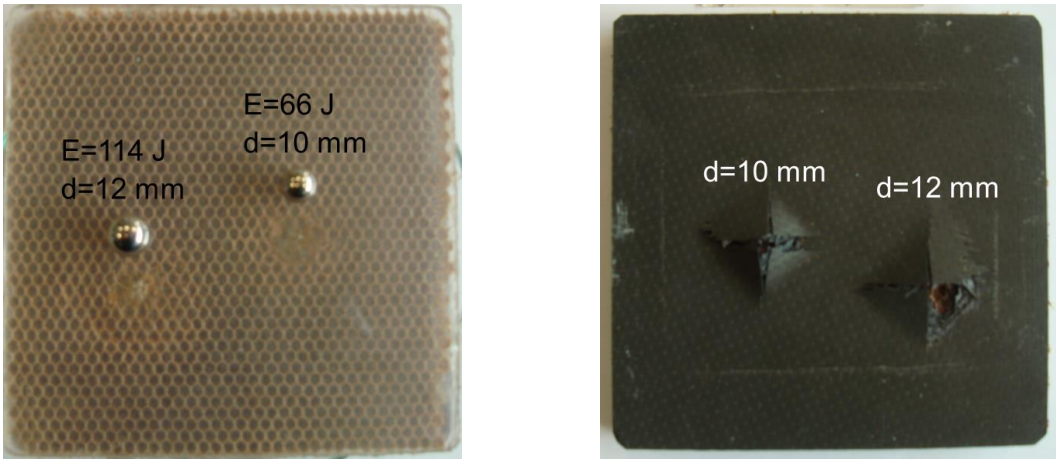

(a) (b)

Figure 4.13: High energy impacts on sandwich systems.

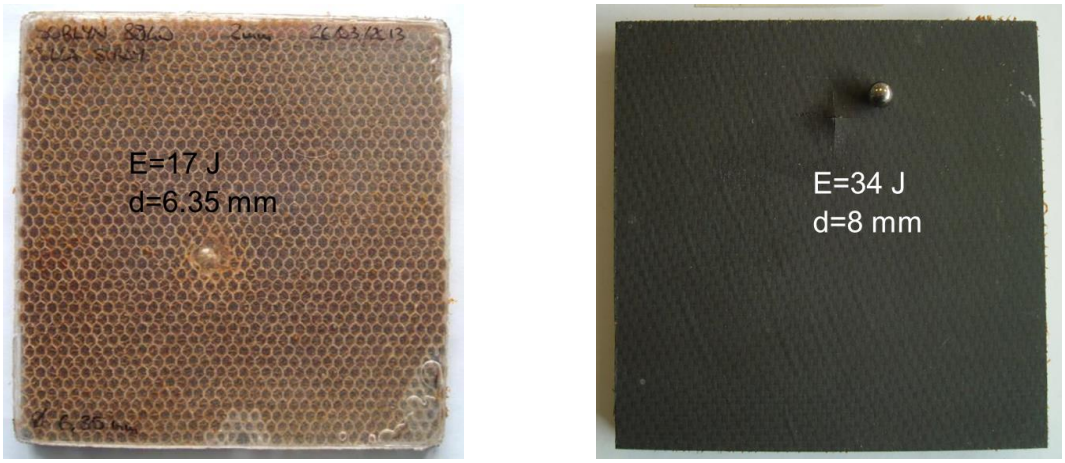

(a) (b)

Figure 4.14: Low energy impacts on sandwich systems.

4.4 Conclusions

In this chapter, the self-healing behaviour of different ionomeric multilayer systems was explored. Performed ballistic impact tests on multilayer plates showed how this capability was in some instance well maintained in the ionomer layers.

Similar response after ballistic impact has been shown by EMAA-(0,30,60)Na/AF and EMAA-30Na/carbon foam multilayer systems.

Hybrid multilayer composites with a carbon-epoxy ply instead, did not exhibit a complete hole closure preventing the self-sealing of the damage after impact. However, a remarkable hole reduction was observed even under these testing conditions.

On the other end, EMAA-30Na layers introduced as skin in honeycomb core sandwich systems show a self-healing behaviour in agreement with that reported for stand-alone EMAA-30Na plates.

A further study may involve the response of these kinds of structures under hypervelocity impact tests in view of possible space applications. These results encourage the study of ionomeric systems and the development of new complex structures yet able to maintain an efficient self-healing ability suggesting also a number of other potential applications in environments prone to impact damages.

Chapter 5 - Ionomer blends

5.1 Introduction

The development of new self-healing materials is an important issue either from a scientific or a technological point of you. Concerning, ionomers, the self-healing behaviour after ballistic impacts appears usually within a limited range of ambient conditions, impact speeds, object geometries [70-75]. A common way to extend the range of properties of polymeric materials is blending with other different polymers and the availability of tailored materials with controlled properties can greatly extend possible operating situations and applications.

Polymer blends having one component as ionomer can develop interesting combinations of thermal and mechanical properties. There exists an extensive literature concerning the synthesis, morphology, and properties of ionomer based blends, however, few trials are reported in literature about polymeric blends containing ionomers and self-healing capability. Varley et al. [72] presented a study on the self-healing behaviour of blends EMAA ionomers with low-molecular-weight acid monomers. Moreover Vega et al. [168] investigated the scratch healing of several ionomers and ionomer based blends.

In this chapter the self-healing ability after high-energy impact of polymer blends based on EMAA-30Na ionomer containing two different polymers is presented. A semi-crystalline poly(vinyl alcohol-co-ethylene) polymer (EVOH) or an epoxidized natural rubber (ENR50) were chosen as component for the blends. The addition of a second component to an ionomer base can deeply change the physical and mechanical properties, thus providing materials with selectable performances over a wide property range.

Indeed, the aim was to investigate the effect of introducing more crystalline segments or highly mobile macromolecular segments in the ionomeric systems over their self-healing behaviour.

In particular, binary blends of different compositions (15-50% of EVOH or ENR50) based on EMAA-30Na were studied by ballistic puncture tests and characterised with physical and mechanical tests. The blends were prepared by melt-mixing and were compression moulded to produce plates of different thickness. Pointed bullets were shot at 700 m/s into the prepared flat specimens; subsequently, the healing efficiency of each sample was observed by microscope analysis and it was further checked by de-pressurized airflow tests. EMAA-30Na showed complete self-healing behaviour in these testing conditions, as expected. Regarding blends, all the samples show at least partial reduction of the punctured surface but, interestingly, all EMAA-30Na/ENR50 blends exhibited complete healing. Also EMAA-30Na/EVOH blends up to 30% EVOH showed an efficient self-healing behaviour and only in blends containing 50% EVOH full repair was not observed.

Several tests were carried out to determine the physical and mechanical propertis of the blends. These tests showed that the blending process gives the opportunity to develop interesting combinations of properties without significant loss in the self-healing behaviour.

Regarding mechanical behaviour, it should be noted that the two polymeric components introduced different mechanical effects, i.e., with increasing stiffness, in case of adding EVOH, and reducing it in case of ENR50. In addition to this, the presence of ethylene units in EVOH can promote a good degree of compatibility between the two components and vinyl alcohol units may interact with functional acid groups by modifying the ionic clusters. On the other hand, amorphous ENR50 introduced more rubbery domains; moreover, epoxy groups in ENR50 may also interact with the ionic clusters in dispersed in the ionomer, thus modifying the ionic strength as well as the viscoelastic behaviour. In order to correlate blend thermo-mechanical and viscoelastic properties with the self-healing behaviour, DMTA and DSC experiments were also performed and discussed.

The development of materials with varying physical and mechanical properties may add important information to the analysis of healing mechanisms. Since processing conditions affect the compatibility of components, a relationship between blend morphology and healing efficiency could be also investigated, in view of possible development of blends with controlled structure and improved self-healing capacity.

5.2 Experimental section

5.2.1 Materials

The sodium neutralised EMAA-30Na ionomer was selected as base material for blends production; the main characteristics of the polymer are shown in the previous chapters (Chapter 2 and Chapter 3).

A thermoplastic polymer (EVOH) was chosen as hard phase for blends manufacturing and it was purchased from Sigma-Aldrich. This polymer has a density of 1.14 g/cm^3 at 25 °C and it is characterised by an ethylene content of 44 mol%, moreover, melt flow index at 210 C° is 3.5 g/10 min. All the data were provided by the supplier.

The ENR50 rubber was purchased from San-Thap International Co. Ltd. (Thailand). This elastomer is based on natural rubber (cis-1,4 polyisoprene) with, in addition, epoxidised groups randomly distributed along the polymer backbone (50% epoxidation level). General properties reported by the producer are summarised in Table 5.1 DCP, used as a cross-linking agent for ENR50, was purchased from Sigma-Aldrich.

Table 5.1: ENR50 properties.

Properties	ENR50
Glass transition [°C]	-24
Density [g/cm^3]	1.02
Mooney viscosity [-]	70-90

5.2.2 Blend processing

Different compositions of EMAA-30Na/EVOH and EMAA-30Na/ENR50 were blended in a twin-screw Barbender (Plastograph, Germany). The first set of blends were melt mixed at 200 °C with a specific screw speed-profile reaching a final constant rotational speed of 80 rpm. Blends with EVOH weight content range from 15% to 50% were prepared. EMAA-30Na/ENR50 blends were melt-blended in the same discontinuous mixer setting a temperature of 120 °C. The same mixing procedure and blend compositions were used. Furthermore, ENR50 based blends with different DCP cross-linker amounts (0.2 and 0.5 wt%) were prepared.

After mixing, samples of 2±0.1 mm thickness were compression moulded by using a hot press set to 180 °C for EVOH based blends and to 150 °C for EMAA-30Na/ENR50 blends. During cooling stage the pressure was maintained until to the removal of the sample from the mould.
All polymers were dried in a vacuum chamber for 12 hours before production.
It is worth to notice that blends with EVOH were opaque, while blends with ENR50 maintained transparency at all compositions as the pure ionomer; this behaviour suggest a higher crystallization level in the EMAA-30Na/EVOH blends.

5.2.3 Measurements

The self-healing capability of produced polymeric blends was investigated by ballistic puncture tests. These experiments were performed at Fiocchi Munizioni Ballistic Lab. by shooting pointed bullets with a nominal diameter of 4.64 mm (Figure 5.1) through 100x100x2 mm square plates. Measured projectile speeds and test temperatures were in all case in the 715±15 m/s velocity range and 23±0.5 °C temperature range, respectively. Subsequently healing evaluation was performed observing all specimens by optical stereo-microscope and by SEM both in the bullet entrance and exit side. Moreover, to check for the healing efficiency, a pressure difference of 0.8 bar was applied in the puncture zone by a vacuum pump using the testing device presented in Chapter 2. Hole closure was tested both by following vacuum decay and by checking for possible flow of a fluid droplet placed at the damage zone with the applied pressure difference.

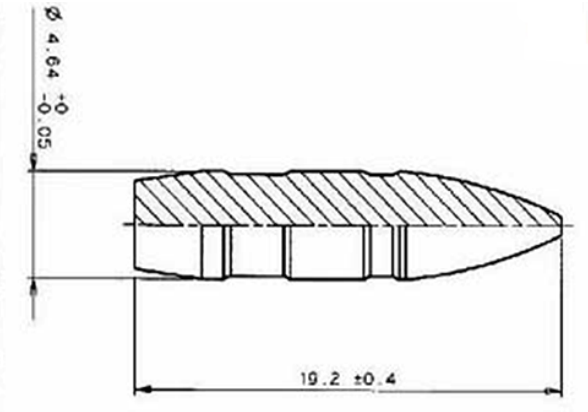

Figure 5.1: General sketch of bullet profile.

In order to correlate the self-healing behaviour to the polymers/blends properties, different kind of tests were carried out to characterize the materials object of study, in particular thermal and mechanical properties were measured by DSC, DMTA and tensile tests.

A TA Instruments DSC Q100 was used to perform DSC experiments in nitrogen atmosphere (50 ml/min) and a heating ramp of 10 °C/min has been set for all tests. The different EMAA-30Na/EVOH and EMAA-30Na/ENR50 blends were tested in the temperature range between 0 °C and 180 °C and of -50 °C and 120 °C, respectively. In this last set of DSC experiments, the glass transition temperature (T_g) related to the elastomeric phase was taken as the inflection point of the heat capacity vs temperature curve.

The measurements of shear storage modulus (G'), shear loss modulus (G'') and phase angle (tanδ) were performed on a Rheometrics RDA II rheometer. A rectangular geometry and torsional deformation (1% strain), oscillating at the frequency of 1 Hz, were chosen to obtain the moduli as function of temperature from 20 °C to 100 °C. Rheological properties were also analysed using the same test apparatus equipped with 25 mm parallel plates geometry and circular samples with thickness varying between 1 and 2 mm; for this purpose, frequency sweep tests (0.5 Hz to 50 Hz) were repeated at different temperatures in the range from 120 °C to 180 °C.

Uniaxial tensile tests were conducted following ASTM D638 procedure using an Instron 4302. All the experiments were performed at room temperature (about 23 °C) on sample with a thickness of 2±0.1 mm and setting a cross-head rate of 10 mm/min.

5.3 Results and discussion

5.3.1 Ballistic impact tests

The base materials and the related prepared blends exhibited a different response after ballistic puncture tests. The healing capability of each material after impact was evaluated by the optical microscope and by SEM; a leakage test was also performed. No healing was observed for pure EVOH, while pure EMAA-Na showed at the adopted testing condition a complete hole closure, as expected. Self-repairing behaviour was also observed in pure ENR50 slightly cross-linked with 0.2, and 0.5 wt% DCP, however, due to the intrinsic thermoset feature of the studied elastomeric system, a different healing process, based on chain interdiffusion, could be assumed. Further analyses are required for a complete understanding of this behaviour.

Blends containing 15 and 30 wt% of EVOH showed an efficient self-healing capability (Figure 5.2-a and 5.1-b) and only the blend containing 50 wt% EVOH showed a clear brittle fracture, with a through-hole and only partial reduction of damage area (Figure 5.2-c). Moreover, SEM analysis supported the previously mentioned two stage healing process required for the complete hole sealing after bullet passage (Figure 5.2-d). From microscope analysis further considerations can be

pointed out; in healed specimens a melted zone is observable nevertheless, in majority of the cases, the bullet puncture produced clear radial cracks detectable in the projectile entry side. This fracture feature is directly linked to the amount of EVOH phase in the blends, the higher the crystalline phase the greater the brittle behaviour.

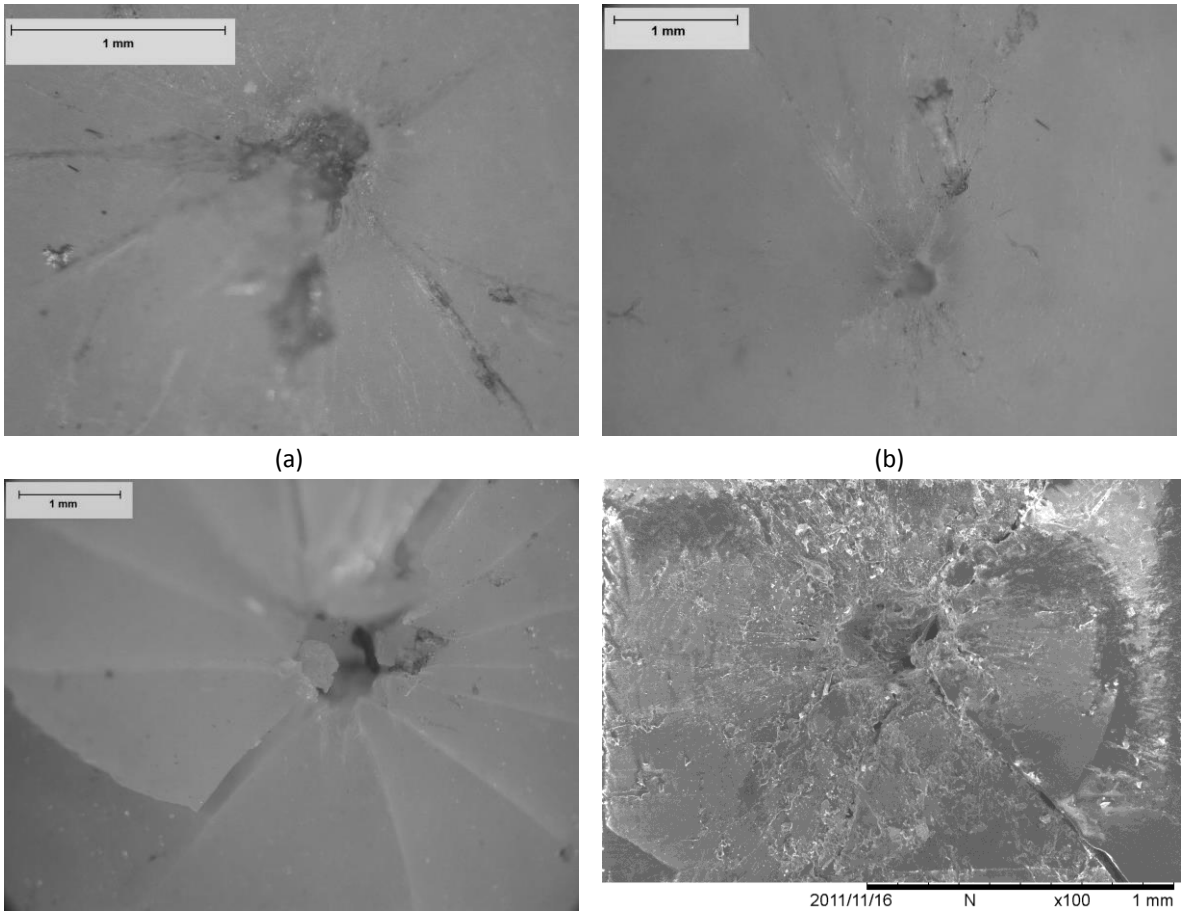

(a) (b)

(c) (d)

Figure 5.2: Optical imagines of 85/15 (a), 70/30 (b), 50/50 (c) EMAA-30Na/EVOH blends and SEM micrograph of 70/30 relative blend (projectile entry side).

Figure 5.3 shows the optical micrographs of bullet impact zones of blends containing 15, 20, 30, and 50 wt% ENR50, respectively. Interestingly, vacuum tests confirmed that all the EMAA-30Na/ENR50 blends exhibited a preservation of self-repairing effect.

It is evident that the presence of the elastomeric second phase does not affect the self-healing behaviour of the materials even when high ENR50 contents are considered. However, it was observed that even when air tightness was restored, a small blind hole remains in the projectile entrance zone indicating that full closure occurs only in a portion of the whole plate thickness (Figure 5.4-a). It can be noticed that also in this case the hole is remarkably smaller than the bullet

dimensions, suggesting a consistent deformation recovery that effectively contributed to healing process.

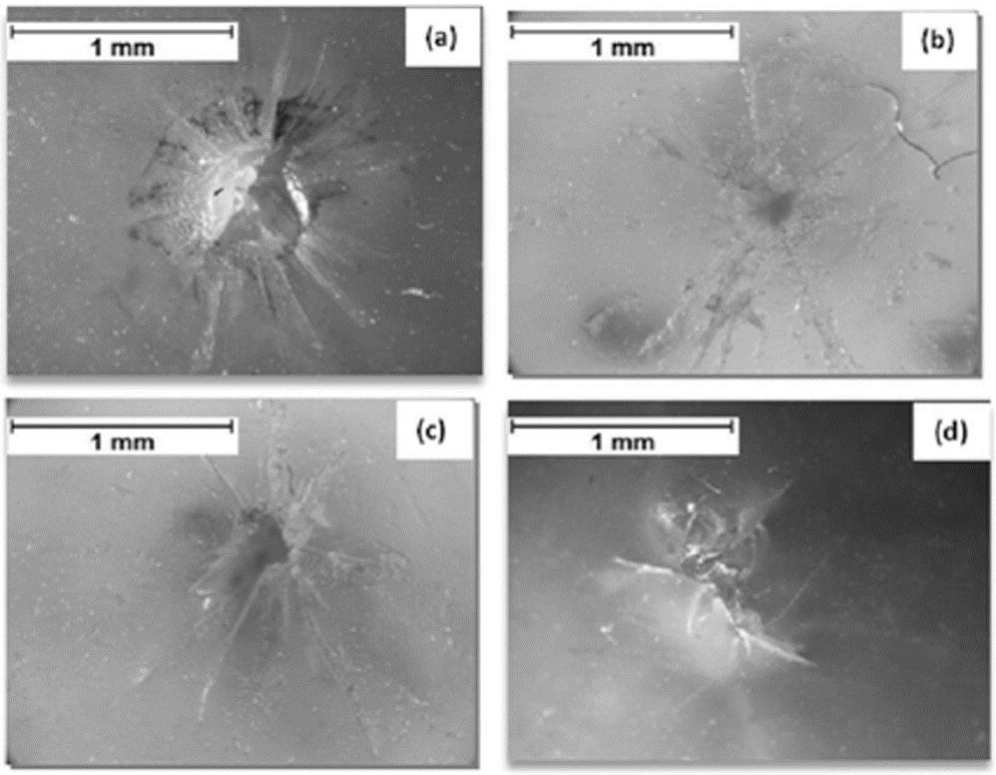

Figure 5.3: Optical micrographs of bullet impact zones (exit zones) of self-healed EMAA-30Na/ENR50 blends containing (a) 15, (b) 20, (c) 30, and (d) 50 wt % ENR50.

EMAA-30Na ionomer blended with non-crosslinked ENR50 gave the greater healing capability, however, it was observed that even with DCP vulcanized rubber, both EMAA-30Na/ENR50 blends (Figure 5.4-a,-b,-c) and pure crosslinked rubber (Figure 5.4-d) maintained an effective self-healing capability.

The increase of the curing agent (DCP) had an effect on the material responses after high-energy impacts. The morphology of the damaged areas changed showing a more “brittle” fracture (extended radial cracks are observable) for specimens with the higher DCP content. Although less evident than in the previous case where EVOH produced a higher crystal phase content in the blends, these results demonstrated that also the reduced molecular mobility of the elastomeric phase has an effect on the global self-repairing capability both in EMAA-30Na/ENR50 blends and pure ENR50 rubber.

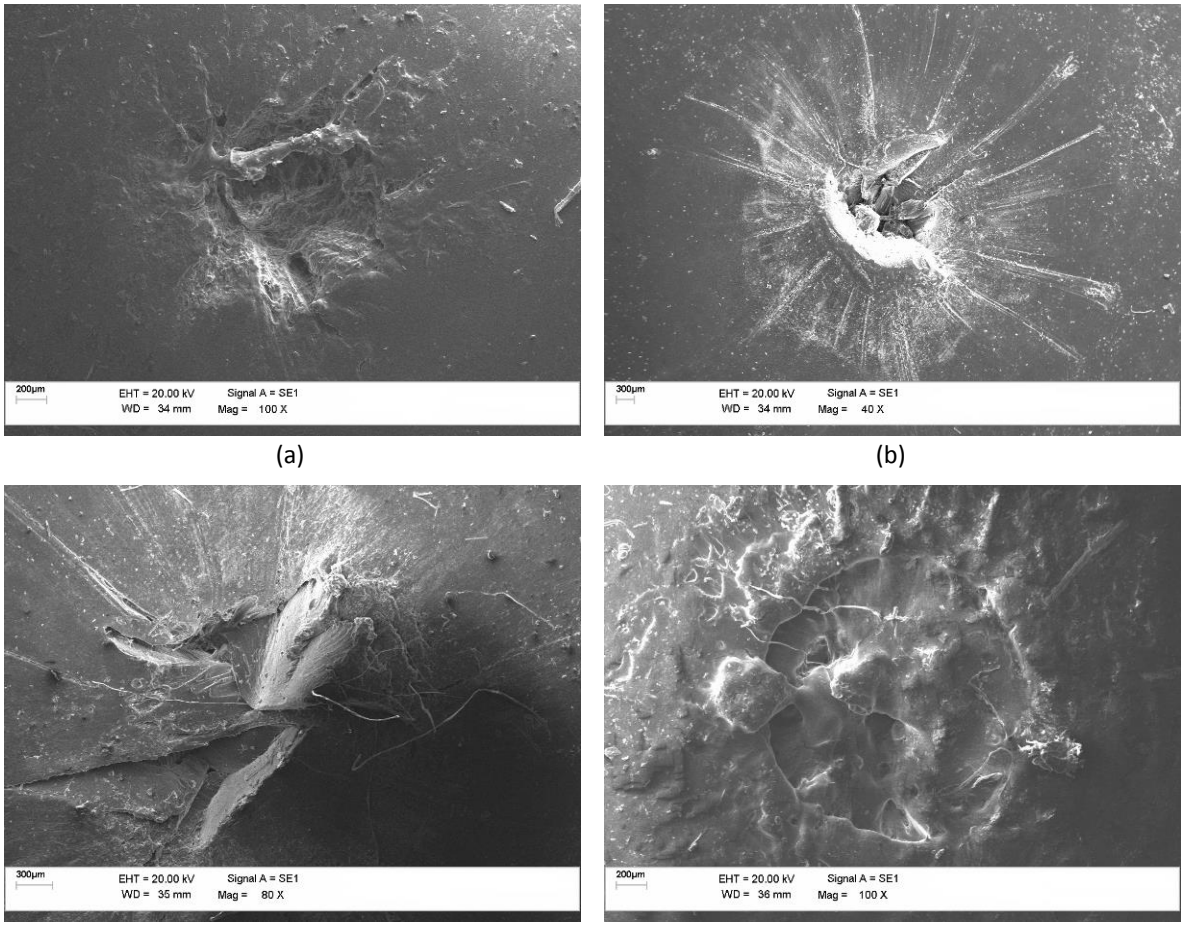

Figure 5.4: SEM micrographs of 50/50 (a), 50/50 with 0.2 DCP, 50/50 with 0.5 DCP (c) and ENR50 with 0.5 DCP (d) damaged areas after ballistic impact tests.

Preliminary impact tests in the low velocity (180 m/s) and hypervelocity (4 km/s) ranges performed firing spherical projectiles on EMAA-30Na/ENR50 blends indicated a marked difference in the material response. At low impact speed complete hole closure and sealing occurred (Figure 5.5-a). On the contrary, at hypervelocity, neither self-healing behaviour nor hole closure effect took place; indeed a clear-cut hole with a diameter of approximately the same dimension of the impacted object was detected (Figure 5.5-b). Moreover a degradation of the elastomeric phase caused by the high temperature in the impacted area could be hypothesized.

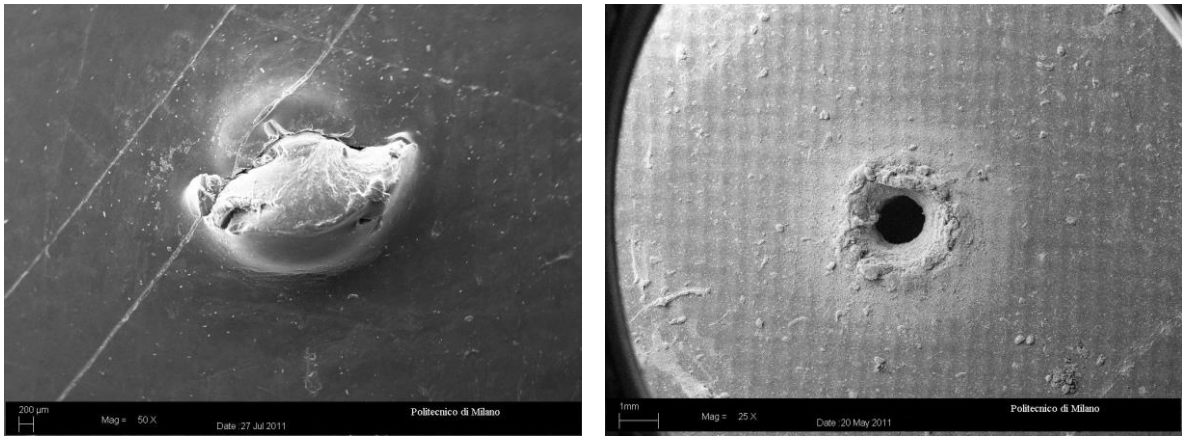

(a) (b)

Figure 5.5: Preliminary test blends (50/50) d = 5 mm t = 2 mm 180 m/s low and hypervelocity d = 1.5 mm t = 2 mm 4 km/s.

5.3.2 Thermal and rheological properties

The possibility of welding after puncture is related to the thermal-rheological behaviour of the studied materials. DSC and DMTA experiments were conducted for all the different blends in order to determine glass transition temperatures, melting temperatures and enthalpies which are considered crucial factors in the understanding the self-healing behaviour.

DSC results regarding EMAA-30Na/EVOH blends are summarised in Table 5.2. All the mixtures showed three melting peaks that occur in temperature ranges consistent with those of pure components (Figure 5.6), however variations of a few degrees were observed; while both melting temperatures of primary and secondary crystal phases (T_{m1} and T_{m2}) related to the ionomeric component in the blends did not show substantial alterations, the melting temperature of EVOH phase (T_{m3}) increases up to about 7 °C. Also the fusion enthalpies of both ionomeric crystal phase and EVOH phase in the blends showed remarkable increment compared to pure components.

It is clear that the presence of EVOH increases the crystallinity of EMAA-30Na phase. This effect is detectable in the rise of enthalpies associated to the melting process of the primary ionomeric crystal phase at about 90 °C in the blends. At the same time, an increase in crystallinity of EVOH phase is also observed, although to a more limited extent. From these results it is apparent that the presence of two different crystalline phases in the blends makes the crystallization process easier for each component. Moreover, it is worth to point out that IR analysis performed during impact tests at low projectile velocity on the ionomer (Chapter 2) indicated a temperature rise up to about 120 °C in the damaged zone and different global crystal phase content and related

melting temperature affected the chance of welding by melting and recrystallization in the puncture zone of EMAA-30Na/EVOH blends as observed in the previous paragraphs.

Table 5.2: Thermal properties of EMAa-30Na/EVOH blends.

EMAA-30Na/EVOH [%]	T_{m2} [°C]	T_{m1} [°C]	ΔH_{m1}/EMAA-30Na[a] [J/g]	T_{m3} [°C]	ΔH_{m3}/EVOH[b] [J/g]
100/0	51	95.4	26.5	-	-
85/15	51	93.3	68.9	154.9	59.7
70/30	51.2	90.6	64	161.4	76.3
50/50	n.d.	91.3	64.4	163.7	80.6
0/100	44	-	-	156.6	68.2

[a]Enthalpy normalized over EMAA-30Na phase

[b]Enthalpy normalized over EVOH phase

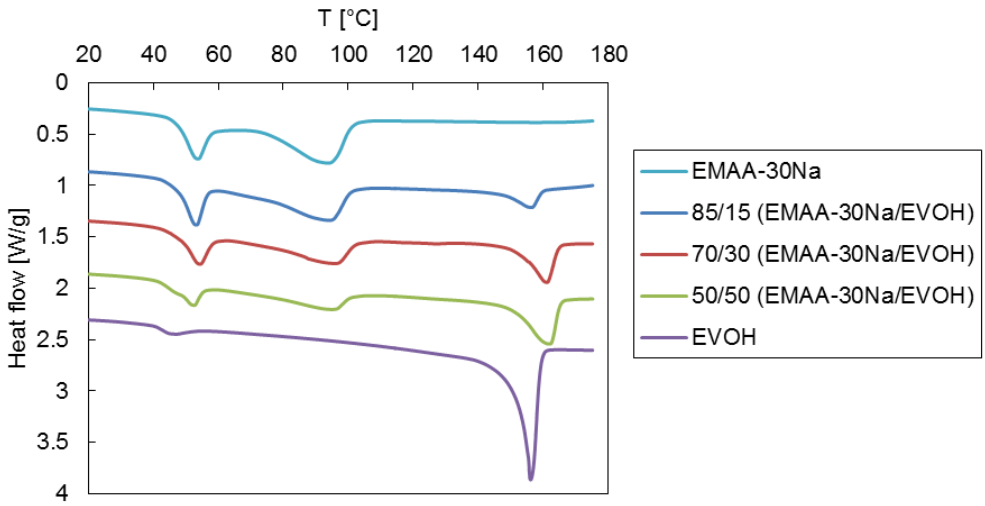

Figure 5.6: DSC results of EMAA-30Na/EVOH blends.

A different thermal behaviour is presented by EMAA-30Na/ENR50 blends, which show one glass transition and two melting peaks (Figure 5.7). Results are presented in Table 5.3. The first transition temperature (T_g) is well below room temperature, consistent with the rubber phase, and the other two melting points at about 50 °C and 95 °C, consistent with the ionomeric phase. In these blends, no significant variation in all the transition temperatures was observed for each composition; only a negligible depression of primary crystal melting point can be detected (T_{m1}), however, a remarkably higher melting enthalpy of this crystal phase, compared to pure ionomer,

was observed (as in blends with EVOH). These results indicate an easier crystallization of EMAA-30Na as consequence of ENR50 addition and confirm the presence of a consistent amount of crystallisable phase, even at the highest rubber contents. Nevertheless the distribution between crystalline and rubbery phase allowed an efficient global self-healing response for all the compositions of EMAA-30Na/ENR50 blends.

Table 5.3: Thermal properties of EMAA-30Na/ENR50 blends.

EMAA-30Na/ENR [%]	T_g [°C]	T_{m2} [°C]	T_{m1} [°C]	ΔH_{m1}/EMAA-30Na[a] [J/g]
100/0	-	51	95.4	26.4
85/15	-20	51	94.0	62.7
70/30	-20	51	93.3	45.3
50/50	-20	51	93.0	56
0/100	-20	-	-	-

[a]Enthalpy normalized over EMAA-30Na content

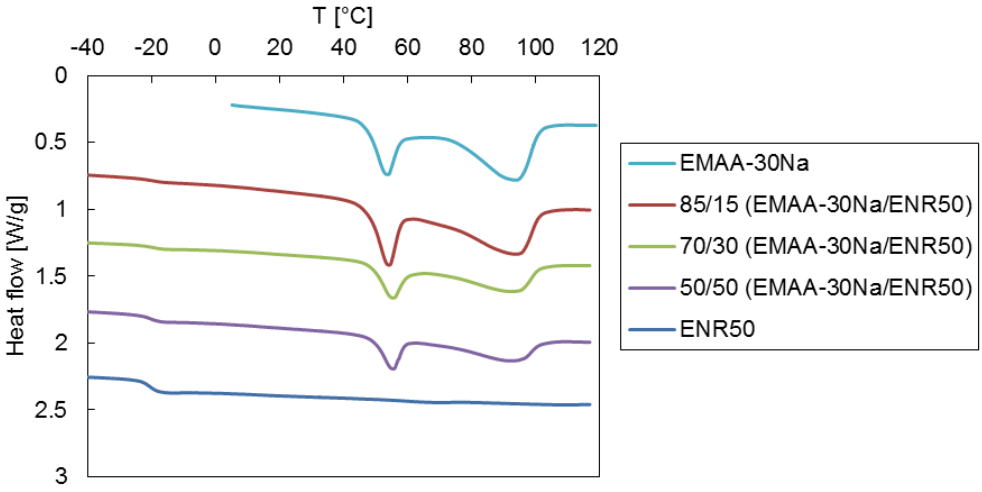

Figure 5.7: DSC results of EMAA-30Na/ENR50 blends.

The transition temperatures of the different blends measured with DSC experiments were also confirmed by DMTA (Figure 5.8). Two relaxation process occurred around 50 °C and 90 °C, both consistent with the melting of the two different crystal morphologies present in the ionomeric phase. Moreover, the variation in mechanical properties showed by the blends can also be estimated. Both the shear storage modulus and the shear loss modulus are higher and lower than

the pure ionomer in EMAA-30Na/EVOH and in EMAA-30Na/ENR50 blends, respectively. No appreciable variation was seen instead for the tanδ.

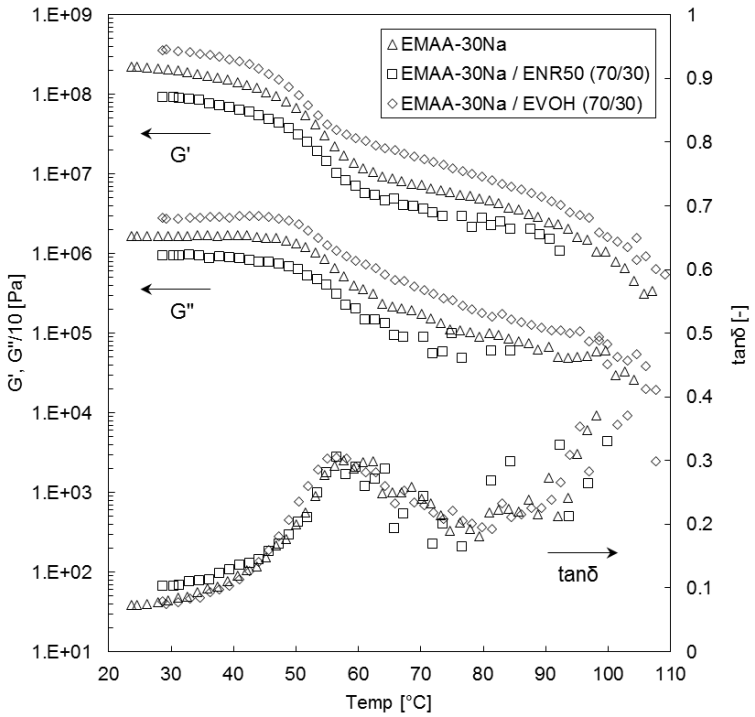

Figure 5.8: DMTA results for different blends and pure ionomer.

Complex viscosity measurements of pure EMAA-30Na, EMAA-30Na/EVOH (70/30) and EMAA-30Na/ENR50 (70/30) showed that the melt viscosity of blends with EVOH is higher than that of pure sodium ionomer at any tested temperature and that in such materials, as expected, viscosity reduces on increasing temperature and frequency (Figure 5.9-a). The blend with ENR50 showed a different behaviour (Figure 5.9-b): while at the lowest temperature (120 °C) melt viscosity of the blend is very similar to that of pure ionomer, on increasing temperature the blend presented a viscosity remarkably higher. This effect may be caused by rubber crosslinking, which becomes possible at temperatures above 120 °C; this hypothesis is supported by viscosity measurements conducted at 180 °C at different times (Figure 5.10): a remarkable increase of viscosity with time was detected. Whether this modification involved the ionomeric polymer, it could also affect the self-healing behaviour and further studies are required.

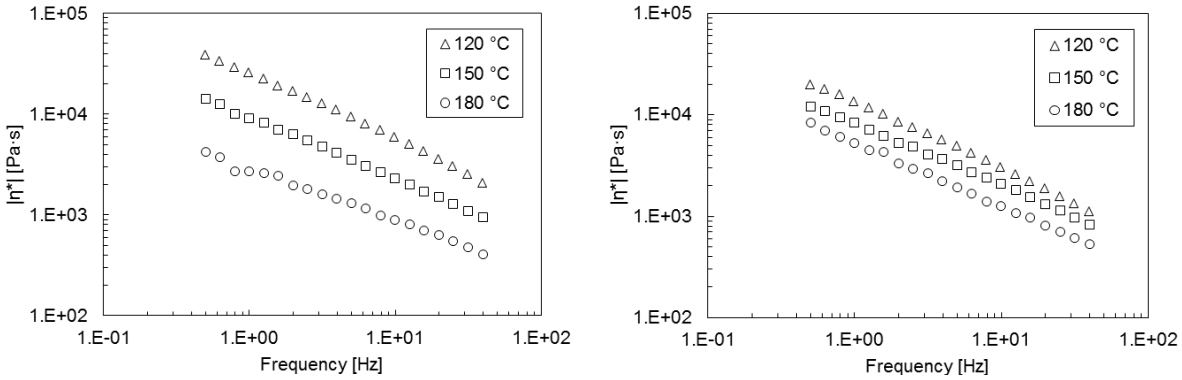

Figure 5.9: Complex viscosity for EMAA/EVOH (a) EMAA-30Na/ENR50 (b) blends measured at different temperatures.

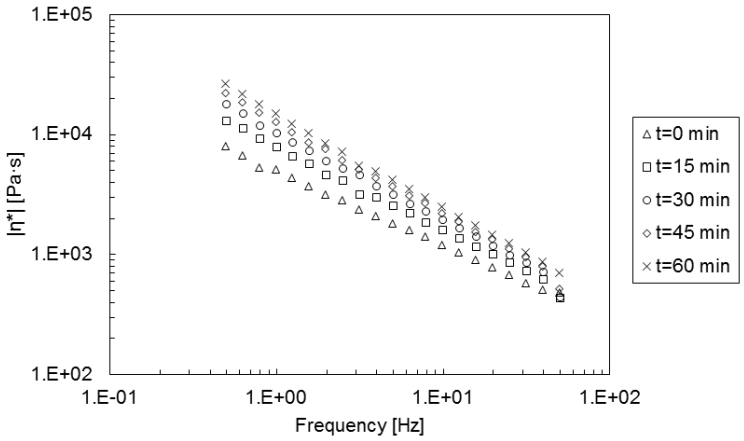

Figure 5.10: Complex viscosity evolution with time of EMAA-30Na/ENR50 (70/30) measured at 180 °C.

5.3.3 Mechanical properties

Performed mechanical tests show that in ENR50 based blends strength, strain at break and tensile stiffness decrease with decreasing ionomer content (Figure 5.11). The presence of a low modulus elastomeric phase explains the reduction in tensile stiffness of these blends. Further mechanical tests were carried out in order to evaluate the mechanical properties of EMAA-30Na/ENR50 blends with different crosslinking levels of the elastomeric phase; obtained results are summarised in Table 5.4. The reported effect of vulcanization by addition of DCP in the studied blends was a general increase in tensile strength, while no clear effect over modulus can be evidenced.

On the other hand, in EMAA-30Na/EVOH blends, the presence of stiff semi-crystalline thermoplastic polymer leads to an increase of the tensile modulus (Figure 5.11-c and Figure 5.12)

while, in this case, it seems that the tensile strength is not severely influenced by the presence of a more rigid phase (Figure 5.11-a). Also in this case, increasing EVOH content a marked reduction of strain at break was detected.

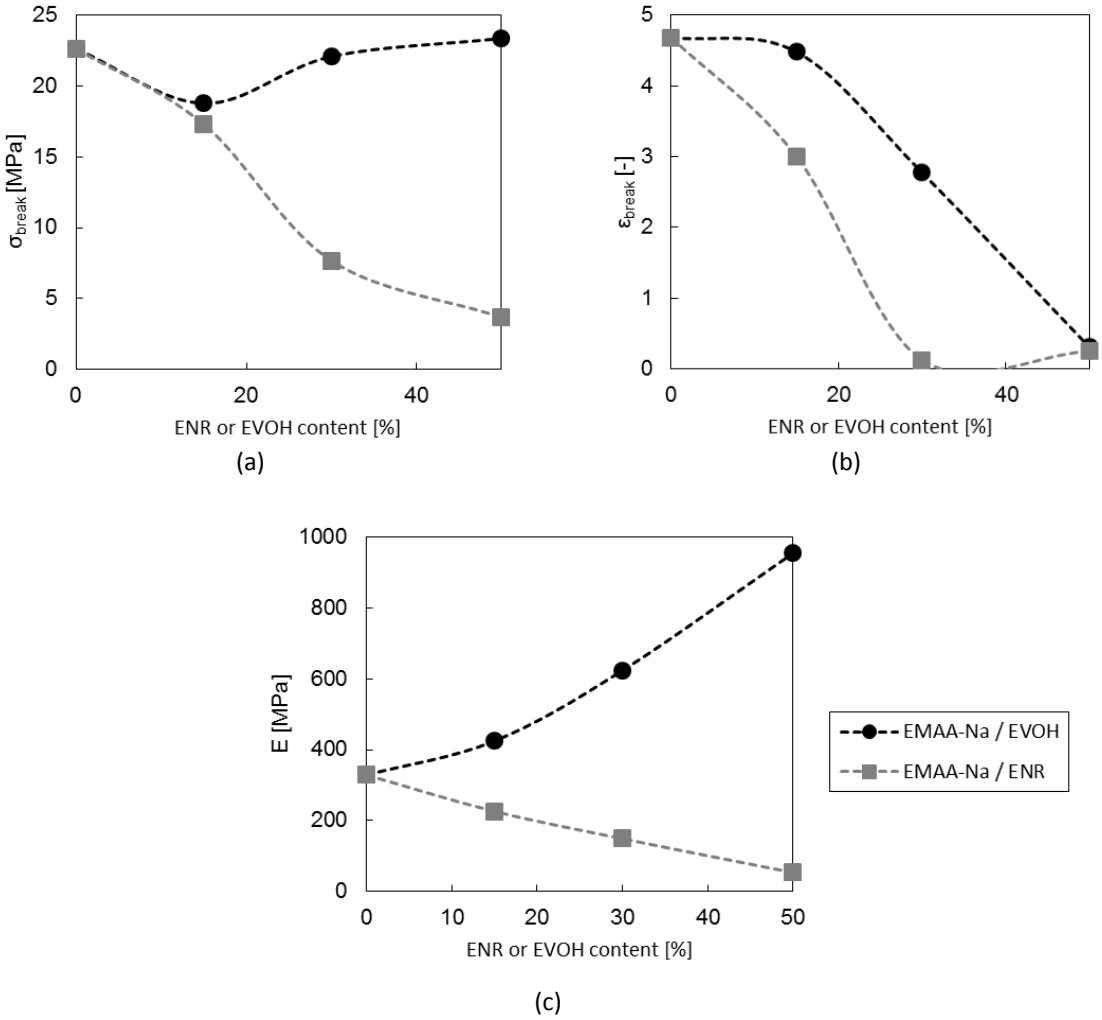

Figure 5.11: EMAA-30Na/EVOH and EMAA-30Na/ENR mechanical properties: stress at break (a), strain at break (b) and tensile modulus (c).

Obtained results suggest, for both blend systems, a lower cohesion between the different phases decreasing ionomer content. This effect is more evident in EMAA-30Na/ENR50 blends; nevertheless, the higher chain mobility and lower mechanical properties of the introduced rubbery phase did not affect the self-healing capability of such blends. Conversely, in EVOH based blends, the higher crystallinity and related higher mechanical properties decreasing EMAA-30Na content, led to a reduction in the self-repairing ability disappearing for a 50 wt% EVOH content.

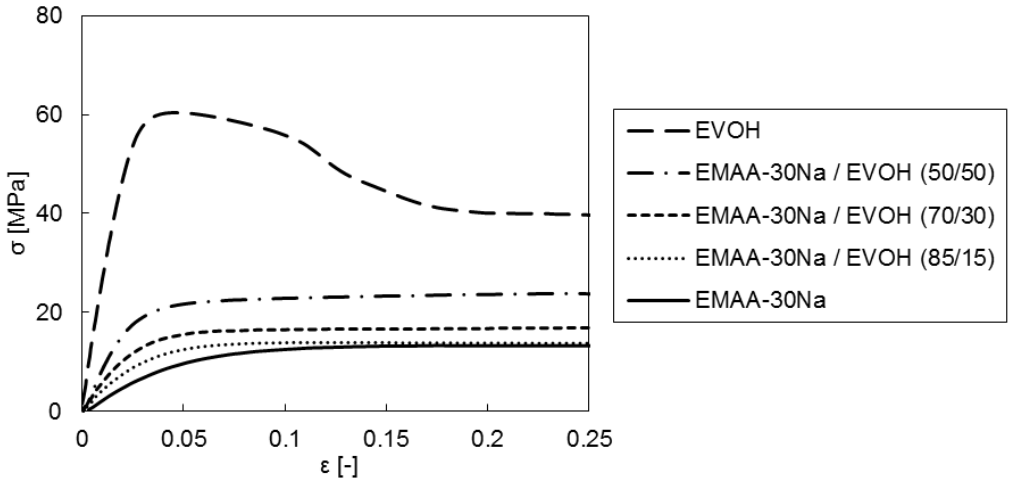

Figure 5.12: Tensile test results on EVOH based blends (10 mm/min).

Table 5.4: Effect of DCP on the mechanical properties of ENR50 based blends.

EMAA-30Na/ENR [wt%]	DCP [wt%]	Tensile Strength [MPa]	Tensile Modulus [MPa]
70/30	0	7.7	148
	0.2	8	204
	0.5	9	179
50/50	0	3.7	52
	0.2	5	38
	0.5	6	26

5.4 Conclusions

The self-repairing behaviour of a number of polymer blends based on EMAA-30Na ionomer after ballistic puncture tests was investigated. The results presented show that the self-healing behaviour is well maintained in EMAA-30Na/EVOH blends up to 30% EVOH. On the contrary, when ENR50 is employed, the optical micrographs and de-pressurized airflow tests detected the complete self-repairing behaviour for all compositions of tested EMAA-30Na/ENR50 blends under impact these conditions. Also ENR50 itself shows self-repairing behaviour in the same experimental conditions, however a different healing process could be assumed. In addition, obtained results demonstrated the effect of the reduced molecular mobility of the ENR50 phase on the global self-repairing capability both in pure rubber and blends when a crosslinking agent (DCP) is used. Preliminary impact tests at low and hypervelocity highlighted the rate dependency

in the self-repairing behaviour of EMAA-30Na/ENR50 blends, in particular at the highest projectile speed no healing was observed. These results seem to indicate that the presence of melted material is a requirement for a complete hole closure and welding/sealing of the damaged area after high velocity impact providing an additional support to the hypothesis of a two stage healing process.

Summarising, ionomer based blends with various polymers, elastomer or thermoplastic, were developed, thus providing a mean to select material properties. The availability of blends with physical and mechanical properties modulated over a wide range, yet maintaining an efficient self-repairing behaviour, could remarkably extends the potential application areas of such materials.

Chapter 6 - Conclusion

6.1 Remarks and conclusions

The main objective of this research is the development of new self-healing polymeric systems tailored for aerospace applications. EMAA based polymers, showing self-healing capability after high-energy impact, were selected and extensively tested under various experimental conditions. Critical parameters for an efficient self-repairing phenomenon were individuated, in particular the roles of sample thickness / projectile diameter ratio (t/d), projectile velocity and neutralization level were identified. In this view, a relation between such parameters can also be estimated; as summarised in Figure 6.1, the results obtained for the EMAA-30Na ionomer indicate an increase in the t/d ratio required for a complete hole closure increasing projectile speed. Furthermore SEM analysis revealed a different morphology of the impacted sites underlining an extended melted zone in samples tested at the highest projectile velocities.

Similar self-healing behaviour was observed for the EMAA copolymer (no neutralization) in the bullet speed range between 180 and 400 m/s. Conversely, the polymer with the highest neutralization level, EMAA-60Na, showed a dissimilar response during low velocity impact tests exhibiting an efficient self-healing capability only from mid velocity ballistic experiments (400 m/s), consistent with the results obtained for the other polymers.

The remarkable healing ability demonstrated by the EMAA-30Na ionomer even after hypervelocity impacts (up to 4 km/s) could promote a potential use in the aerospace field, however further investigations are required in order to achieve a complete understating of the phenomenon. Moreover, experiments at hypervelocity speed were not performed on EMAA and EMAA-60Na polymers.

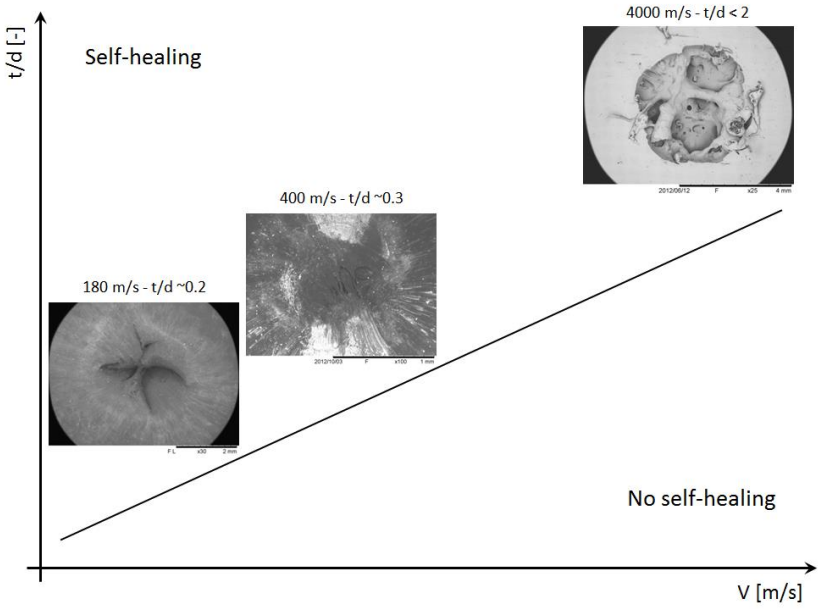

Figure 6.1: EMAA-30Na sample thickness / projectile diameter ratios (t/d) required for an efficient self-healing event after impact at various velocities.

According to these results new polymeric systems with self-healing capability were designed and manufactured: multilayers systems and polymeric blends, both based on EMAA-30Na ionomer. In the first case, hybrid composites coupling several materials and the ionomer were tested under different impact conditions in order to evaluate the response of the self-healing polymer embedded in a complex structure. In the second case, the same EMAA based iononer was blended with a semi-crystalline stiff polymer or an elastomer; the produced blends have physical and mechanical properties modulated over a wide range, yet maintaining an efficient self-repairing behaviour. Further improvements of the developed polymeric systems can be achieved controlling the nanostructure of the produced materials [169].

These new results confirm how ionomer based materials may find employment in multifunctional structures for aerospace applications, indeed, the design of both aeronautic and space structures must take into account the probability of impact during the operational life with debris or, in space applications, with micrometeoroids.

In the aeronautic field, multilayer wall fuel tanks may be a direct application for these self-healing materials. Fuel self-sealing after perforation was obtained as a result of swelling or chemical reaction of rubber/foam layer when it comes in contact with the spilling internal liquid. A usual drawback of these materials is the limited resistance to aging, which reduces their effectiveness with time. Moreover, the sealing material adds consistent weight to the component, yet giving no

or negligible contribution to structural performance. Polymeric materials and composites with intrinsic self-healing capability may become a valid alternative to these traditional configurations. The combination of aramid fabric or carbon foams with polymers able to restore, at least partially, the continuity of the material may provide significant protection and fluid containment capacity even in particularly critical conditions. In this context, ethylene-methacrylic acid based ionomers have widely demonstrated their efficiency to autonomously repair after bullet punctures and can be taken into consideration as self-healing layers in tanks.

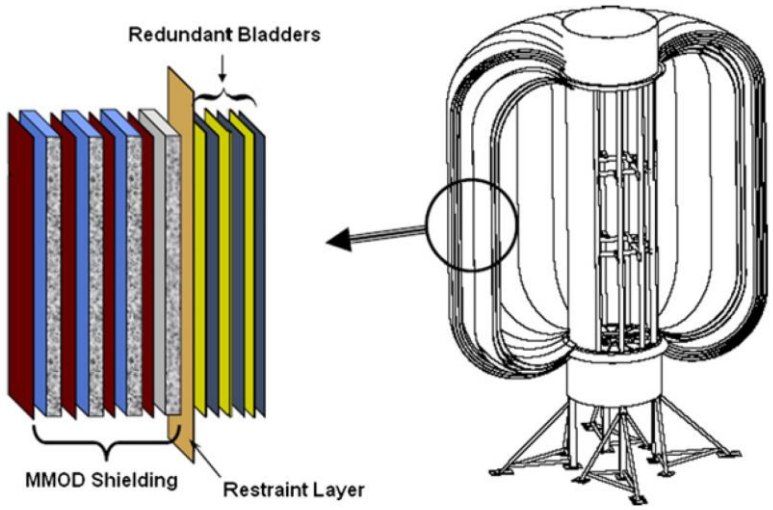

Figure 6.2: Schematic view of the TransHab inflatable structure [170].

Regarding the space field, in recent years, the amount of space debris has increased significantly and nowadays every spacecraft must face orbital manoeuvres to avoid the collision with major objects. Nevertheless the number of smaller objects (<1 cm), which are difficult to monitor by ground stations, is continuously growing due to space collisions and explosions. In some regions of space environment, incidentally the most interesting for space activities such as the Low Earth Orbits (LEO) region, their concentration is so high that an impact with a spacecraft is almost a sure thing during the operational lifetime [171]. Even if small sized, these objects travel at orbital velocity (~km/s), so that impact events involve a great energy amount and are seriously dangerous for space systems, especially for electronic units and pressurized systems, such as tanks or habitable modules. In this scenario, it is evident how important is the availability of materials which can self-repair after an impact and avoid any pressure leakage. Nevertheless, the rough conditions of the space environment limit the usability of many of existing self-healing systems [172]. For all these reasons, it would be very important to include a self-healing

materials, such as EMAA based polymers or ionomers, in multifunctional composite structures in order to employ them in space systems (Figure 6.2).

This opportunity could highly increase the reliability of future spacecrafts allowing a longer duration of mission for deep space exploration and a safer environment for astronauts against pressure leakage. However, materials intended to be used in space missions must be extensively tested in order to investigate their behaviour once exposed to space environment conditions, as required by the main space agencies.

Appendix A

In order to study physical or mechanical property changes once exposed to space conditions preliminary outgassing test carried out. When exposed to high vacuum for long time period, some materials, especially polymers, may exhibit considerable mass reduction due to diffusion and loss of volatile substances; this can significantly affect material physical and mechanical properties, thus posing a severe limit to its employment in space applications. In this view, thermal outgassing tests were performed to investigate the ionomer behaviour in conditions similar to those encountered in space environment. Using a high vacuum chamber, specimens were exposed to thermal cycles in vacuum environment.

The aim of outgassing tests is to evaluate the loss of mass of the material when exposed to high vacuum condition. Outgassing phenomena require a long time exposure to show clear effects, but it was observed that this phenomenon is accelerated by high temperature. In order to achieve appreciable results in a reasonable time span, thermal cycles are usually performed during vacuum exposure. Experiment was performed according to ECSS-Q-ST-70-02.

A thermal vacuum chamber was employed, which is able to reach high vacuum condition (up to 10^{-9} bar) and is equipped with two independent heating sources: a heated steel plate, where the specimens were placed, and a radiant heating system. Three flat rectangular EMAA-30Na specimens measuring about 120x120x2 mm were tested.

All specimens were cleaned and then stored at 22±3°C and 55±10% RH for 30 days after manufacturing; the weight of each sample was measured immediately before the test. During the experiment a pressure of about 10^{-8} bar was maintained in the chamber for 43 hours (Figure B.1-a). Two thermal cycles at 60 °C were also performed in order to promote any outgassing phenomenon: the first cycle was performed only using the conductive steel plate while the second used also the radiant heating system. Temperature was monitored both on the steel plate and on one of the specimens using thermocouples. The weight of each sample was measured immediately after the test and then two weeks later in order to evaluate any mass variation.

The mass variations of the plate specimens recorded after thermal vacuum outgassing tests are reported in Table B.1. The results indicate that EMAA-30Na ionomer is not significantly affected by outgassing phenomena. The scarce mass loss, showed by the two samples immediately after the test, is to a large extent due to humidity diffusion, as confirmed by the weight regain exhibited by all the samples after storage for two weeks at 22±3°C with a relative humidity of 55±10%.

Observing the temperature profile in Figure B.1-b it can be noticed that during the first thermal cycle the material did not reach the target temperature of 60°C, while in the second cycle the material immediately reached the target temperature; this is due to the better efficiency of the radiant heating compared to conductive heating. Comparing the temperature and pressure profiles it can be pointed out that the most of mass release occurred when the material reached the fixed temperature (Figure B.1-a). This confirms the importance of temperature in promoting the outgassing and ensures that any phenomenon was fairly concluded at the end of the test.

Table B.1: Thermal outgassing test results

Sample ID	Weight [g]			Variation [%]	
	Before test	After test	After 2 weeks	After test	After 2 weeks
1	27.730	-	27.719	-	-0.039%
2	30.574	30.544	30.559	-0.098%	-0.049%
3	28.196	28.168	28.180	-0.099%	-0.057%

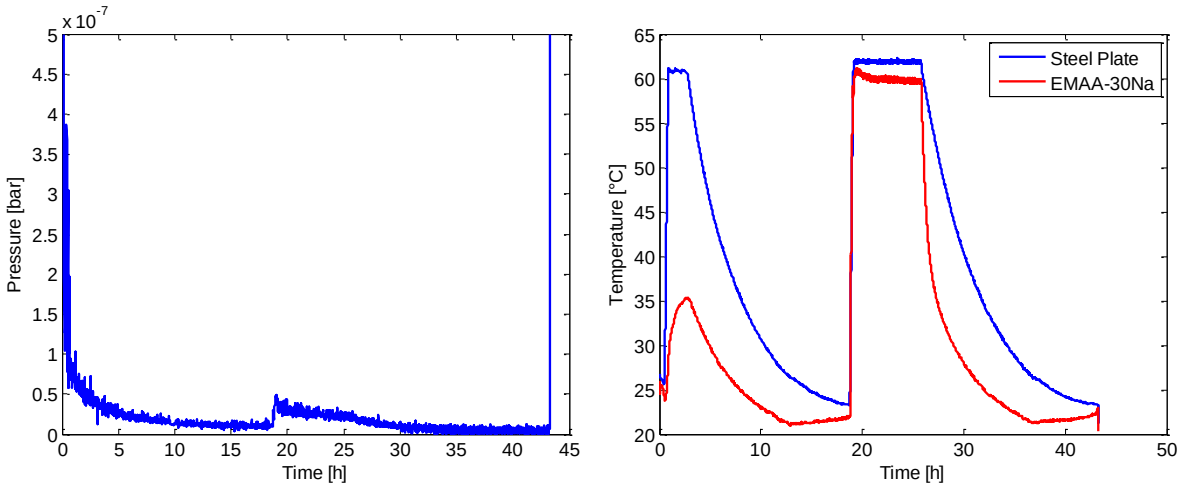

(a) (b)

Figure B.1: Thermal outgassing test results

Thermal outgassing test showed that the considered material is not significantly affected by outgassing phenomena. These results suggest that a future employment of EMAA-30Na ionomers as self-healing materials in space applications could be further evaluated.

Bibliography

[1] C. Dry, *Smart Mater. Struct.* **1994**, *3*, 118-123.

[2] C. Dry, *Compos. Struct.* **1996**, *35*, 263-269.

[3] S. R. White, N. R. Sottos, P. H. Geubelle, J. S. Moore, M. R. Kessler, S. R. Sriram, E. N. Brown, S. Viswanathan, *Nature* **2001**, *409*, 794-797.

[4] J. W. C. Pang, I. P. Bond, *Composites A* **2005**, *36*, 183-188.

[5] J. W. C. Pang, I. P. Bond, *Compos. Sci. Technol.* **2005**, *65*, 1791-1799.

[6] S. van der Zwaag, N. H. van Dijk, H. M. Jonkers, S. D. Mookhoek, W. G. Sloof, *Philos. Trans. A Math. Phys. Eng. Sci.* **2009**, *367*, 1689-1704.

[7] S. van der Zwaag, *Self Healing Materials: an alternative approach to 20 centuries of materials science*, Springer, 2007.

[8] M. D. Hager, P. Greil, C. Leyens, S. van der Zwaag, U. Schubert, *Adv. Mater.* **2010**, *22*, 5424-5430.

[9] S. J. Garcia, H. R. Fischer, S. van der Zwaag, *Prog. Org. Coat.* **2011**, *72*, 142-149.

[10] E. N. Brown, N. R. Sottos, S. R. White, *Exp. Mech.* **2002**, *42*, 372-379.

[11] E. N. Brown, S. R. White, N. R. Sottos, *J. Mater. Sci.* **2004,** *39*, 1703-1710.

[12] E. N. Brown, S. R. White, N. R. Sottos, *Compos. Sci. Technol.* **2005**, *65*, 2474-2480.

[13] T. C. Mauldin, J. D. Rule, N. R. Sottos, S. R. White, J. S. Moore, *J. R. Soc. Interface* **2007**, *4*, 389-393.

[14] J. D. Rule, E. N. Brown, N. R. Sottos, S. R. White, J. S. Moore, *Adv. Mater.* **2005**, *17*, 205-208.

[15] G. O. Wilson, J. S. Moore, S. R. White, N. R. Sottos, H. M. Andersson, *Adv. Func. Mater.* **2008**, *18*, 44-52.

[16] H. Jin, C. L. Mangun, D. S. Stradley, J. S. Moore, N. R. Sottos, S. R. White, *Polymer* **2012**, *53*, 581-587.

[17] S. H. Cho, H. M. Andersson, S. R. White, N. R. Sotto, P. V. Braun, *Adv. Mater.* **2006**, *18*, 997-1000.

[18] M.W. Keller, S.R. White, N.R. Sottos, *Adv. Funct. Mater.* **2007**, *17*, 2399–2404.

[19] M.W. Keller, S.R. White, N.R. Sottos, *Polymer* **2008**, *49*, 3136–3145.

[20] K. Sanada, I. Yasuda, Y. Shindo, *Plast. Rubber Compos.* **2006**, 35, 67-72.

[21] K. Sanada, N. Itaya, Y. Shindo, *The Open Mechanical Engineering Journal* **2008**, 2, 97-103.

[22] B. J. Blaiszik , M. Baginska , S. R. White, N. R. Sottos, *Adv. Funct. Mater.* **2010**, 20, 3547-3554.

[23] A. R. Jones, B.J. Blaiszik, S.R. White, N. R. Sottos, *Compos. Sci. Technol.* **2013**, 79, 1-7.

[24] R.S. Trask, I.P. Bond, *Smart Mater. Struct.* **2006**, *15*, 704-710.

[25] R. S. Trask, G. J. Williams, I. P. Bond, *J. R. Soc. Interface* **2007**, *4*, 363-371.

[26] C. J. Norris, I. P. Bond, R. S. Trask, *Composites A* **2011**, *42*, 639-648.

[27] C. J. Norris, I. P. Bond, R. S. Trask, *Comp. Sci. Tech.* **2011**, 71, 847-853.

[28] C. J. Norris, J. A. P. White, G. McCombe , P. Chatterjee, I. P. Bond, R. S. Trask, *Smart Mater. Struct.* **2012**, 21, 094027.

[29] C. J. Norris, I.P. Bond, R. S. Trask, *Composites A* **2013**, 44, 78-85.

[30] K. S. Toohey, C. J. Hansen, J. A. Lewis, S. R. White, N. R. Sottos, *Adv. Func. Mater.* **2009**, 19, 1399-1405.

[31] A. R. Hamilton, N. R. Sottos, S. R. White, *Adv. Mater.* **2010**, 22, 5159-5163.

[32] A. P. Esser-Kahn, P. R. Thakre, H. Dong, J. F. Partrick, V.K. Vlasko-Vlasov, N. R. Sottos, J. S. Moore, S. R. White, *Adv. Mater.* **2011**, 23, 3654-3658.

[33] S. D. Mookhoek, H. R. Fischer, S. van der Zwaag, *Composite A* **2012**, 43, 2176-2182.

[34] X. F. Wu, A. L. Yarin, *J. Appl. Polym. Sci.* **2013**, 130, 2225-2237.

[35] Q. Chen, L. Zhang, A. Rahman, Z. Zhou, X. F. Wu, H. Fong, *Composites A* **2011**, 42, 2036-2042.

[36] S. Sinha-Ray, D. D. Pelot, Z. P. Zhou, A. Rahman, X. F. Wu, A. L. Yarin, *J. Mater. Chem.* **2012**, 22, 9138-9146.

[37] X. F. Wu, A. Rahman, Z. Zhou, D. D. Pelot, S. Sinha-Ray, B. Chen, S. Payne, A. L. Yarin, *J. Appl. Polym. Sci.* **2013**, 129, 1383-1393.

[38] D.Y Wu, S. Meure, D. Solomon, Prog. Polym. Sci. 2008, 33, 479-522.

[39] B. J. Blaiszik, S. L. B. Kramer, S. C. Olugebefola, J. S. Moore, N. R. Sottos, S. R. White, *Annu. Rev. Mater. Res.* **2010**, 40, 179-211.

[40] H. Jin, K. R. Hart, A. M. Coppola, R. C. Gergely, J. S. Moore, N. R. Sottos, S. R. White in: W. H. Binder, Self-healing polymers: from principles to applications, Wiley 2013.

[41] S. Billiet, X. K. D. Hillewaere, R. F. A. Teixeira, F. E. Du Prez, *Macromol. Rapid Comm.* **2013**, 34, 290-309.

[42] F. Herbst, D. Döhler, P. Michael, W. H. Binder, *Macromol. Rapid Comm.* **2013**, 34, 203-220.

[43] H. Meng, G. Li, *Polymer* **2013**, 54, 2199-2221.

[44] T. J. Swait, A. Rauf, R. Grainger, P. B. S. Bailey, A. D. Lafferty, E. J. Fleet, R. J. Hand, S. A. Hayes, *Plastics, Rubber and Composites* **2012**, 41, 215-224.

[45] J. M. Craven 'US patent 3.435.003', Patent US patent 3.435.003, 1969.

[46] X. Chen, M. A. Dam, K. Ono, A. Mal, H. Shen, S. R. Nutt, K. Sheran, F. Wudl, *Science* **2002**, 295, 1698-1702.

[47] X. Chen, F. Wudl, A. K. Mal, H. Shen, S. R. Nutt, *Macromolecules* **2003**, 36, 1802-1807.

[48] E. B. Murphy, E. Bolanos, C. Schaffner-Hamann, F. Wudl, S. R. Nutt, M. L. Auad, *Macromolecules* **2008**, 41, 5203-5209.

[49] Y. Wang, E. Bolanos, F. Wudl, T. Hahn, N. Kwok, *Proc. SPIE 'Behavior and Mechanics of Multifunctional Materials and Composites'*, San Diego, USA, **2007**, paper 65261I.

[50] J. S. Park, K. Takahashi, Z. Guo, Y. Wang, E. Bolanos, C. Hamann-Schaffner, E. Murphy, F. Wudl, H. T. Hahn, *J. Compos. Mater.* **2008**, 42, 2869-2881.

[51] F. Ghezzo, D. R. Smith, T. N. Starr, T. Perram, A. F. Starr, T. K. Darlington, R. K. Baldwin, S. J. Oldenburg, *J. Compos. Mater.* **2010**, 44, 1587-1603.

[52] A. M. Peterson, R. E. Jensen, G. R. Palmese, *ACS Appl. Mater. Interfaces* **2010**, 2, 1141-1149.

[53] Z. Xu, Y. Zhao, X. Wang, T. Lin, *Chem. Commun.* **2013**, 49, 6755-6757.

[54] Y. Chujo, K. Sada, A. Naka, R. Nomura, T. Saegusa, *Macromolecules* **1993**, 26, 883-887.

[55] Y. Chujo, K. Sada, R. Nomura, A. Naka, T. Saegusa, *Macromolecules* **1993**, 26, 5611-5614.

[56] J. Canadell, H. Goossens, B. Klumperman, *Macromolecules* **2011**, 44, 2536-2541.

[57] U. Lafont, H. Van Zeijl, S. Van Der Zwaag, *ACS Appl. Mater. Interfaces* **2012**, 4, 6280-6288.

[58] A. M. Peterson, R. E. Jensen, G. R. Palmese, *Compos. Sci. Technol.* **2011**, 71, 586-592.

[59] R. P. Sijbesma, F. H. Beijer, L. Brunsveld, B. J. B. Folmer, J. H. K. K. Hirschberg, R. F. M. Lange, J. K. L. Lowe, E. W. Meijer, *Science* **1997**, 278, 1601-1604.

[60] P. Cordier, F. Tournilhac, C. Soulié-Ziakovic, L. Leibler, *Nature* **2008**, 451, 977-980.

[61] F. Tournilhac, P. Cordier, D. Montarnal, C. Soulie-Ziakovic, L. Leibler, *Macromol. Symp.* **2010**, *291-292*, 84-88.

[62] G. Li, J. J. Wie, N. A. Nguyen, W. J. Chung, E. T. Kim, K. Char, M. E. MacKay, J. Pyun, *J.Polym. Sci. A* **2013**, 51, 3598-3606.

[63] A. C. Schüssele, F. Nübling, Y. Thomann, O. Carstensen, G. Bauer, T. Speck, R. Mülhaupt, *Macromol. Mater. Eng.* **2012**, 297, 411-419.

[64] A. Zhang, L. Yang, Y. Lin, L. Yan, H. Lu, L. Wang, *J. Appl. Polym. Sci.* **2013**, 129, 2435-2442.

[65] S. Burattini, H. M. Colquhoun, B. W. Greenland, W. Hayes, *Faraday Discuss.* **2009**, 143, 251-264.

[66] S. Burattini, B. W. Greenland, D. H. Merino, W. Weng, J. Seppala, H. M. Colquhoun, W. Hayes, M. E. MacKay, I. W. Hamley, S. J. Rowan, *J. Am. Chem. Soc.* **2010**, 132, 12051-12058.

[67] J. Fox, J. J. Wie, B. W. Greenland, S. Burattini, W. Hayes, H. M. Colquhoun, M. E. MacKay, S. J. Rowan, *J. Am. Chem. Soc.* **2012**, 134, 5362-5368.

[68] M. Burnworth, L. Tang, J. R. Kumpfer, A. J. Duncan, F. L. Beyer, G. L. Fiore, S. J. Rowan, C. Weder, *Nature* **2011**, 472, 334-337.

[69] N. Hohlbein, M. von Tapavicza, A. Nellesen and A. M. Schmidt: 'Self-Healing Ionomers', in 'Self-Healing Polymers', 315-334; 2013, Wiley.

[70] S. J. Kalista, T. C. Ward, *J. R. Soc. Interface* **2007**, 4, 405-411.

[71] S. J. Kalista, T. C. Ward, Z. Oyetunji, *Mech. Adv. Mater. Struc.* **2007**, 14, 391-397.

[72] R. J. Varley, S. Shen, S. van der Zwaag, *Polymer* **2010**, 51, 679-686.

[73] R. J. Varley, S. van der Zwaag, *Polym. Int.* **2010**, 59, 1031-1038.

[74] R. J. Varley, S. van der Zwaag, *Acta Mater.* **2008**, 56, 5737-5750.

[75] R. J. Varley, S. van der Zwaag, *Polym. Test.* **2008**, 27, 11-19.

[76] P. T. Mather, X. Luo, I. A. Rousseau, *Annu. Rev. Mater. Res.* **2009**, 39, 445-471.

[77] X. Lan, Y. Liu, H. Lv, X. Wang, J. Leng, S. Du, *Smart Mater. Struct.* **2009**, 18, 024002.

[78] K. Wei, G. Zhu, Y. Tang, X. Li, T. Liu, L. Niu, *Composites B* **2013**, 51, 169-174.

[79] S. Chen, J. Hu, H. Zhuo, Y. Zhu, *Mater. Lett.* **2008**, 62, 4088-4090.

[80] X. Xiao, T. Xie, Y. T. Cheng, *J. Mater. Chem.* **2010**, 20, 3508-3514.

[81] G. Li, N. Uppu, *Compos. Sci. Technol.* **2010**, 70, 1419-1427.

[82] J. Nji, G. Li, *Smart Mater. Struct.* **2012**, 21, 025011.

[83] J. Nji, G. Li, *Polymer* **2010**, 51, 6021-6029.

[84] E. D. Rodriguez, X. Luo, P. T. Mather, *ACS Appl. Mater Interfaces* **2011**, 3, 152-161.

[85] X. Luo, P. T. Mather, *ACS Macro Lett.* **2013**, 2, 152-156.

[86] T. C. Bor, L. Warnet, R. Akkerman, A. de Boer, *J. of Comp. Mat.* **2010**, 44, 2547-2572.

[87] S. Neuser, V. Michaud, S. R. White, *Polymer* **2012**, 53, 370-378.

[88] M. Zako, N. Takano, *J. Intell. Mater. Syst. Struct* **2000**, 10, 836-841.

[89] S. A. Hayes, F. R. Jones, K. Marshiya, W. Zhang, *Composites A* **2007**, 38, 1116-1120.

[90] S. A. Hayes, W. Zhang, M. Branthwaite, F. R. Jones, *J. R. Soc. Interface* **2007**, 4, 381-387.

[91] T. J. Swait, F. R. Jones, S. A. Hayes, *Compos. Sci. Technol.* **2012**, 72, 1515-1523.

[92] M. A. M. Rahmathullah, G. R. Palmese, *J. Appl. Polym. Sci.* **2009**, 113, 2191-2201.

[93] A. M. Peterson, H. Kotthapalli, M. A. M. Rahmathullah, G. R. Palmese, *Compos. Sci. Technol.* **2012**, 72, 330-336.

[94] S. Meure, S. Furman, S. Khor, *Macromol. Mater. Eng.* **2010**, 295, 420-424.

[95] S. Meure, D. Y. Wu, S. Furman, *Acta Mater.* **2009**, 57, 4312-4320.

[96] S. Meure, R. J. Varley, D. Y. Wu, S. Mayo, K. Nairn, S. Furman, *Eur. Polym. J.* **2012**, 48, 524-531.

[97] S. Meure, D. Y. Wu, S. A. Furman, *Vib. Spectrosc.* **2010**, 52, 10-15.

[98] R. J. Varley, G. P. Parn, *Compos. Sci. Technol.* **2012**, 72, 453-460.

[99] K. Hargou, K. Pingkarawat, A. P. Mouritz, C. H. Wang, *Composites B* **2013**, 45, 1031-1039.

[100] X. Luo, R. Ou, D. E. Eberly, A. Singhal, W. Viratyaporn, P. T. Mather, *ACS Appl. Mater. Interfaces* **2009**, 1, 612-620.

[101] J. Zhang, T. Lin, S. C. P. Cheung, C. H. Wang, *Compos. Sci. Technol.* **2012**, 72, 1952-1959.

[102] Y. Chen, A. M. Kushner, G. A. Williams, Z. Guan, *Nature Chemistry* **2012**, 4, 467-472.

[103] K. B. Amer, *Journal of the American Helicopter Society*, **1989**, *34*, 3-13.

[104] P. M. Toor, *Eng. Fract. Mech.* **1973**, *5*, 837-880.

[105] M. C. Y. Niu, *Airframe structural design: Practical design information and data on aircraft structures*, ConMilit Press Ltd, 1988.

[106] J. Siegl, I. Nedbal, J. Kunz, *Int. J. Fatigue* **2009**, *31*, 1062-1067.

[107] A. Corigliano, *Int. J. Solids Struct.* **1993**, *30*, 2779-2811.

[108] Y. Mi , M. A. Criesfield, G. A. O. Davies, H. B. Hellweg, *J. Compos. Mater.* **1998**, *32*, 1246-1272.

[109] P. P. Camanho, C. G. Davila, M.F. de Moura, *J. Compos. Mater.* **2003**, *37*, 1415-1438.

[110] A. Airoldi, G. Sala, P. Bettini, A. Baldi, *J. Reinf. Plast. Comp.* **2013**, *32*, 1075-1091.

[111] W. H. Binder, *Self-healing Polymers: from principles to applications*, Wiley, 2013.

[112] S. J. Garcia, H. R. Fischer in: M. R. Aguilar de Armas, J. San Roman, *Smart polymers and their applications*, Woodhead, 2013.

[113] M. R. Kessler, S.R White, *Composites A* **2001**, 32, 683-699.

[114] M. R. Kessler, N. R. Sottos, S. R. White, *Composites A* **2003**, 34, 743-753.

[115] T. Yin, L. Zhou, M. Z. Rong, M. Q. Zhang, *Smart Mater. Struct.* **2008**, 17, 015019.

[116] K. Pingkarawat, C. H. Wang, R. J. Varley, A. P. Mouritz, *J. Mater. Sci.* **2012**, 47, 4449-4456.

[117] E. N. Brown, S. R. White, N. R. Sottos, *Compos. Sci. Technol.* **2005**, 65, 2474-2480

[118] A. S. Jones, J. D. Rule, J. S. Moore, N. R. Sottos, S. R. White, *J. R. Soc. Interface* **2007**, 4, 395-403.

[119] Y. C. Yuan, M. Z. Rong, M. Q. Zhang, G. C. Yang, J. Q. Zhao, *Express Polym. Lett.* **2011**, 5, 47-59.

[120] T. Yin, M. Z. Rong, J. Wu, H. Chen, M. Q. Zhang, *Composites A* **2008**, 39, 1479-1487.

[121] A. J. Patel, N. R. Sottos, E. D. Wetzel, S. R. White, *Composites A* **2010**, 41, 360-368.

[122] G. J. Williams, I. P. Bond, R. S. Trask, *Composites A* **2009**, 40, 1399-1406.

[123] L. Holiday, *Ionic Polymer*, Applied Science Publisher, 1975.

[124] H. Akimoto, T. Kanazawa, M. Yamada, S. Matsuda, G. O. Shonaike, A. J. Murakami, *Appl. Polym. Sci.* **2001**, 81, 1712-1720.

[125] R. C. Scogna, R. A. Register, *J. Polym. Sci. Part B*. **2009,** 47, 1588-1598.

[126] R. C. Scogna, R. A. Register, *Polymer* **2009**, 50, 585-590.

[127] S. J. Kalista, J. R. Pflug, R. J. Varley, *Polym. Chem.* **2013**, *4*, 4910-4926.

[128] H. P. Kulkarni, G. Mogilevsky, W. M. Mullins, Y. J. Wu, *Mater. Res*. **2009**, 24, 1087-1092.

[129] Y. Loo, K. Wakabayashi, Y. E. Huang, R. A. Register, B. S. Hsiao, *Polymer* **2005**, 46, 5118-5124.

[130] F. Angrilli, D. Pavarin, M. De Cecco, A. Francesconi, *Acta Astronaut.* **2003**, 53, 185-189.

[131] A. Eisenberg, B. Hird, R. B. Moore, *Macromolecules* **1990**, *23*, 4098-4107.

[132] A. Eisenberg, M. Rinaudo, *Polymer Bulletin* **1990**, *24*, 671-671

[133] K. Tadano, E. Hirasawa, H. Yamamoto , S. Yano, *Macromolecules* **1989**, *22*, 226-233.

[134] K. Han, H. L. Williams, *J. Appl. Polym. Sci.* **1991**, *42*, 1845-1859.

[135] K. Wakabayashi, R. A. Register, *Macromolecules* **2006**, *39*, 1079-1086.

[136] Y. Tsujita, K. Shibayama, A. Takizawa, T. Kinoshita, I. Uematsu, *J. Appl. Polym. Sci.* **1987**, *33*, 1307–1314.

[137] M.W. Spencer, M.D. Wetzel, C. Troeltzsch, D.R. Paul, *Polymer* **2012**, *53*, 569-580.

[138] E. Hirasawa, Y. Yamamoto, K. Tadano, S. Yano, *J. Appl. Polym. Sci.* **1991**, *42*, 351–362.

[139] M. Kohzaki, Y. Tsujita, A. Takizawa, T. Kinoshita, *J. Appl. Polym. Sci.* **1987**, *33*, 2393-2402.

[140] R. J. Varlery and S .J. Kalista, “Synchrotron Ionomers Studies”, Unpublished results.

[141] P. C. Painter, M. Watzek, J. L. Koenig, *Polymer* **1977**, *18*, 1169-1172.

[142] P. C. Painter, B. A. Brozoski, M. M. Coleman, *J. Polym. Sci Part B* **1982**, *20*, 1069-1080

[143] M. M. Coleman, J. Y. Lee, P. C. Painter, *Macromolecules* **1990**, *23*, 2339-2345.

[144] D. A. Siuzdak, P. R. Start, K. A. Mauritz, *J. Appl. Polym. Sci.* **2000**, *77*, 2832-2844.

[145] R. A. Register, S. L. Copper, *Macromolecules* **1990**, *23*, 318-323.

[146] D. J. Quiram, R. A. Register, *Macromolecules* **1998**, *31*, 1432-1435.

[147] J. D. Ferry, *Viscoelastic properties of polymers*, Wiley 1980.

[148] T. T. Hsieh, C. Tiu, G. P. Simon, *Polymer* **2001**, *42*, 1931-1939.

[149] T. Kurian, M. Nishio, A. Nishioka, T. Takahashi, K. Koyama, *Int. J. Polym. Mater.* **2007**, *56*, 135-145.

[150] W.P. Cox and E.H. Merz, *J. Polym. Sci.* **1958**, *28*, 619-622.

[151] P. D. Gujrati, A. I. Leonov, *Modeling and Simulation in Polymers*, Wiley, 2010.

[152] M.M. Cross, *J. Colloid Sci.* **1965**, *20*, 417-437.

[153] K. Wakabayashi, R. A. Register, *Polymer* **2005**, *46*, 8838-8845.

[154] R. C. Scogna, R. A. Register, *Polymer* **2008**, *49*, 992-998.

[155] B. J. Briscoe, F. Motamedi, *Wear* **1992**, *158*, 229-247.

[156] B. L. Lee, T. F. Walsh, S. T. Won, H. M. Patts, J. W. Song, A. H. Mayer, *J. Compos. Mater.* **2001**, *35*, 1605-1633.

[157] M. Karahan, A. Kus, R. Eren, *Int. J. Impact Eng.* **2008**, *35*, 499-510.

[158] J. R. Brown, P. J. C. Chappell, Z. Mathys, *J. Mater. Sci.* **1991**, *26*, 4172-4178.

[159] J.G. Carrillo, R.A. Gamboa, E.A. Flores-Johnson, P.I. Gonzalez- Chi, *Polym. Test.* **2012**, *31*, 512-519.

[160] Y. S. Lee, E. D. Wetzel, N. J. Wagner, *J. Mater. Sci.* **2003**, *38*, 2825-2833.

[161] S. Sihn, B. P. Rice, *J. Compos. Mater.* **2003**, *37*, 1319-1336.

[162] G. Janszen, P. G. Nettuno in: M. Guarascio, C. A. Brebbia , F. Garzia editors, *Safety and Security Engineering III*, WIT Press, 2009.

[163] G. Janszen, P. G. Nettuno, *Proc. 14th International Conference on Computational Methods and Experimental Measurements*, Algarve, Portugal, **2009**.

[164] G. Janszen, P. G. Nettuno, *Proc. 3rd International Conference on Safety and Security Engineering*, Rome, Italy, **2009**.

[165] C.-G. Kim, E.-J. Jun, *J. Compos. Mater.* **1992**, *26*, 2247-2261.

[166] K. F. Karlsson, B. T. Astrom, *Composites Part A* **1997**, *28*, 97-111.

[167] H. Zhao, G. Gary, *Int. J. Impact Eng.* **1998**, *21*, 827-836.

[168] J. M. Vega, unpublished results.

[169] J. H. Lee, D. Veysset, J. P. Singer, M. Retsch, G. Saini, T. Pezeril, K. A. Nelson, E. L. Thomas, *Nat. Commun.* **2012**, *3*, art. no. 1164.

[170] E. J. Brandon, M. Vozoff, E. A. Kolawa, G. F. Studor, F. Lyons, M. W. Keller, B. Beiermann, S. R. White, N. R. Sottos, M. A. Curry, D. L. Banks, R. Brocato, L. Zhou, S. Jung, T. N. Jackson, K. Champaigne, *Acta Astronaut.* **2011**, *68*, 883-903.

[171] C. Pardini, L. Anselmo, *Adv. Space Res.* **2011**, *48*, 557-569.

[172] M. Chipara, J. Zaleski, B. Dragnea, E. Shansky, T. Onuta, *Proc. of the 47th AIAA/ASME/ASCE/AHS/ASC Structures, Structural Dynamics and Materials Conference*, Newport, Rhode Island, USA, **2006**.

List of publications

Journal papers

1. S. van der Zwaag, A. M. Grande, W. Post, S. J. Garcia, T. C. Bor, "A review of current strategies to induce self-healing behaviour in fibre reinforced polymer based composites", *Materials Science and Technology* **2013**. Submitted.
2. M.A. Rahman, G. Spagnoli, A. M. Grande, L. Di Landro, "Role of phase morphology on the damage initiated self-healing behavior of ionomer blends", *Macromolecular Materials and Engineering* **2013**, *298*, 1350-1364.
3. A. M. Grande, L. Castelnovo, L. Di Landro, C. Giacomuzzo, A. Francesconi, M. A. Rahman, "Rate-dependent self-healing behavior of an ethylene-co-methacrylic acid ionomer under high-energy impact conditions", *Journal of Applied Polymer Science* **2013**, *130*, 1949-1958.
4. A. Francesconi, C. Giacomuzzo, A. M. Grande, T. Mudric, M. Zaccariotto, E. Etemadi, L. Di Landro, U. Galvanetto, "Comparison of self-healing ionomer to aluminium-alloy bumpers for protecting spacecraft equipment from space debris impacts", *Advances in Space Research*, **2013**, *51*, 930-940.
5. M. A. Rahman, M. Penco, I. Peroni, G. Ramorino, A. M. Grande, L. Di Landro, "Self-repairing systems based on ionomers and epoxidized natural rubber blends", *ACS Applied Materials and Interfaces* **2011**, *3*, 4865-4874.
6. M. A. Rahman, M. Penco, G. Spagnoli, A. M. Grande, L. Di Landro, "Self-healing behavior of blends based on ionomers with ethylene/vinyl alcohol copolymer or epoxidized natural rubber", *Macromolecular Materials and Engineering* **2011**, *296*, 1119-1127.

Conference proceedings

1. G. Janszen, A.M. Grande, P. Bettini, L. Di Landro, "Improved solutions for dangerous liquid containment", *Proc. 5th International Conference on Safety and Security Engineering, SAFE,* Rome, Italy, **2013**.
2. A. M. Grande, S. Coppi, L. Di Landro, G.Sala, C. Giacomuzzo, A. Francesconi, M. A. Rahman, "An experimental study of the self-healing behavior of ionomeric systems under ballistic impact tests", *Proc. SPIE 'Behavior and Mechanics of Multifunctional Materials and Composites'*, San Diego, USA, **2012**, paper 83420U. *Oral presentation*

3. A. M. Grande, L. Di Landro, P. Bettini, A. Baldi, G. Sala, "RTM process monitoring and strain acquisition by fibre optics", Proc. 11th International Conference on the Mechanical Behavior of Materials, ICM11, Como, Italy, **2011**. *Poster*

Conference presentations

1. AIDAA XXII - Italian Association of Aeronautics and Astronautics Conference (Napoli, September 2013). "Evaluation tests on Self-Healing ionomers for space applications", L. Castelnovo, A. M. Grande, P. Bettini, G. Sala, C. Giacomuzzo, A. Francesconi, L. Di Landro.
2. ICCM19 - 19th International Conference on Composite Materials (Montreal, July 2013). "Multilayer composites with self-healing capability based on an EMAA ionomer", A. M. Grande, L. Castelnovo, L. Di Landro, G. Sala, C. Giacomuzzo, A. Francesconi. *Oral presentation*
3. ICCM19 - 19th International Conference on Composite Materials (Montreal, July 2013). "Impact behavior of a simple multifunctional plate structure", T. Mudric, U. Galvanetto, A. Francesconi, C. Giacomuzzo, M. Zaccariotto, A. M. Grande, L. Di Landro.
4. 4ICSHM - 4th International Conference on Self-Healing Materials (Ghent, June 2013). "Effects of Na neutralization level on the SH behaviour after ballistic tests of EMAA based ionomers", A. M. Grande, L. Castelnovo, I. Quadrio, S. Zaffaroni, L. Di Landro. *Oral presentation*
5. 4ICSHM - 4th International Conference on Self-Healing Materials (Ghent, June 2013). "A cohesive elements based model to describe fracture and cohesive healing in elastomers", A. Baldi, A. M. Grande, R. K. Bose, A. Airoldi, S. J. Garcia, L. Di Landro, S. van der Zwaag. *Oral presentation*
6. 4ICSHM - 4th International Conference on Self-Healing Materials (Ghent, June 2013). "Hypervelocity impact and outgassing tests on ethylene-co-methacrylic acid ionomers for space applications", L. Castelnovo, A. M. Grande, L. Di Landro, G. Sala, C. Giacomuzzo, A. Francesconi.
7. ECCM15 - 15th European Conference on Composite Materials (Venezia, June 2012). "Self-Healing behaviour of ionomers and ionomer composites under ballistic impact tests at different speeds", A. M. Grande, L. Di Landro, G. Janszen, C. Giacomuzzo, A. Francesconi. *Oral presentation*

8. ECCM15 - 15th European Conference on Composite Materials (Venezia, June 2012). “Impact tests and simulations for multifunctional materials”, T. Mudric, C. Giacomuzzo, U. Galvanetto, A. Francesconi, M. Zaccariotto, A.M. Grande, L. Di Landro.
9. BiPoCo 2012 - International Conference on Biobased Polymers and Composites (Balaton, Hungary 2012). “PLA/PEG Matrix Composites with Microfibrillated Cellulose”, L. Di Landro, A. Rahman, M. Penco, A.M. Grande.
10. EUCASS 2011 - European Conference for Aerospace Sciences (St. Petersburg, July 2011). “Self-healing response in different ionomer binary blends during projectile puncture tests”, A. M. Grande, M. A. Rahman, L. Di Landro, M. Penco, I. Peroni. *Oral presentation*
11. 3ICSHM - 3rd International Conference on Self-Healing Materials (Bath, June 2011). “Self healing of blends based on Sodium Salt of Poly(Ethylene-co-Methacrylic Acid)/ poly(ethylene-co-vinyl alcohol) and epoxidized natural rubber following high energy impact”, A. M. Grande, M. A. Rahman, L. Di Landro, M. Penco, G. Spagnoli. *Oral presentation*